

# Measurement of the CKM angle $\gamma$ using $B_s^0 \rightarrow D_s K \pi\pi$ decays

P. d'Argent<sup>1</sup>, E. Gersabeck<sup>2</sup>, M. Kecke<sup>1</sup>, M. Schiller<sup>3</sup>

<sup>1</sup>*Physikalisches Institut, Ruprecht-Karls-Universität Heidelberg, Heidelberg, Germany*

<sup>2</sup>*School of Physics and Astronomy, University of Manchester, Manchester, United Kingdom*

<sup>3</sup>*School of Physics and Astronomy, University of Glasgow, Glasgow, United Kingdom*

## Abstract

We present the first measurement of the weak phase  $2\beta + \gamma$  obtained from a time-dependent (amplitude) analysis of  $B_s^0 \rightarrow D_s K \pi\pi$  decays using proton-proton collision data corresponding to an integrated luminosity of  $7 \text{ fb}^{-1}$  recorded by the LHCb detector.



# Contents

<b>1</b>	<b>Introduction</b>	<b>1</b>
<b>2</b>	<b>Formalism</b>	<b>2</b>
2.1	Decay rates and $CP$ -observables . . . . .	2
2.2	Amplitude model . . . . .	4
2.2.1	Form Factors and Resonance Lineshapes . . . . .	4
2.2.2	Spin Densities . . . . .	6
2.3	Fit implementation . . . . .	8
2.4	Validation . . . . .	9
<b>3</b>	<b>Data samples and event selection</b>	<b>12</b>
3.1	Stripping and Trigger selection . . . . .	12
3.2	Offline selection . . . . .	12
3.2.1	Phase space region . . . . .	13
3.2.2	Physics background vetoes . . . . .	14
3.2.3	Training of multivariate classifier . . . . .	17
3.2.4	Final selection . . . . .	19
<b>4</b>	<b>Yields determination</b>	<b>22</b>
4.1	Signal model . . . . .	22
4.2	Background models . . . . .	23
4.3	Results . . . . .	24
<b>5</b>	<b>Decay-time Resolution</b>	<b>26</b>
5.1	Calibration for Run-I data . . . . .	27
5.2	Calibration for Run-II data . . . . .	28
<b>6</b>	<b>Acceptance</b>	<b>31</b>
6.1	MC corrections . . . . .	31
6.1.1	Truth matching of simulated candidates . . . . .	31
6.1.2	Correction of data-simulation differences . . . . .	31
6.2	Decay-time acceptance . . . . .	32
6.3	Phase space acceptance . . . . .	37
<b>7</b>	<b>Flavour Tagging</b>	<b>40</b>
7.1	OS tagger combination . . . . .	40
7.2	Tagging performance . . . . .	42
<b>8</b>	<b>Production and Detection Asymmetries</b>	<b>44</b>
8.1	$B_s$ Production Asymmetry . . . . .	44
8.2	$K^-\pi^+$ Detection Asymmetry . . . . .	45
<b>9</b>	<b>Decay-time fit</b>	<b>48</b>
9.1	Fit to $B_s^0 \rightarrow D_s\pi\pi\pi$ data . . . . .	48
9.2	Fit to $B_s^0 \rightarrow D_sK\pi\pi$ data . . . . .	49

<b>10 Time-dependent amplitude fit</b>	<b>51</b>
10.1 Signal Model Construction . . . . .	51
10.2 Results . . . . .	54
<b>11 Systematic uncertainties</b>	<b>57</b>
11.1 Fit bias . . . . .	57
11.2 Background subtraction . . . . .	57
11.3 Decay-time acceptance . . . . .	58
11.4 Decay-time resolution and tagging . . . . .	58
11.5 Production, detection asymmetries and mixing frequency . . . . .	59
11.6 Multiple candidates . . . . .	59
11.7 Length and momentum scales . . . . .	59
11.8 Phase space acceptance . . . . .	60
11.9 Resonance description . . . . .	60
11.10 Alternative amplitude models . . . . .	61
<b>A Stripping and Trigger cuts</b>	<b>65</b>
<b>B Details of multivariate classifier</b>	<b>67</b>
<b>C Detailed mass fits</b>	<b>71</b>
<b>D Decay-time Resolution fits</b>	<b>75</b>
<b>E Comparison of time-acceptance in subsamples</b>	<b>78</b>
<b>F Spin Amplitudes</b>	<b>79</b>
<b>G Considered Decay Chains</b>	<b>80</b>
<b>H Data-simulation comparisson</b>	<b>81</b>
<b>I Data distributions</b>	<b>82</b>
I.1 Comparison of signal and calibration channels . . . . .	82
I.2 Comparison of Run-I and Run-II data . . . . .	83
I.3 Comparison of $D_s$ final states . . . . .	83
I.4 Comparison of trigger categories . . . . .	84
<b>References</b>	<b>85</b>

# 1 Introduction

The weak phase  $\gamma$  is the least well known angle of the CKM unitary triangle. A key channel to measure  $\gamma$  is the time-dependent analysis of  $B_s^0 \rightarrow D_s K$  decays [1, 2].

To measure the weak CKM phase  $\gamma \equiv \arg[-(V_{ud}V_{ub}^*)/(V_{cd}V_{cb}^*)]$ , a decay with interference between  $b \rightarrow c$  and  $b \rightarrow u$  transitions is needed [1]. This note present the first measurement of  $\gamma$  using  $B_s^0 \rightarrow D_s K\pi\pi$  decays, where the  $K\pi\pi$  subsystem is dominated by excited kaon states such as the  $K_1(1270)$  and  $K_1(1400)$  resonances. To account for the non-constant strong phase across the phasespace, one can either perform a time-dependent amplitude fit or select a suitable phase-space region and introduce a coherence factor as additional hadronic parameter to the fit. This analysis is based on the first observation of the  $B_s^0 \rightarrow D_s K\pi\pi$  decay by LHCb [3, 4], where the branching ratio is measured relative to  $B_s^0 \rightarrow D_s \pi\pi\pi$ .

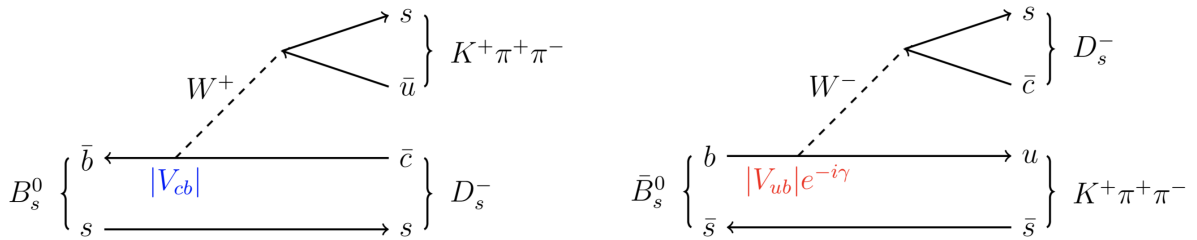


**Figure 1.1:** Feynman diagram for  $B_s^0/\bar{B}_s^0 \rightarrow D_s^- K^+ \pi^+ \pi^-$  decays.

## 13 2 Formalism

### 14 2.1 Decay rates and *CP*-observables

15 The differential decay rate of  $B_s^0$  or  $\bar{B}_s^0$  decays to the final state  $D_s^- K^+ \pi\pi$  or  $D_s^+ K^- \pi\pi$  is  
 16 given by:

$$\begin{aligned} \frac{d\Gamma(\mathbf{x}, t, q, f)}{e^{-\Gamma_s t} dt d\Phi_4} &\propto (|\mathcal{A}_f^c(\mathbf{x})|^2 + |\mathcal{A}_f^u(\mathbf{x})|^2) \cosh\left(\frac{\Delta\Gamma_s t}{2}\right) \\ &\quad + q f (|\mathcal{A}_f^c(\mathbf{x})|^2 - |\mathcal{A}_f^u(\mathbf{x})|^2) \cos(\Delta m_s t) \\ &\quad - 2\text{Re}(\mathcal{A}_f^c(\mathbf{x})^* \mathcal{A}_f^u(\mathbf{x}) e^{-if(\gamma-2\beta_s)}) \sinh\left(\frac{\Delta\Gamma_s t}{2}\right) \\ &\quad - 2q f \text{Im}(\mathcal{A}_f^c(\mathbf{x})^* \mathcal{A}_f^u(\mathbf{x}) e^{-if(\gamma-2\beta_s)}) \sin(\Delta m_s t) \end{aligned} \quad (2.1)$$

17 where  $q = +1$  (-1) refers to an initially produced  $B_s^0$  ( $\bar{B}_s^0$ ) flavour eigenstate,  $q = 0$  to an  
 18 undetermined initial flavour,  $f = +1$  or -1 denotes  $D_s^- K^+ \pi\pi$  or  $D_s^+ K^- \pi\pi$  final states and  
 19  $\Gamma_s$ ,  $\Delta\Gamma_s$  and  $\Delta m_s$  are the width average, the width difference and the mass difference of  
 20 the two  $B_s$  mass eigenstates. We choose a convention in which  $\Delta\Gamma_s < 0$  and  $\Delta m_s > 0$ .  
 21 We further assume  $|q/p| = 1$  for the complex coefficients  $p$  and  $q$  which relate the  $B_s$   
 22 meson mass eigenstates to the flavour eigenstates (no *CP* violation in the mixing). The  
 23 CKM angle  $\gamma$  can be extracted from the *CP* violating phase associated to the interference  
 24 between mixing and decay,  $\gamma - 2\beta_s$ , since the  $B_s^0 - \bar{B}_s^0$  mixing phase,  $\beta_s$ , is well constrained  
 25 from  $B_s \rightarrow J/\psi \phi$  and related modes.

26 The static total decay amplitudes  $\mathcal{A}_f^c(\mathbf{x})$  and  $\mathcal{A}_f^u(\mathbf{x})$  are given by the coherent sum  
 27 over all intermediate state amplitudes  $A_i(\mathbf{x})$ , each weighted by a complex coefficient to be  
 28 determined from data,

$$\mathcal{A}(B_s^0 \rightarrow D_s^- K^+ \pi\pi) \equiv \mathcal{A}_f^c(\mathbf{x}) = \sum_i a_i^c A_i(\mathbf{x}) \quad (2.2)$$

$$\mathcal{A}(\bar{B}_s^0 \rightarrow D_s^- K^+ \pi\pi) \equiv \mathcal{A}_f^u(\mathbf{x}) = \sum_i a_i^u A_i(\mathbf{x}) \quad (2.3)$$

29 where the superscript  $c$  ( $u$ ) indicates a  $b \rightarrow c$  ( $b \rightarrow u$ ) quark-level transition and  $\mathbf{x}$   
 30 represents a unique set of kinematic conditions within the five-dimensional phase space of  
 31 the decay. Convenient choices for the kinematic observables include the invariant mass  
 32 combinations of the final state particles or acoplanarity and helicity angles. In practice,  
 33 we do not need to choose a particular five-dimensional basis, but use the full four-vectors  
 34 of the decay in our analysis. The dimensionality is handled by the phase space element  
 35 which can be written in terms of any set of five independent kinematic observables,  
 36  $\mathbf{x} = (x_1, \dots, x_5)$ , as

$$d\Phi_4 = \phi_4(\mathbf{x}) d^5 x, \quad (2.4)$$

37 where  $\phi_4(\mathbf{x}) = \left| \frac{\partial \Phi_4}{\partial(x_1, \dots, x_5)} \right|$  is the phase space density. In contrast to three-body decays,  
 38 the four-body phase space density function is not flat in the usual kinematic variables.  
 39 Therefore, an analytic expression for  $\phi_4$  is taken from Ref. [5].

<sup>40</sup> Assuming there is no direct  $CP$  violation in the  $B_s$  decay implies for the  $CP$  conjugate  
<sup>41</sup> transition amplitudes:

$$\mathcal{A}(\bar{B}_s^0 \rightarrow \bar{f}) = \mathcal{A}_f^c(\mathbf{x}) = \mathcal{A}_f^c(\bar{\mathbf{x}}) \quad (2.5)$$

$$\mathcal{A}(B_s^0 \rightarrow \bar{f}) = \mathcal{A}_f^u(\mathbf{x}) = \mathcal{A}_f^u(\bar{\mathbf{x}}) \quad (2.6)$$

<sup>42</sup> where the  $CP$ -conjugate phase space point  $\bar{\mathbf{x}}$  is defined such that it is mapped onto  $\mathbf{x}$  by  
<sup>43</sup> the interchange of final state charges, and the reversal of three-momenta.

<sup>44</sup> The phenomenological description of the intermediate state amplitudes is discussed  
<sup>45</sup> in Sec. 2.2. For a model-independent measurement, the differential decay rate can be  
<sup>46</sup> integrated over the phase space:

$$\begin{aligned} \int \frac{d\Gamma(x, t, q, f)}{e^{-\Gamma_s t} dt d\Phi_4} d\Phi_4 &\propto \cosh\left(\frac{\Delta\Gamma_s t}{2}\right) + q f C \cos(\Delta m_s t) \\ &+ D_f \sinh\left(\frac{\Delta\Gamma_s t}{2}\right) - q S_f \sin(\Delta m_s t) \end{aligned} \quad (2.7)$$

<sup>47</sup> where the same convention for the  $CP$  coefficients as for the  $B_s \rightarrow D_s K$  analysis is used:

$$C = \frac{1 - r^2}{1 + r^2} \quad (2.8)$$

$$D_f = -\frac{2 r \kappa \cos(\delta - q_f (\gamma - 2\beta_s))}{1 + r^2} \quad (2.9)$$

$$S_f = f \frac{2 r \kappa \sin(\delta - q_f (\gamma - 2\beta_s))}{1 + r^2} \quad (2.10)$$

<sup>48</sup> The coherence factor  $\kappa$ , the strong phase difference  $\delta$  and the ratio of the suppressed  
<sup>49</sup> ( $b \rightarrow u$ ) over favored ( $b \rightarrow c$ ) decay mode, averaged over the phase space, are defined as:

$$\kappa e^{i\delta} \equiv \frac{\int \mathcal{A}_f^c(x)^* \mathcal{A}_f^u(x) d\Phi_4}{\sqrt{\int |\mathcal{A}_f^c(x)|^2 d\Phi_4} \sqrt{\int |\mathcal{A}_f^u(x)|^2 d\Phi_4}} \quad (2.11)$$

$$r \equiv \frac{\sqrt{\int |\mathcal{A}_f^u(x)|^2 d\Phi_4}}{\sqrt{\int |\mathcal{A}_f^c(x)|^2 d\Phi_4}}. \quad (2.12)$$

<sup>50</sup> The coherence factor dilutes the sensitivity to the weak phase  $\gamma$  due to the integration  
<sup>51</sup> over the interfering amplitudes across the phase space. The value of  $\kappa$  is bounded between  
<sup>52</sup> zero and unity. The latter corresponds to the limit of only one contributing intermediate  
<sup>53</sup> state in which case the same sensitivity as in  $B_s \rightarrow D_s K$  decays is reached, while  $\kappa = 0$   
<sup>54</sup> would result in no sensitivity to  $\gamma$  at all.

## 55 2.2 Amplitude model

56 To construct the intermediate state amplitudes  $A_i(\mathbf{x})$ , the isobar approach is used, which  
 57 assumes that the decay process can be factorized into subsequent two-body decay am-  
 58 plitudes [6–8]. This gives rise to two different decay topologies; quasi two-body decays  
 59  $B_s \rightarrow (R_1 \rightarrow h_1 h_2) (R_2 \rightarrow h_3 h_4)$  or cascade decays  $B_s \rightarrow h_1 [R_1 \rightarrow h_2 (R_2 \rightarrow h_3 h_4)]$ . In  
 60 either case, the intermediate state amplitude is parameterized as a product of orbital  
 61 angular momentum,  $L$ , dependent form factors  $B_L$ , included for each vertex of the decay  
 62 tree, Breit-Wigner propagators  $T_R$ , included for each resonance  $R$ , and an overall angular  
 63 distribution represented by a spin factor  $S$ ,

$$A_i(\mathbf{x}) = B_{L_{B_s}}(\mathbf{x}) [B_{L_{R_1}}(\mathbf{x}) T_{R_1}(\mathbf{x})] [B_{L_{R_2}}(\mathbf{x}) T_{R_2}(\mathbf{x})] S_i(\mathbf{x}). \quad (2.13)$$

64 The following description of the individual components is adapted from Ref. [9] and  
 65 only included for completeness.

### 66 2.2.1 Form Factors and Resonance Lineshapes

67 To account for the finite size of the decaying resonances, the Blatt-Weisskopf penetration  
 68 factors, derived in Ref. [10] by assuming a square well interaction potential with radius  
 69  $r_{\text{BW}}$ , are used as form factors,  $B_L$ . They depend on the breakup momentum  $q$ , and the  
 70 orbital angular momentum  $L$ , between the resonance daughters. Their explicit expressions  
 71 are

$$\begin{aligned} B_0(q) &= 1, \\ B_1(q) &= 1/\sqrt{1 + (q r_{\text{BW}})^2}, \\ B_2(q) &= 1/\sqrt{9 + 3 (q r_{\text{BW}})^2 + (q r_{\text{BW}})^4}. \end{aligned} \quad (2.14)$$

72 Resonance lineshapes are described as function of the energy-squared,  $s$ , by Breit-Wigner  
 73 propagators

$$T(s) = \frac{1}{m_0^2 - s - i m_0 \Gamma(s)}, \quad (2.15)$$

74 where the total width,  $\Gamma(s)$ , is normalized to give the nominal width,  $\Gamma_0$ , when evaluated  
 75 at the nominal mass  $m_0$ .

76 For a decay into two stable particles  $R \rightarrow AB$ , the energy dependence of the decay  
 77 width can be described by

$$\Gamma_{R \rightarrow AB}^{(2)}(s) = \Gamma_0 \frac{m_0}{\sqrt{s}} \left( \frac{q}{q_0} \right)^{2L+1} \frac{B_L(q)^2}{B_L(q_0)^2}, \quad (2.16)$$

78 where  $q_0$  is the value of the breakup momentum at the resonance pole [11].

79 The energy-dependent width for a three-body decay  $R \rightarrow ABC$ , on the other hand, is  
 80 considerably more complicated and has no analytic expression in general. However, it can  
 81 be obtained numerically by integrating the transition amplitude-squared over the phase  
 82 space,

$$\Gamma_{R \rightarrow ABC}^{(3)}(s) = \frac{1}{2\sqrt{s}} \int |A_{R \rightarrow ABC}|^2 d\Phi_3, \quad (2.17)$$

and therefore requires knowledge of the resonant substructure. The three-body amplitude  $A_{R \rightarrow ABC}$  can be parameterized similarly to the four-body amplitude in Eq. (2.13). In particular, it includes form factors and propagators of intermediate two-body resonances.

Both Eq. (2.16) and Eq. (2.17) give only the partial width for the decay into a specific channel. To obtain the total width, a sum over all possible decay channels has to be performed,

$$\Gamma(s) = \sum_i g_i \Gamma_i(s), \quad (2.18)$$

where the coupling strength to channel  $i$ , is given by  $g_i$ .

The treatment of the lineshape for various resonances considered in this analysis is described in what follows. The nominal masses and widths of the resonances are taken from the PDG [12] with the exceptions described below.

For the broad scalar resonance  $\sigma$ , the model from Bugg is used [13]. We use the Gounaris-Sakurai parametrization for the  $\rho(770)^0 \rightarrow \pi\pi$  propagator [14]. For the decay chain  $K_1(1270) \rightarrow \rho(770)K$ , we include  $\rho - \omega$  mixing with the relative magnitude and phase between  $\rho$  and  $\omega$  fixed to the values determined in Ref. [15]. The energy-dependent width of the  $f_0(980)$  resonance is given by the sum of the partial widths into the  $\pi\pi$  and  $KK$  channels [16], where the coupling constants as well as the mass and width are taken from a measurement performed by the BES Collaboration [17]. For the  $f_2(1270)$  and the  $f_0(1370)$  mesons we use the total decay widths calculated in Ref. [9] which take the channels  $\pi\pi$ ,  $KK$ ,  $\eta\eta$  and  $\pi\pi\pi\pi$  into account. The Lass parameterization is used to model the  $K\pi$   $S$ -wave contribution. It consists of the  $K_0^*(1430)$  resonance together with an effective range non-resonant component [18–20]:

$$T_{Lass}(s) = \frac{\sqrt{s}}{q \cot \delta_L - iq} + e^{2i\delta_L} \frac{m_0 \Gamma_0 \frac{m_0}{q_0}}{m_0^2 - s - i m_0 \Gamma_0 \frac{m_0}{\sqrt{s}} \frac{q}{q_0}} \quad (2.19)$$

with  $\cot \delta_L = \frac{1}{aq} + \frac{1}{2}rq$ . We use the values for the scattering length  $a$  and effective range parameter  $r$  from Ref. [18, 19]. Equation (2.16) is used for all other resonances decaying into a two-body final state.

For the resonances  $K_1(1270)$  and  $K(1460)$ , the energy-dependent widths as well as the nominal mass and width are taken from Ref. [21]. We further use the energy-dependent widths for the  $K_1(1400)$ ,  $K^*(1410)$  and  $K^*(1680)$  mesons from Ref. [9]. For all other resonances decaying into a three-body final state, an energy-dependent width distribution is derived from Equation 2.17 assuming an uniform phase space population.

Some particles may not originate from a resonance but are in a state of relative orbital angular momentum. We denote such non-resonant states by surrounding the particle system with brackets and indicate the partial wave state with an subscript; for example  $(\pi\pi)_S$  refers to a non-resonant di-pion  $S$ -wave. The lineshape for non-resonant states is set to unity.

<sup>118</sup> **2.2.2 Spin Densities**

<sup>119</sup> The spin amplitudes are phenomenological descriptions of decay processes that are required  
<sup>120</sup> to be Lorentz invariant, compatible with angular momentum conservation and, where  
<sup>121</sup> appropriate, parity conservation. They are constructed in the covariant Zemach (Rarita-  
<sup>122</sup> Schwinger) tensor formalism [22–24]. At this point, we briefly introduce the fundamental  
<sup>123</sup> objects of the covariant tensor formalism which connect the particle’s four-momenta to  
<sup>124</sup> the spin dynamics of the reaction and give a general recipe to calculate the spin factors  
<sup>125</sup> for arbitrary decay trees. Further details can be found in Refs. [25, 26].

<sup>126</sup> A spin- $S$  particle with four-momentum  $p$ , and spin projection  $\lambda$ , is represented by the  
<sup>127</sup> polarization tensor  $\epsilon_{(S)}(p, \lambda)$ , which is symmetric, traceless and orthogonal to  $p$ . These  
<sup>128</sup> so-called Rarita-Schwinger conditions reduce the a priori  $4^S$  elements of the rank- $S$  tensor  
<sup>129</sup> to  $2S + 1$  independent elements in accordance with the number of degrees of freedom of a  
<sup>130</sup> spin- $S$  state [23, 27].

<sup>131</sup> The spin projection operator  $P_{(S)}^{\mu_1 \dots \mu_S \nu_1 \dots \nu_S}(p_R)$ , for a resonance  $R$ , with spin  $S =$   
<sup>132</sup>  $\{0, 1, 2\}$ , and four-momentum  $p_R$ , is given by [26]:

$$\begin{aligned} P_{(0)}^{\mu\nu}(p_R) &= 1 \\ P_{(1)}^{\mu\nu}(p_R) &= -g^{\mu\nu} + \frac{p_R^\mu p_R^\nu}{p_R^2} \\ P_{(2)}^{\mu\nu\alpha\beta}(p_R) &= \frac{1}{2} \left[ P_{(1)}^{\mu\alpha}(p_R) P_{(1)}^{\nu\beta}(p_R) + P_{(1)}^{\mu\beta}(p_R) P_{(1)}^{\nu\alpha}(p_R) \right] - \frac{1}{3} P_{(1)}^{\mu\nu}(p_R) P_{(1)}^{\alpha\beta}(p_R), \end{aligned} \quad (2.20)$$

<sup>133</sup> where  $g^{\mu\nu}$  is the Minkowski metric. Contracted with an arbitrary tensor, the projection  
<sup>134</sup> operator selects the part of the tensor which satisfies the Rarita-Schwinger conditions.

<sup>135</sup> For a decay process  $R \rightarrow AB$ , with relative orbital angular momentum  $L$ , between  
<sup>136</sup> particle  $A$  and  $B$ , the angular momentum tensor is obtained by projecting the rank- $L$   
<sup>137</sup> tensor  $q_R^{\nu_1} q_R^{\nu_2} \dots q_R^{\nu_L}$ , constructed from the relative momenta  $q_R = p_A - p_B$ , onto the spin- $L$   
<sup>138</sup> subspace,

$$L_{(L)\mu_1 \dots \mu_L}(p_R, q_R) = (-1)^L P_{(L)\mu_1 \dots \mu_L \nu_1 \dots \nu_L}(p_R) q_R^{\nu_1} \dots q_R^{\nu_L}. \quad (2.21)$$

<sup>139</sup> Their  $|\vec{q}_R|^L$  dependence accounts for the influence of the centrifugal barrier on the transition  
<sup>140</sup> amplitudes. For the sake of brevity, the following notation is introduced,

$$\begin{aligned} \varepsilon_{(S)}(R) &\equiv \varepsilon_{(S)}(p_R, \lambda_R), \\ P_{(S)}(R) &\equiv P_{(S)}(p_R), \\ L_{(L)}(R) &\equiv L_{(L)}(p_R, q_R). \end{aligned} \quad (2.22)$$

<sup>141</sup> Following the isobar approach, a four-body decay amplitude is described as a product  
<sup>142</sup> of two-body decay amplitudes. Each sequential two-body decay  $R \rightarrow A B$ , with relative  
<sup>143</sup> orbital angular momentum  $L_{AB}$ , and total intrinsic spin  $S_{AB}$ , contributes a term to the  
<sup>144</sup> overall spin factor given by

$$\begin{aligned} S_{R \rightarrow AB}(\mathbf{x}|L_{AB}, S_{AB}; \lambda_R, \lambda_A, \lambda_B) &= \varepsilon_{(S_R)}(R) X(S_R, L_{AB}, S_{AB}) L_{(L_{AB})}(R) \\ &\times \Phi(\mathbf{x}|S_{AB}; \lambda_A, \lambda_B), \end{aligned} \quad (2.23)$$

<sup>145</sup> where

$$\Phi(\mathbf{x}|S_{AB}; \lambda_A, \lambda_B) = P_{(S_{AB})}(R) X(S_{AB}, S_A, S_B) \varepsilon_{(S_A)}^*(A) \varepsilon_{(S_B)}^*(B). \quad (2.24)$$

<sup>146</sup> Here, a polarization vector is assigned to the decaying particle and the complex conjugate  
<sup>147</sup> vectors for each decay product. The spin and orbital angular momentum couplings are  
<sup>148</sup> described by the tensors  $P_{(S_{AB})}(R)$  and  $L_{(L_{AB})}(R)$ , respectively. Firstly, the two spins  $S_A$   
<sup>149</sup> and  $S_B$ , are coupled to a total spin- $S_{AB}$  state,  $\Phi(\mathbf{x}|S_{AB})$ , by projecting the corresponding  
<sup>150</sup> polarization vectors onto the spin- $S_{AB}$  subspace transverse to the momentum of the  
<sup>151</sup> decaying particle. Afterwards, the spin and orbital angular momentum tensors are  
<sup>152</sup> properly contracted with the polarization vector of the decaying particle to give a Lorentz  
<sup>153</sup> scalar. This requires in some cases to include the tensor  $\varepsilon_{\alpha\beta\gamma\delta} p_R^\delta$  via

$$X(j_a, j_b, j_c) = \begin{cases} 1 & \text{if } j_a + j_b + j_c \text{ even} \\ \varepsilon_{\alpha\beta\gamma\delta} p_R^\delta & \text{if } j_a + j_b + j_c \text{ odd} \end{cases}, \quad (2.25)$$

<sup>154</sup> where  $\varepsilon_{\alpha\beta\gamma\delta}$  is the Levi-Civita symbol and  $j$  refers to the arguments of  $X$  defined in  
<sup>155</sup> Eqs. 2.23 and 2.24. Its antisymmetric nature ensures the correct parity transformation  
<sup>156</sup> behavior of the amplitude. The spin factor for a whole decay chain, for example  $R \rightarrow$   
<sup>157</sup>  $(R_1 \rightarrow AB)(R_2 \rightarrow CD)$ , is obtained by combining the two-body terms and performing a  
<sup>158</sup> sum over all unobservable, intermediary spin projections

$$\sum_{\lambda_{R_1}, \lambda_{R_2}} S_{R \rightarrow R_1 R_2}(\mathbf{x}|L_{R_1 R_2}; \lambda_{R_1}, \lambda_{R_2}) S_{R_1 \rightarrow AB}(\mathbf{x}|L_{AB}; \lambda_{R_1}) S_{R_2 \rightarrow CD}(\mathbf{x}|L_{CD}; \lambda_{R_2}), \quad (2.26)$$

<sup>159</sup> where  $\lambda_R = \lambda_A = \lambda_B = \lambda_C = \lambda_D = 0$ ,  $S_{AB} = S_{CD} = 0$  and  $S_{R_1 R_2} = L_{R_1 R_2}$ , as only  
<sup>160</sup> pseudoscalar initial/final states are involved.

<sup>161</sup> The spin factors for all decay topologies considered in this analysis are explicitly given  
<sup>162</sup> in Appendix F.

### 163 2.3 Fit implementation

164 The hadronic amplitudes are renormalized prior to the amplitude fit such that

$$\int |A_i(\mathbf{x})|^2 d\Phi_4 = 1. \quad (2.27)$$

165 This allows us to set more intuitive starting values as the amplitude coefficients are all on  
166 a comparable scale. Moreover, the total amplitudes  $\mathcal{A}_f^{c(u)}(\mathbf{x})$  are renormalized on-the-fly  
167 such that

$$\begin{aligned} & \int \left| \mathcal{A}_f^{c(u)}(\mathbf{x}) \right|^2 d\Phi_4 = 1 \\ & \arg \left( \int \mathcal{A}_f^c(\mathbf{x})^* \mathcal{A}_f^u(\mathbf{x}) d\Phi_4 \right) = 0. \end{aligned} \quad (2.28)$$

168 As a result, the average amplitude ratio and strong phase difference between the  $b \rightarrow u$  and  
169  $b \rightarrow c$  transitions can be introduced as direct fit parameters instead of derived quantities  
170 that have to be calculated from Equation 2.11 after the fit. For the differential decay rate  
171 follows:

$$\begin{aligned} \frac{d\Gamma(\mathbf{x}, t, q, f)}{e^{-\Gamma_s t} dt d\Phi_4} \propto & (|\mathcal{A}_f^c(\mathbf{x})|^2 + r^2 |\mathcal{A}_f^u(\mathbf{x})|^2) \cosh \left( \frac{\Delta\Gamma_s t}{2} \right) \\ & + q f (|\mathcal{A}_f^c(\mathbf{x})|^2 - r^2 |\mathcal{A}_f^u(\mathbf{x})|^2) \cos (\Delta m_s t) \\ & - 2 r \operatorname{Re} (\mathcal{A}_f^c(\mathbf{x})^* \mathcal{A}_f^u(\mathbf{x}) e^{i\delta - if(\gamma - 2\beta_s)}) \sinh \left( \frac{\Delta\Gamma_s t}{2} \right) \\ & - 2 q f r \operatorname{Im} (\mathcal{A}_f^c(\mathbf{x})^* \mathcal{A}_f^u(\mathbf{x}) e^{i\delta - if(\gamma - 2\beta_s)}) \sin (\Delta m_s t) \end{aligned} \quad (2.29)$$

172 This renormalization procedure was found to be crucial for the fit stability since it reduces  
173 the correlation between the  $a_i^c$  and  $a_i^u$  amplitude coefficients significantly. Due to the  
174 overall normalization, one of the complex amplitude coefficients  $a_i^c$  can be fixed to unity  
175 and since  $r$  and  $\delta$  are included as fit parameters one of the complex amplitude coefficient  
176  $a_i^u$  can be additionally fixed to unity.

177 We force strong decays in the cascade topology to have the same pattern in  $b \rightarrow c$   
178 and  $b \rightarrow u$  transitions by the sharing of couplings between related quasi-two-body final  
179 states. For example, given the two  $a_i^c$  parameters required for  $B_s \rightarrow D_s^- K_1(1270)^+$   
180 with  $K_1(1270)^+ \rightarrow \rho(770)^0 \pi^+$  and  $K_1(1270)^+ \rightarrow K^*(892) \pi^+$ , the amplitude  $\bar{B}_s \rightarrow$   
181  $D_s^- K_1(1270)^+$  with  $K_1(1270)^+ \rightarrow \rho(770)^0 \pi^+$  and  $K_1(1270)^+ \rightarrow K^*(892) \pi^+$  only requires  
182 one additional global complex parameter to represent the different production processes  
183 of  $B_s \rightarrow D_s^- K_1(1270)^+$  and  $\bar{B}_s \rightarrow D_s^- K_1(1270)^+$ , while the relative magnitude and phase  
184 of  $K_1(1270)^+ \rightarrow \rho(770)^0 \pi^+$  and  $K_1(1270)^+ \rightarrow K^*(892) \pi^+$  are the same regardless of  
185 the production mechanism. For this purpose, multiple decay amplitudes of a three-body  
186 resonance are defined relative to a given reference channel.

## 187 2.4 Validation

188 The amplitude fit is performed by using the amplitude analysis tool **MINT2**. It was  
 189 previously applied to analyze  $D^0 \rightarrow 4\pi$  and  $D^0 \rightarrow KK\pi\pi$  decays [9] which have an  
 190 identical general spin structure (*i.e.* scalar to four scalar decay) to  $B_s \rightarrow D_s K\pi\pi$  decays.  
 191 In the course of the  $D^0 \rightarrow hhhh$  analysis, the implementation of the amplitudes were  
 192 extensively cross-checked against other available tools such as **qft++** [28], **AmpGen** [21]  
 193 and where possible **EVTGEN** [29]. Since no additional line shapes or spin factors are  
 194 needed for this analysis, we consider the amplitude calculation as fully validated.

195 This does, however, not apply to the full time-dependent amplitude pdf which is  
 196 newly implemented for this analysis. To cross-check it, we use **EVTGEN** to generate  
 197 toy events with time-dependent  $CP$  violation according to the **SSD\_Cp** event model [29].  
 198 Since this event model does not allow for multiple interfering resonances, we generate  
 199 only the decay chain  $B_s \rightarrow D_s(K_1(1400) \rightarrow K^*(892)\pi)$ . Table 2.1 lists the generated  
 200 input parameters. The toy data set is fitted with our **MINT2** implementation of the full  
 201 time-dependent amplitude pdf and the phasespace-integrated pdf. The fit projections are  
 202 shown in Figs. 2.1 and 2.2.

203 The  $CP$  coefficients  $C, D, \bar{D}, S, \bar{S}$  are the fit parameters in case of the phasespace-  
 204 integrated pdf, which are converted after to the fit to the physical observables  $r, \kappa, \delta$  and  $\gamma$   
 205 using the **GammaCombo** package [30]. The obtained 1-CL contours are shown in Fig. 2.3.  
 206 The full pdf determines  $r, \delta$  and  $\gamma$  directly. As shown in Tab. 2.2 and 2.3, the fit results  
 207 are in excellent agreement with the generated input values. The phasespace-integrated fit  
 208 is, in addition, performed with the **B2DX** fitter used for the  $B_s \rightarrow D_s K$  analysis yielding  
 209 identical results. Note though that some parts of the **B2DX** fitter have been taken over to  
 210 our **MINT2** fitter, such that the implementations are not fully independent.

**Table 2.1:** Input values used to generate **EVTGEN** toy events according to the **SSD\_Cp** event model.

$\tau$	1.5 ps
$\Delta\Gamma$	$-0.1 \text{ ps}^{-1}$
$\Delta m_s$	$17.757 \text{ ps}^{-1}$
$r$	0.37
$\kappa$	1
$\delta$	$10.0^\circ$
$\gamma$	$71.1^\circ$
$\beta_s$	$0.0^\circ$

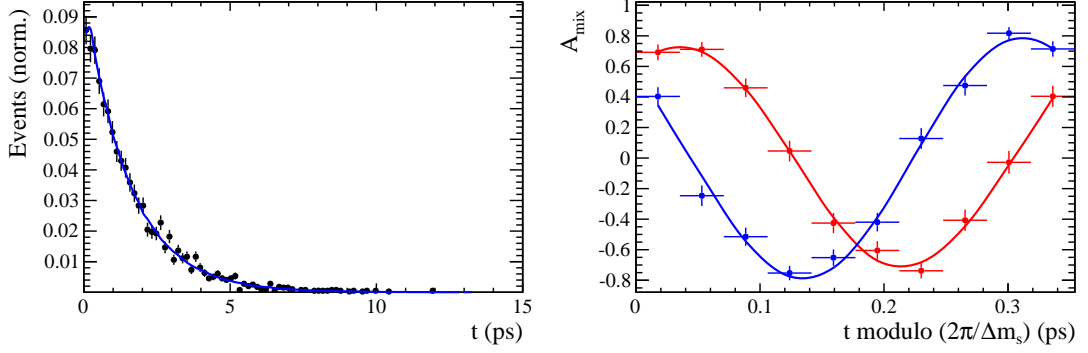


**Figure 2.1:** Left: Time distribution of  $B_s \rightarrow D_s K \pi \pi$  events generated with EVTGEN (points with error bars) and MINT2 fit projections (solid line). Right: Time-dependent asymmetry between mixed and unmixed events folded into one oscillation period for  $D_s^- K^+ \pi \pi$  (red) and  $D_s^+ K^- \pi \pi$  (blue) final states. The data points show events generated with EVTGEN, while the solid lines show the MINT2 fit projections.

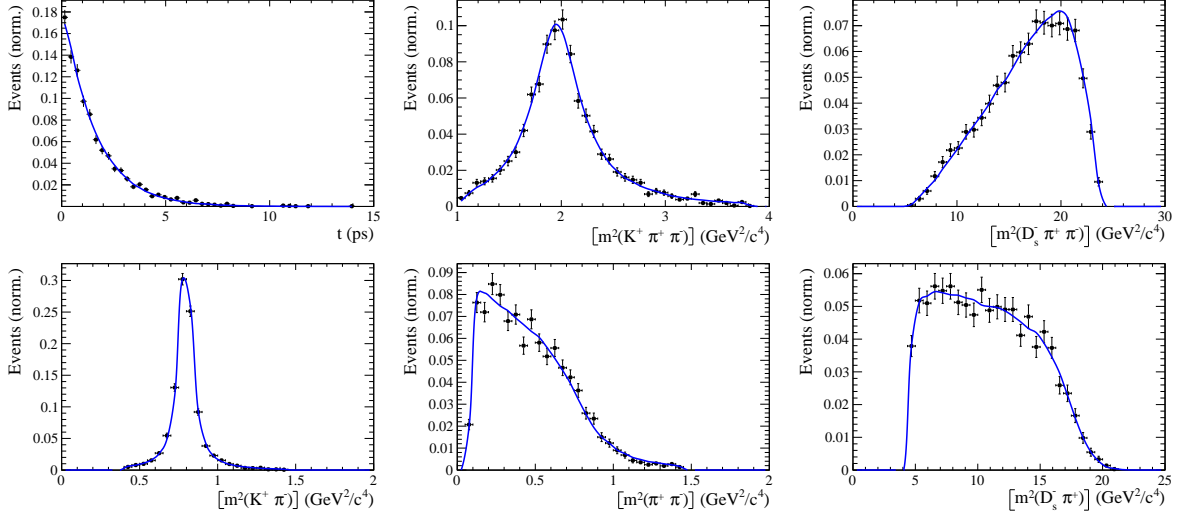


**Figure 2.2:** Time and invariant mass distributions of  $B_s \rightarrow D_s K \pi \pi$  events generated with EVTGEN (points with error bars) and MINT2 fit projections (blue solid line).

**Table 2.2:** Result of the phasespace-integrated fit to EVTGEN toy events.

	Generated	Fit result	Pull( $\sigma$ )
$C$	0.759	$0.763 \pm 0.026$	0.2
$D$	-0.314	$-0.376 \pm 0.227$	-0.3
$\bar{D}$	-0.101	$-0.261 \pm 0.246$	-0.7
$S$	-0.570	$-0.626 \pm 0.035$	1.6
$\bar{S}$	-0.643	$-0.669 \pm 0.035$	-0.7

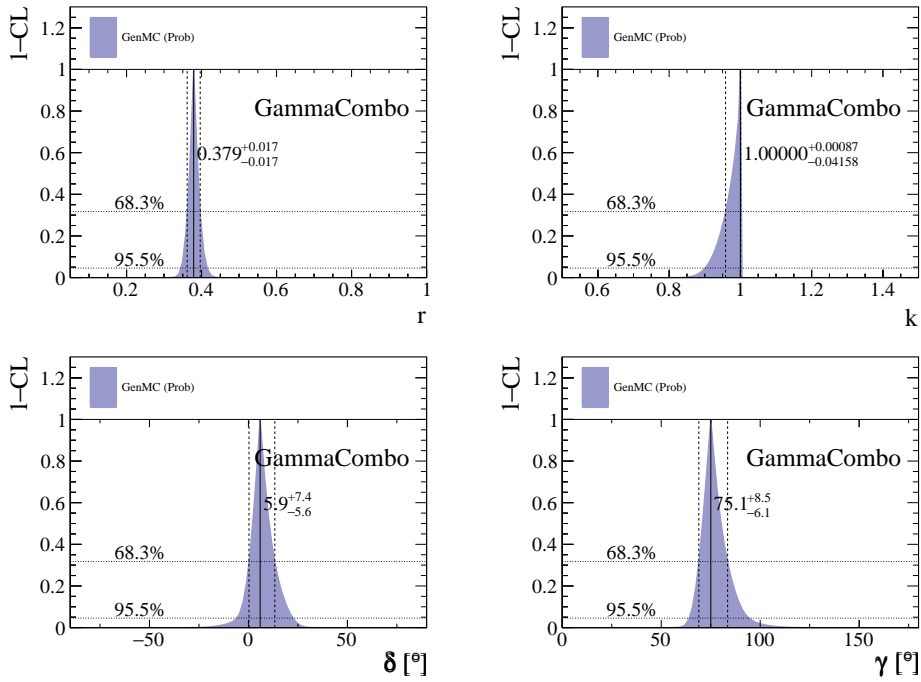


**Figure 2.3:** The 1-CL contours for the physical observable  $r, \kappa, \delta$  and  $\gamma$  obtained with the phasespace-integrated fit to the EVTGEN toy sample.

**Table 2.3:** Results for the physical observables obtained from fits to EVTGEN toy events.

	Generated	Full PDF	Phasespace-integrated
$r$	0.370	$0.379 \pm 0.021$	$0.379 \pm 0.017$
$\kappa$	1.0	1.0	$1.000 \pm 0.059$
$\delta$	$10.0^\circ$	$9.0 \pm 5.1$	$5.9 \pm 6.0$
$\gamma$	$71.1^\circ$	$67.3 \pm 5.9$	$75.1 \pm 6.9$

## 211 3 Data samples and event selection

### 212 3.1 Stripping and Trigger selection

213 The dataset used for this analysis corresponds to  $1 \text{ fb}^{-1}$  of proton-proton collision data col-  
214 lected in 2011 with a centre of mass energy  $\sqrt{s} = 7 \text{ TeV}$ ,  $2 \text{ fb}^{-1}$  collected in 2012 with  $\sqrt{s} =$   
215  $7 \text{ TeV}$  and  $4 \text{ fb}^{-1}$  collected in 2015/2016/2017 with  $\sqrt{s} = 13 \text{ TeV}$ . Candidate  $B_s^0 \rightarrow D_s K \pi \pi$   
216 ( $B_s^0 \rightarrow D_s \pi \pi \pi$ ) decays are reconstructed using the `B02DKPiPiD2HHHPIDBeauty2CharmLine`  
217 (`B02DPiPiD2HHHPIDBeauty2CharmLine`) line of the `BHadronCompleteEvent` stream of  
218 `Stripping21r1` (2011), `Stripping21` (2012), `Stripping24r1` (2015) and `Stripping28r1p1` (2016)  
219 and `Stripping29r2` (2017). Both stripping lines employ the same selection cuts, listed in  
220 Appendix A, except for the PID requirement on the bachelor kaon/pion.

221 Events that pass the stripping selection are further required to fulfill the following  
222 trigger requirements: at the hardware stage, the  $B_s^0$  candidates are required to be TOS  
223 on the `L0Hadron` trigger or TIS on `L0Global`; at Hlt1,  $B_s^0$  candidates are required to be  
224 TOS on the `Hlt1TrackAllL0` (`Hlt1TrackMVA` or `Hlt1TwoTrackMVA`) trigger line for Run-I  
225 (Run-II) data; at Hlt2, candidates have to be TOS on either one of the 2, 3 or 4-body  
226 topological trigger lines or the inclusive  $\phi$  trigger. More details on the used HLT lines are  
227 given in Appendix A.

228 Due to a residual kinematic dependence on whether the event is triggered by `L0Hadron`  
229 or not and on the data taking condition, the analysis is performed in four disjoint categories:  
230 `[Run-I,L0-TOS]`, `[Run-I,L0-TIS]`, `[Run-II,L0-TOS]` and `[Run-II,L0-TIS]`, where for simplic-  
231 ity we denote `L0Hadron-TOS` as `L0-TOS` and (`L0Global-TIS` and not `L0Hadron-TOS`) as  
232 `L0-TIS`.

### 233 3.2 Offline selection

234 The offline selection, in particular the requirements on the  $D_s$  hadron, are guided by  
235 the previous analyses of  $B_s \rightarrow D_s K/\pi$ ,  $B_d \rightarrow D^0 \pi$  as well as the branching fraction  
236 measurement of  $B_s^0 \rightarrow D_s K \pi \pi$  decays. Tables 3.1 and 3.2 summarize all selection  
237 requirements which are described in the following. Throughout the note, we abbreviate  
238  $B_s^0 \rightarrow D_s X_s (\rightarrow K \pi \pi)$  and  $B_s^0 \rightarrow D_s X_d (\rightarrow \pi \pi \pi)$ .

239 Given the high number of  $pp$  interactions per bunch crossing, a large fraction of  
240 events have more than one reconstructed PV. We choose the 'best' PV to be the one  
241 to which the  $B_s$  candidate has the smallest  $\chi_{IP}^2$ . In instances where the association  
242 of the  $B_s$  candidate to the best PV is wrong, the decay time of this candidate will be  
243 incorrect. These wrongly associated candidates are rejected by requiring that the  $B_s$   
244  $\chi_{IP}^2$  with respect to any other PV is sufficiently higher than with respect to the best PV  
245 ( $\Delta\chi_{IP}^2 = \chi_{IP,\text{SECONDBEST}}^2 - \chi_{IP,\text{BEST}}^2 > 20$ ). Events with only a single PV are not affected.

246 In order to clean up the sample and to align the Run-I to the slightly tighter Run-II  
247 stripping selection, we apply the following loose cuts to the b-hadron:

- 248 • DIRA > 0.99994
- 249 • min IP  $\chi^2 < 16$  to the best PV,
- 250 • FD  $\chi^2 > 100$  to the best PV,
- 251 • Vertex  $\chi^2/\text{nDoF} < 8$ .

252 The cut on the  $B_s$  decay-time is tightened with respect to the stripping selection ( $t > 0.2$  ps)  
253 because, while offline we use the decay-time determined for a DTF in which the PV position,  
254 the  $D_s$  and the  $B_s$  mass are constrained, in the stripping the simple decay-time returned  
255 by a kinematic fit is used. The difference between these two decay-times extends up to 0.1  
256 ps, thus cutting at 0.4 ps avoids any boundary effects and simplifies the time-acceptance  
257 studies. We further remove outliers with poorly estimated decay times ( $\delta t < 0.15$  ps).

258 We reconstruct the  $B_s^0 \rightarrow D_s h\pi\pi$  decay through three different final states of the  
259  $D_s$  meson:  $D_s \rightarrow KK\pi$ ,  $D_s \rightarrow \pi\pi\pi$  and  $D_s \rightarrow K\pi\pi$ . Of those,  $D_s \rightarrow KK\pi$  is the  
260 most prominent one, while  $\mathcal{BR}(D_s \rightarrow \pi\pi\pi) \approx 0.2 \cdot \mathcal{BR}(D_s \rightarrow KK\pi)$  and  $\mathcal{BR}(D_s \rightarrow$   
261  $K\pi\pi) \approx 0.12 \cdot \mathcal{BR}(D_s \rightarrow KK\pi)$  holds for the others. For the  $KK\pi$  final state we make  
262 use of the well known resonance structure; the decay proceeds either via the narrow  $\phi$   
263 resonance, the broader  $K^{*0}$  resonance or (predominantly) non-resonant. Within the  $\phi$   
264 resonance region the sample is already sufficiently clean after the stripping so that we  
265 do not impose additional criteria on the  $D_s$  daughters. For the  $K^{*0}$  and non-resonant  
266 regions consecutively tighter requirements on the particle identification and the  $D_s$  flight-  
267 distance are applied. We apply global requirements for the other final states. All cuts are  
268 summarized in Table 3.1.

### 269 3.2.1 Phase space region

270 Due to the comparably low masses of the final state particles with respect to the  $B_s$   
271 mass, there is, in contrast to for example b-hadron to charmonia or charm decays, a  
272 huge phase-space available for the  $B_s^0 \rightarrow D_s K\pi\pi$  decay. For the invariant mass of  
273 the  $K\pi\pi$  subsystem it extends up to 3.4 GeV. It has however been observed that the  
274 decay proceeds predominantly through the low lying axial vector states  $K_1(1270)$  and  
275  $K_1(1400)$ , while the combinatorial background is concentrated at high  $K\pi\pi$  invariant  
276 masses ( $m(K\pi\pi) > 2000$  MeV). Moreover, the strange hadron spectrum above 2 GeV  
277 is poorly understood experimentally such that a reliable extraction of the strong phase  
278 motion in that region is not possible. We consequently choose to limit the considered  
279 phase space region to  $m(K\pi\pi) < 1950$  MeV, which is right below the charm-strange  
280 threshold ( $B_s^0 \rightarrow D_s^+ D_s^-$ ).

281 **3.2.2 Physics background vetoes**

282 We veto various physical backgrounds, which have either the same final state as our  
 283 signal decay, or can contribute via a single misidentification of  $K \leftrightarrow \pi$ ,  $K \leftrightarrow p$  or  $\pi \leftrightarrow p$ .  
 284 Depending on the  $D_s$  final state different vetoes are applied in order to account for peaking  
 285 backgrounds originating from charm meson or charmed baryon decays.

286 1.  $D_s^- \rightarrow K^+ K^- \pi^-$

287 (a)  $D^- \rightarrow K^+ \pi^- \pi^-$ :

288 Possible with  $\pi^- \rightarrow K^-$  misidentification, vetoed by requiring  $m(K^+ K_\pi^- \pi^-) \neq$   
 289  $m(D^-) \pm 40$  MeV or the  $K^-$  has to fulfill more stringent PID criteria depending  
 290 on the resonant region (see Table 3.1).

291 (b)  $\Lambda_c^- \rightarrow K^+ \bar{p} \pi^-$ :

292 Possible with  $\bar{p} \rightarrow K^-$  misidentification, vetoed by requiring  $m(K^+ K_p^- \pi^-) \neq$   
 293  $m(\Lambda_c^-) \pm 40$  MeV or the  $K^-$  has to fulfill more stringent PID criteria depending  
 294 on the resonant region (see Table 3.1).

295 (c)  $D^0 \rightarrow KK$ :

296  $D^0$  combined with a random  $\pi$  can fake a  $D_s \rightarrow KK\pi$  decay, vetoed by  
 297 requiring  $m(KK) < 1840$  MeV.

298 2.  $D_s^- \rightarrow \pi^+ \pi^- \pi^-$

299 (a)  $D^0 \rightarrow \pi\pi$ :

300  $D^0$  combined with a random  $\pi$  can fake a  $D_s \rightarrow \pi\pi\pi$  decay, vetoed by requiring  
 301 both possible combinations to have  $m(\pi\pi) < 1700$  MeV.

302 3.  $D_s^- \rightarrow K^- \pi^+ \pi^-$

303 (a)  $D^- \rightarrow \pi^- \pi^+ \pi^-$ :

304 Possible with  $\pi^- \rightarrow K^-$  misidentification, vetoed by requiring  $m(K_\pi^- \pi^+ \pi^-) \neq$   
 305  $m(D^-) \pm 40$  MeV or  $\text{PIDK}(K^+) > 15$ .

306 (b)  $\Lambda_c^- \rightarrow \bar{p} \pi^+ \pi^-$ :

307 Possible with  $\bar{p} \rightarrow K^-$  misidentification, vetoed by requiring  $m(K_p^- \pi^+ \pi^-) \neq$   
 308  $m(\Lambda_c^-) \pm 40$  MeV or  $\text{PIDK}(K^-) - \text{PIDp}(K^-) > 5$ .

309 (c)  $D^0 \rightarrow K\pi$ :

310  $D^0$  combined with a random  $\pi$  can fake a  $D_s \rightarrow K\pi\pi$  decay, vetoed by requiring  
 311 both possible combinations to have  $m(K\pi) < 1750$  MeV.

312 The effects of these veto cuts are illustrated in Figs. 3.1,3.2 and 3.3. To reduce cross-feed  
 313 from our calibration channel into the signal channel and vice-versa we require tight PID  
 314 cuts on the ambiguous bachelor kaon ( $\text{PIDK}(K) > 10$ )/pion ( $\text{PIDK}(K) < 0$ ). In addition,  
 315 we veto  $B_s^0 \rightarrow D_s^- D_s^+$  decays which is illustrated in Fig. 3.4.

- 316 1.  $X_s^+ \rightarrow K^+\pi^+\pi^-$ :
- 317 (a)  $B_s^0 \rightarrow D_s\pi\pi\pi$ :  
318 Possible with  $\pi^+ \rightarrow K^+$  misidentification, suppressed with  $\text{PIDK}(K^+) > 10$ .
- 319 (b)  $B_s^0 \rightarrow D_s^-(D_s^+ \rightarrow K^+\pi^+\pi^-)$ :  
320 Outside of considered phase-space region, see Sec. 3.2.1.
- 321 (c)  $B_s^0 \rightarrow D_s^-(D_s^+ \rightarrow K^+K^-\pi^+)$ :  
322 To suppress  $B_s^0 \rightarrow D_s^-K^+K^-\pi^+$  background, possible with  $K^- \rightarrow \pi^-$  misiden-  
323 tification, we require  $\text{PIDK}(\pi^-) < 0$ . In case the invariant mass of the  $K^+\pi^+\pi^-$   
324 system recomputed applying the kaon mass hypothesis to the pion is close to  
325 the  $D_s$  mass ( $m(K^+\pi^+\pi_K^-) = m(D_s) \pm 20$  MeV), we further tighten the cut to  
326  $\text{PIDK}(\pi^-) < -5$ .
- 327 2.  $X_d^+ \rightarrow \pi^+\pi^+\pi^-$ :
- 328 (a)  $B_s^0 \rightarrow D_s K\pi\pi$ :  
329 Possible with single missID of  $K^+ \rightarrow \pi^+$ , suppressed with  $\text{PIDK}(\pi^+) < 0$ .
- 330 (b)  $B_s^0 \rightarrow D_s^-(D_s^+ \rightarrow \pi^+\pi^+\pi^-)$ :  
331 Outside of considered phase-space region, see Sec. 3.2.1.
- 332 (c)  $B_s^0 \rightarrow D_s^-(D_s^+ \rightarrow K^+\pi^-\pi^+)$ :  
333 Possible with single missID of  $K^+ \rightarrow \pi^+$ , vetoed by requiring  $m(\pi^+\pi_K^+\pi^-) \neq$   
334  $m(D_s) \pm 20$  MeV or  $\text{PIDK}(\pi^+) < -5$  for both  $\pi^+$ .

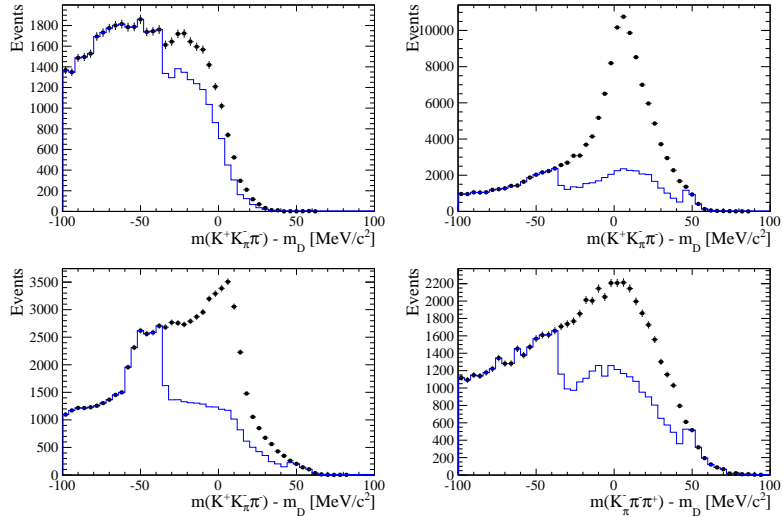


**Figure 3.1:** Background contributions from  $D^-$  decays where the  $\pi^-$  is misidentified as  $K^-$ . The  $D_s$  invariant mass is recomputed applying the pion mass hypothesis to the kaon and shown for the  $D_s \rightarrow \phi\pi$ ,  $D_s \rightarrow K^*(892)K$ ,  $D_s \rightarrow KK\pi$  (non-resonant) and  $D_s \rightarrow K\pi\pi$  final state categories from top-left to bottom-right. The distributions are shown without (black) and with (blue) the  $D^-$ -veto applied.

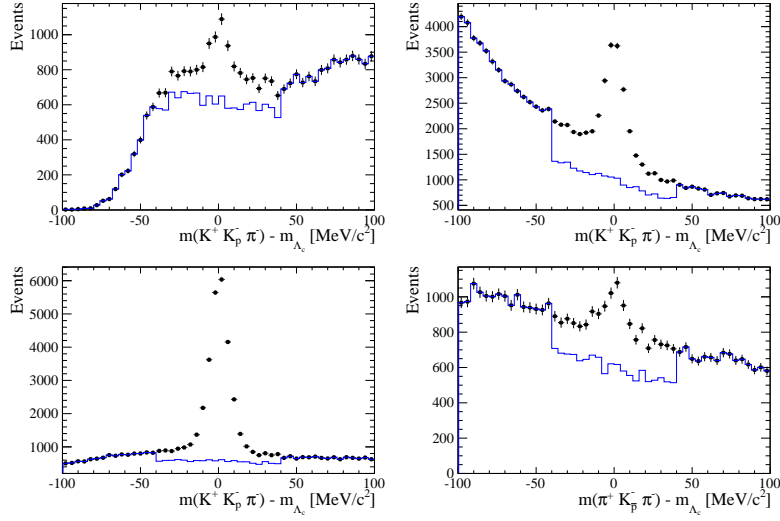


**Figure 3.2:** Background contributions from  $\Lambda_c$  decays where the  $\bar{p}$  is misidentified as  $K^-$ . The  $D_s$  invariant mass is recomputed applying the proton mass hypothesis to the kaon and shown for the  $D_s \rightarrow \phi\pi$ ,  $D_s \rightarrow K^*(892)K$ ,  $D_s \rightarrow KK\pi$  (non-resonant) and  $D_s \rightarrow K\pi\pi$  final state categories from top-left to bottom-right. The distributions are shown without (black) and with (blue) the  $\Lambda_c$ -veto applied.

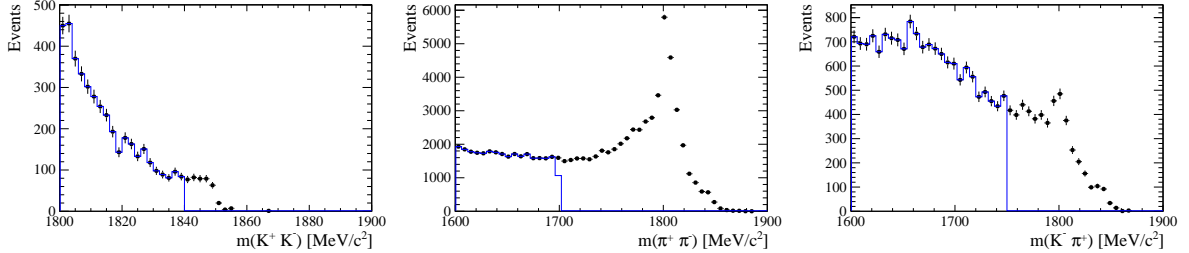


**Figure 3.3:** Background contributions to  $D_s \rightarrow KK\pi$  (left),  $D_s \rightarrow \pi\pi\pi$  (middle) and  $D_s \rightarrow K\pi\pi$  (right) from  $D^0 \rightarrow hh$  decays combined with a random pion.

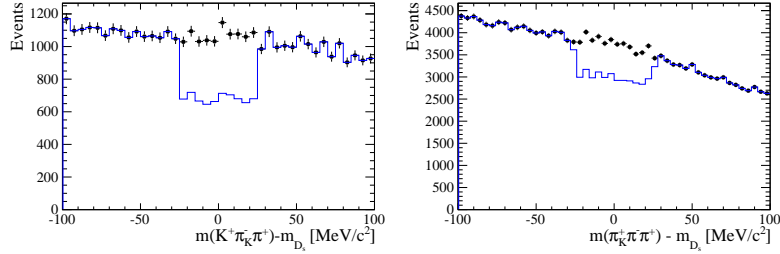


**Figure 3.4:** Background contributions to  $B_s \rightarrow D_s K\pi\pi$  (left) and  $B_s \rightarrow D_s \pi\pi\pi$  (right) from  $B_s \rightarrow D_s D_s$  decays where the kaon is misidentified as pion. The  $X_{s,d}$  invariant mass is recomputed applying the kaon mass hypothesis to the pion and shown without (black) and with (blue) the  $D_s$ -veto applied.

335 **3.2.3 Training of multivariate classifier**

336 The Toolkit for Multivariate Analysis (TMVA [31]) is used to train a multivariate classifier  
337 (BDT with gradient boosting, BDTG) discriminating signal and combinatorial background.  
338 We use  $B_s \rightarrow D_s \pi\pi$  data that passes the preselection as signal proxy. The background  
339 is statistically subtracted by applying `sWeights` based on the fit to the reconstructed  $B_s$   
340 mass shown in Fig. 3.5. This is a simplified version (performed in a reduced mass range)  
341 of the final mass fits described in Sec. 4. The sideband data ( $m(B_s) > 5500$  MeV) is used  
342 as background proxy.

343 Training the classifier on a sub-sample which is supposed to be used in the final analysis  
344 might cause a bias, as the classifier selects, in case of overtraining, the training events  
345 more efficiently. As overtraining can not be completely avoided, we split the signal and  
346 the background training samples into two disjoint subsamples according to whether the  
347 event number is even or odd. We then train the classifier on the even sample and apply it  
348 to the odd one, and vice-versa (cross-training).

349 The following discriminating variables are used for the BDTG training:

- 350 • logarithm of the  $B_s$  impact-parameter  $\chi^2$ ,  $B_s \log(\chi_{IP}^2)$
- 351 • logarithm of the cosine of the  $B_s$  direction angle,  $\log(\text{DIRA})$
- 352 • fit quality of the DTF with PV constrain,  $\chi_{DTF}^2/ndf$
- 353 • logarithm of the minimal vertex quality difference for adding one extra track,  
354  $\log(\Delta\chi_{add-track}^2)$
- 355 • the asymmetry between the transverse momentum of the  $B_s$ - candidate and the  
356 transverse momentum of all the particles reconstructed with a cone of radius  
357  $r = \sqrt{(\Delta\Phi)^2 + (\Delta\eta)^2} < 1$  rad around the  $B_s$ - candidate,  $B_s A_{pT}^{\text{cone}}$
- 358 • largest ghost probability of all tracks,  $\max(\text{ghostProb})$
- 359 • logarithm of the the smallest  $X_s$  daughter impact-parameter  $\chi^2$ ,  $X_s \log(\min(\chi_{IP}^2))$
- 360 • largest distance of closest approach of the  $X_s$  daughters,  $\max(\text{DOCA})$
- 361 • cosine of the largest opening angle between the  $D_s$  and another bachelor track  $h_i$  in  
362 the plane transverse to the beam,  $\cos(\max \theta_{D_s h_i})$
- 363 • logarithm of the the smallest  $D_s$  daughter impact-parameter  $\chi^2$ ,  $D_s \log(\min(\chi_{IP}^2))$
- 364 • logarithm of the  $D_s$  flight-distance significance,  $D_s \log(\chi_{FD}^2)$
- 365 • logarithm of the  $D_s$  radial flight-distance,  $D_s \log(RFD)$

366 Loose cuts on the variables  $\chi_{DTF}^2/ndf$ ,  $\Delta\chi_{add-track}^2$  and  $\cos(\max \theta_{D_s h_i})$  are applied prior  
367 to the training which are expected to be 100% signal efficient. Figure 3.6 shows the  
368 distributions of the input variables for signal and background. As shown in Appendix B,  
369 these distributions differ between data-taking period and trigger category. In particular  
370 variables depending on the  $B_s$  kinematics and the event multiplicity are affected (e.g.  
371  $\theta_{D_s h_i}$  or  $A_{pT}^{\text{cone}}$ ). The BDTG is consequently trained separately for these categories. The  
372 resulting classifier response is shown in Fig. 3.7 for each category (even and odd test  
373 samples combined) and in Appendix B for each training.

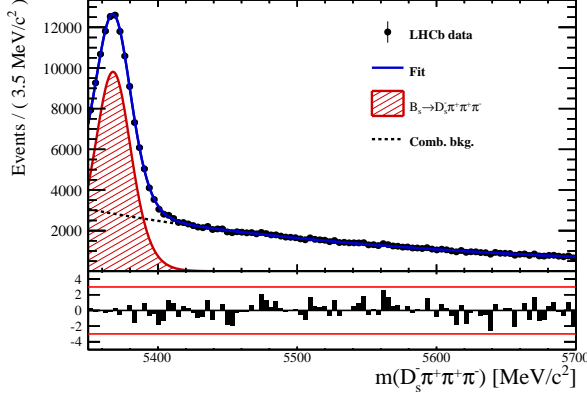


**Figure 3.5:** Reconstructed  $B_s$  mass for  $B_s \rightarrow D_s \pi\pi\pi$  events that pass the preselection. The fitted PDF is shown in blue, the signal component in red and the background component in black.

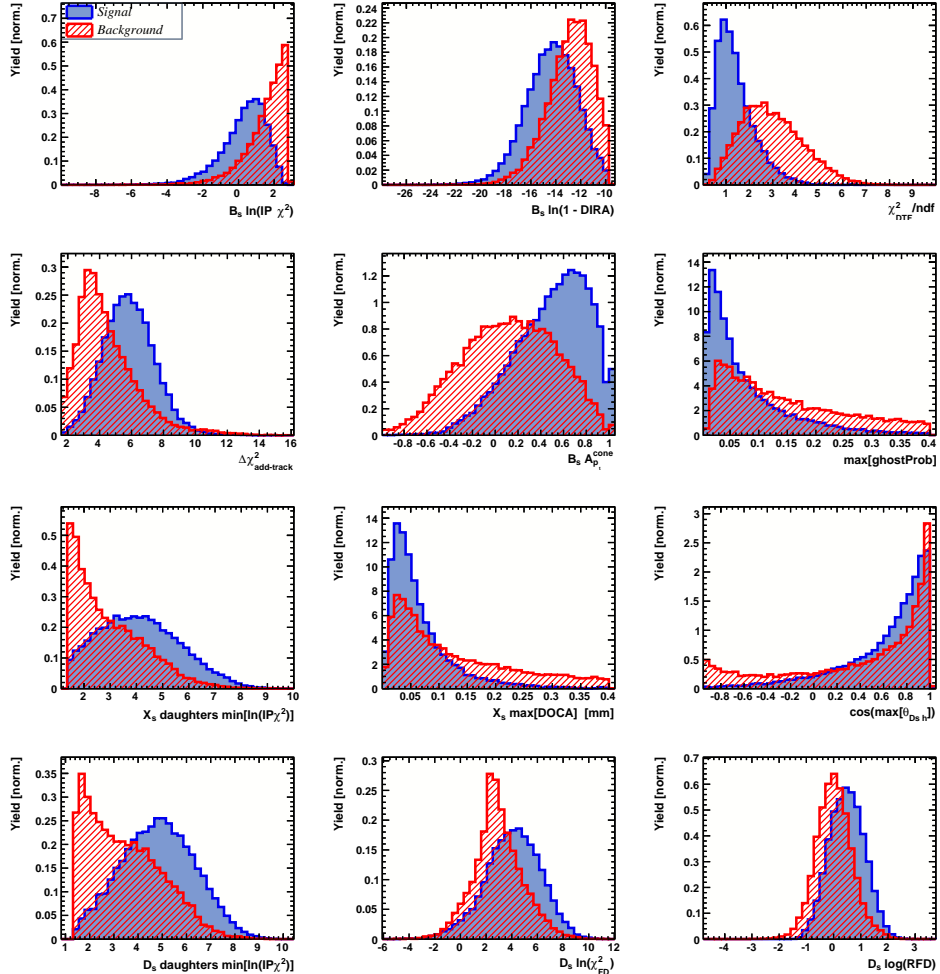


**Figure 3.6:** Discriminating variables used to train the BDTG for all data categories combined.

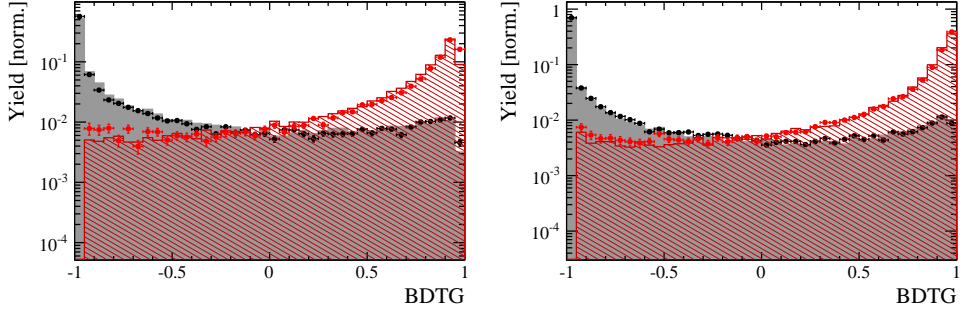


**Figure 3.7:** Signal (red) and background (black) distributions for the BDTG response for Run-I (left) and Run-II (right) data. Filled histograms (data points) show the BDTG response for the L0-TOS (L0-TIS) category. Even and odd test samples are combined.

### 3.2.4 Final selection

The cut on the BDTG output is optimized using the signal significance as figure of merit:

$$\text{FOM}(\text{BDTG}) = \frac{N_s(\text{BDTG})}{\sqrt{N_s(\text{BDTG}) + N_b(\text{BDTG})}} \quad (3.1)$$

where  $N_s(\text{BDTG})$  is the  $B_s \rightarrow D_s K\pi\pi$  signal yield for a given BDTG cut and  $N_b(\text{BDTG})$  is the combinatorial background yield in the signal region ( $m(D_s K\pi\pi) = m_{B_s} \pm 40 \text{ MeV}$ ). To compute the yields as function of the BDTG cut, we use the BDTG efficiencies,  $\epsilon_{s,b}$ , evaluated on the corresponding test samples. To fix the overall scale, it is required to know the yields at (at least) one point of the scanned range. We arbitrarily choose this fix point to be  $\text{BDTG} > 0$  and perform a fit to the reconstructed  $B_s$  mass as described in Sec. 4 to obtain the yields  $N_{s,b}(0)$ . These yields are then efficiency corrected to calculate the yields for a given BDTG cut:

$$N_{s,b}(\text{BDTG}) = N_{s,b}(0) \cdot \frac{\epsilon_{s,b}(\text{BDTG})}{\epsilon_{s,b}(0)}. \quad (3.2)$$

Figure 3.8 shows the resulting BDTG scans for each training category.

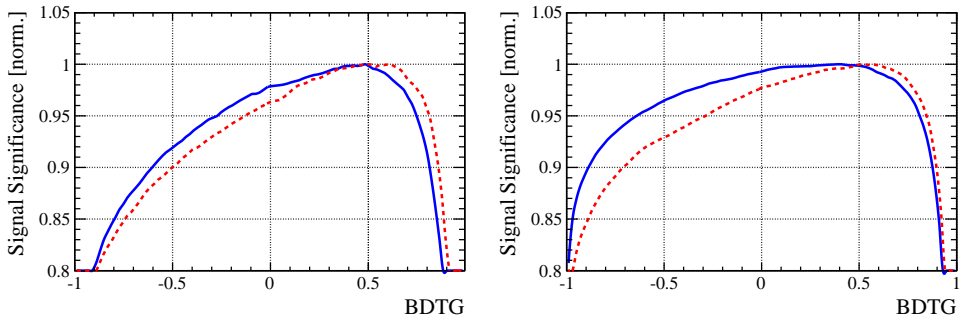


**Figure 3.8:** Signal significance as function of the applied cut on the BDTG response for Run-I (left) and Run-II (right) data. The scans for the L0-TOS (L0-TIS) category are shown in blue (red). The signal significance is normalized to be 1 at the optimal BDTG cut value.

**Table 3.1:** Offline selection requirements for  $D_s \rightarrow 3h$  candidates.

	Description	Requirement
$D_s \rightarrow hh\bar{h}$	$m(hh\bar{h})$	$= m_{D_s} \pm 25$ MeV
$D_s^- \rightarrow KK\pi^-$	$D^0$ veto	$m(KK) < 1840$ MeV
$D_s^- \rightarrow \phi\pi^-$	$m(KK)$ PIDK( $K^+$ ) PIDK( $K^-$ ) PIDK( $\pi^-$ ) $\chi_{FD}^2$ FD in $z$ $D^-$ veto $\Lambda_c$ veto	$= m_\phi \pm 12$ MeV $> -10$ $> -10$ $< 20$ $> 0$ $> -1$ $m(K^+K_\pi^-\pi^-) \neq m(D^-) \pm 40$ MeV    PIDK( $K^-$ ) $> 5$ $m(K^+K_p^-\pi^-) \neq m(\Lambda_c) \pm 40$ MeV    PIDK( $K^-$ ) – PIDp( $K^-$ ) $> 2$
$D_s^- \rightarrow K^*(892)K^-$	$m(KK)$ $m(K^+\pi^-)$ PIDK( $K^+$ ) PIDK( $K^-$ ) PIDK( $\pi^-$ ) $\chi_{FD}^2$ FD in $z$ $D^-$ veto $\Lambda_c$ veto	$\neq m_\phi \pm 12$ MeV $= m_{K^*(892)} \pm 75$ MeV $> -10$ $> -5$ $< 10$ $> 0$ $> 0$ $m(K^+K_\pi^-\pi^-) \neq m(D^-) \pm 40$ MeV    PIDK( $K^-$ ) $> 15$ $m(K^+K_p^-\pi^-) \neq m(\Lambda_c) \pm 40$ MeV    PIDK( $K^-$ ) – PIDp( $K^-$ ) $> 5$
$D_s^- \rightarrow (KK\pi^-)_{NR}$	$m(KK)$ $m(K^+\pi^-)$ PIDK( $K^+$ ) PIDK( $K^-$ ) PIDK( $\pi^-$ ) $\chi_{FD}^2$ FD in $z$ $D^-$ veto $\Lambda_c$ veto	$\neq m_\phi \pm 12$ MeV $\neq m_{K^*(892)} \pm 75$ MeV $> 5$ $> 5$ $< 10$ $> 4$ $> 0$ $m(K^+K_\pi^-\pi^-) \neq m(D^-) \pm 40$ MeV    PIDK( $K^-$ ) $> 15$ $m(K^+K_p^-\pi^-) \neq m(\Lambda_c) \pm 40$ MeV    PIDK( $K^-$ ) – PIDp( $K^-$ ) $> 5$
$D_s \rightarrow \pi\pi\pi$	PIDK( $\pi$ ) PIDp( $\pi$ ) $D^0$ veto $\chi_{FD}^2$ FD in $z$	$< 10$ $< 20$ $m(\pi^+\pi^-) < 1700$ MeV $> 9$ $> 0$
$D_s^- \rightarrow K^-\pi^+\pi^-$	PIDK( $K$ ) PIDK( $\pi$ ) PIDp( $\pi$ ) $D^0$ veto $\chi_{FD}^2$ FD in $z$ $D^-$ veto $\Lambda_c$ veto	$> 8$ $< 5$ $< 20$ $m(K^-\pi^+) < 1750$ MeV $> 9$ $> 0$ $m(K_\pi^-\pi^+\pi^-) \neq m(D^-) \pm 40$ MeV    PIDK( $K^-$ ) $> 15$ $m(K_p^-\pi^+\pi^-) \neq m(\Lambda_c) \pm 40$ MeV    PIDK( $K^-$ ) – PIDp( $K^-$ ) $> 5$

**Table 3.2:** Offline selection requirements for  $B_s \rightarrow D_s K\pi\pi(D_s\pi\pi\pi)$  candidates.

	Description	Requirement
$B_s \rightarrow D_s h\pi\pi$	$m(D_s h\pi\pi)$	$> 5200 \text{ MeV}$
	$\chi^2_{vtx}/\text{ndof}$	$< 8$
	DIRA	$> 0.99994$
	$\chi^2_{FD}$	$> 100$
	$\chi^2_{IP}$	$< 16$
	$\chi^2_{DTF}/\text{ndof}$	$< 15$
	$\Delta\chi^2_{add-track}$	$> 2$
	$\cos(\max \theta_{D_s h_i})$	$> -0.9$
	$t$	$> 0.4 \text{ ps}$
	$\delta t$	$< 0.15 \text{ ps}$
	Phasespace region	$m(h\pi\pi) < 1.95 \text{ GeV}$ $m(h\pi) < 1.2 \text{ GeV}$ $m(\pi\pi) < 1.2 \text{ GeV}$
Wrong PV veto		$\text{nPV} = 1 \parallel \min(\Delta\chi^2_{IP}) > 20$
BDTG		$> 0.45 \text{ [Run-I,L0-TOS]}$ $> 0.50 \text{ [Run-I,L0-TIS]}$ $> 0.35 \text{ [Run-II,L0-TOS]}$ $> 0.50 \text{ [Run-II,L0-TIS]}$
$X_s^+ \rightarrow K^+\pi^+\pi^-$	PIDK(K)	$> 10$
	PIDK( $\pi^+$ )	$< 10$
	PIDK( $\pi^-$ )	$< 0$
	$D_s$ veto	$m(K^+\pi^+\pi_K^-) \neq m(D_s) \pm 20 \text{ MeV} \parallel \text{PIDK}(\pi^-) < -5$
$X_d^+ \rightarrow \pi^+\pi^+\pi^-$	PIDK( $\pi^+$ )	$< 0$
	PIDK( $\pi^-$ )	$< 10$
	$D_s$ veto	$m(\pi^+\pi_K^+\pi^-) \neq m(D_s) \pm 20 \text{ MeV} \parallel \text{PIDK}(\pi^+) < -5$
All tracks	hasRich	$= 1$

## 385 4 Yields determination

386 An extended unbinned maximum likelihood fit to the reconstructed  $B_s$  mass of the selected  
 387 events is performed in order to determine the signal and background yields. The invariant  
 388 mass  $m(D_s h\pi\pi)$  is determined from a DTF constraining the mass of the  $D_s$  to the PDG  
 389 value and the position of the PV. The probability density functions (PDFs) used to  
 390 describe the signal and background components are described in the following.

391 Due to different mass resolutions, we perform the invariant mass fits simultaneously  
 392 for each data-taking period and each trigger category. We further introduce four  $D_s$  final  
 393 state categories:  $D_s \rightarrow \phi\pi$ ,  $D_s \rightarrow K^*(892)\pi$ ,  $D_s \rightarrow \pi\pi\pi$  and  $D_s \rightarrow Kh\pi$  to account for  
 394 different signal purities. The  $D_s \rightarrow Kh\pi$  category combines the two  $D_s$  decay channels  
 395 with the lowest statistics:  $D_s \rightarrow KK\pi$  (non-resonant) and  $D_s \rightarrow K\pi\pi$ . This amounts to  
 396 16 categories in total.

### 397 4.1 Signal model

398 The signal  $B_s$ -mass distribution of both  $B_s^0 \rightarrow D_s K\pi\pi$  and  $B_s^0 \rightarrow D_s \pi\pi\pi$  is modeled  
 399 using a Johnson's SU function [32], which results from a variable transformation of a  
 400 normal distribution to allow for asymmetric tails:

$$\mathcal{J}(x|\mu, \sigma, \nu, \tau) = \frac{e^{-\frac{1}{2}r^2}}{2\pi \cdot c \cdot \sigma \cdot \tau \cdot \sqrt{z^2 + 1}} \quad (4.1)$$

$$r = -\nu + \frac{\operatorname{asinh}(z)}{\tau} \quad (4.2)$$

$$z = \frac{x - (\mu - c \cdot \sigma \cdot e^\tau \sinh(\nu \cdot \tau))}{c \cdot \tau} \quad (4.3)$$

$$c = \frac{e^{\tau^2} - 1}{2\sqrt{e^{\tau^2} \cdot \cosh(2\nu \cdot \tau) + 1}}. \quad (4.4)$$

401 It is conveniently expressed in terms of the central moments up to order four: The mean  
 402 of the distribution  $\mu$ , the standard deviation  $\sigma$ , the skewness  $\nu$  and the kurtosis  $\tau$ . The  
 403 tail parameters  $\nu$  and  $\tau$  are fixed to the values obtained by a fit to the invariant mass  
 404 distribution of simulated events shown in Fig 4.1. To account for differences between

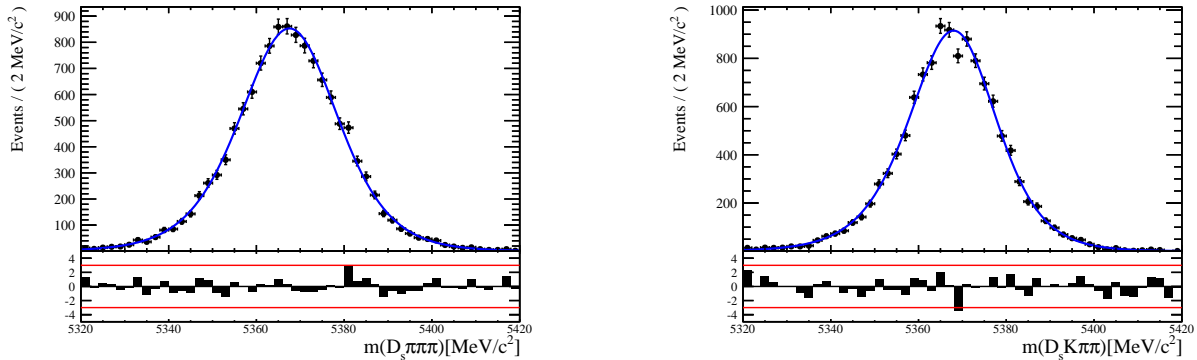


**Figure 4.1:** Invariant mass distributions of simulated (left)  $B_s^0 \rightarrow D_s \pi\pi\pi$  and (right)  $B_s^0 \rightarrow D_s K\pi\pi$  events. A fit with a Johnson's SU PDF is overlaid.

405 simulation and real data, linear scaling factors for the mean  $\mu$  and width  $\sigma$  are determined  
406 in the fit to  $B_s^0 \rightarrow D_s\pi\pi\pi$  data and later fixed in the fit to  $B_s^0 \rightarrow D_sK\pi\pi$  decays. The scale  
407 factors are determined separately for each data-taking period and each trigger category.

## 408 4.2 Background models

409 After the full selection the following residual background components have to be accounted  
410 for:

### 411 Combinatorial background

412 The combinatorial background is described by a second order polynomial, whose  
413 parameters are determined, for each  $D_s$  final state separately, in the fit to data. For  
414 systematic studies an exponential PDF is used.

### 415 Peaking $B_d$ background

416 Decays of  $B_d$  mesons into the  $D_sh\pi\pi$  final state are described by the  $B_s$  signal PDF  
417 where the mean is shifted by the known mass difference  $m_{B_s} - m_{B_d}$  [12].

### 418 Partially reconstructed background

419 Partially reconstructed  $B_s^0 \rightarrow D_s^*\pi\pi\pi$  decays, with  $D_s^* \rightarrow D_s\gamma$  or  $D_s^* \rightarrow D_s\pi^0$ , are expected  
420 to be peaking lower than signal in the  $m(D_s\pi\pi\pi)$  spectrum with large tails due to the  
421 momentum carried away by the not reconstructed  $\pi^0$  or  $\gamma$ . An empirical description for  
422 the shape of this contribution is derived from a  $B_s^0 \rightarrow D_s^*\pi\pi\pi$  MC sample subject to  
423 the nominal  $B_s^0 \rightarrow D_s\pi\pi\pi$  selection. Figure 4.2 (left) shows the respective reconstructed  
424  $m(D_s\pi\pi\pi)$  distribution. A sum of three bifurcated Gaussian functions is used to describe  
425 it. In the fit to data, all parameters are fixed to the ones obtained from MC except for  
426 the parameter which describes the width of the right tail of the distribution to account for  
427 data-simulation differences in mass resolution. The equivalent  $B_s^0 \rightarrow D_s^*K\pi\pi$  component  
428 contributing to the  $B_s^0 \rightarrow D_sK\pi\pi$  data sample is described by the same PDF with the  
429 right tail fixed to the  $B_s^0 \rightarrow D_s\pi\pi\pi$  result.

430 Contributions from  $B^0 \rightarrow D_s^*K\pi\pi$  decays are modeled with the  $B_s^0 \rightarrow D_s^*K\pi\pi$  PDF  
431 shifted by  $m_{B_s^0} - m_{B^0}$ .

### 432 Misidentified background

433 A small fraction of  $B_s \rightarrow D_s^-\pi^+\pi^+\pi^-$  and  $B_s^0 \rightarrow D_s^*\pi^+\pi^+\pi^-$  decays, where one of the  
434 pions is misidentified as a kaon, contaminate the  $B_s^0 \rightarrow D_sK^+\pi^+\pi^-$  sample. To determine  
435 the corresponding background shapes, we use simulated events passing the nominal  
436 selection except for the PID cuts on the bachelor  $\pi^+$  tracks. The **PIDCalib** package  
437 is used to determine the  $p_T, \eta$ -dependent  $\pi^+ \rightarrow K^+$  misidentification probability for  
438 each pion. We change the particle hypothesis from pion to kaon for the pion with the  
439 higher misidentification probability and recompute the invariant  $B_s^0$  mass,  $m(D_s^-\pi_K^+\pi^+\pi^-)$ .  
440 Similarly, the invariant masses  $m(\pi_K^+\pi^+\pi^-)$  and  $m(\pi_K^+\pi^-)$  are recomputed and required  
441 to be within the considered phasespace region. The background distributions are shown  
442 in Fig. 4.2 (middle,right) and modeled by the sum of two Crystal Ball functions. The  
443 expected yield of misidentified  $B_s^0 \rightarrow D_s\pi\pi\pi$  ( $B_s^0 \rightarrow D_s^*\pi^+\pi^+\pi^-$ ) candidates in the  
444  $B_s^0 \rightarrow D_sK\pi\pi$  sample is computed by multiplying the fake rate (within the considered  
445  $B_s$  mass range) of 0.47% (0.61%) by the  $B_s^0 \rightarrow D_s\pi\pi\pi$  ( $B_s^0 \rightarrow D_s^*\pi^+\pi^+\pi^-$ ) yield as

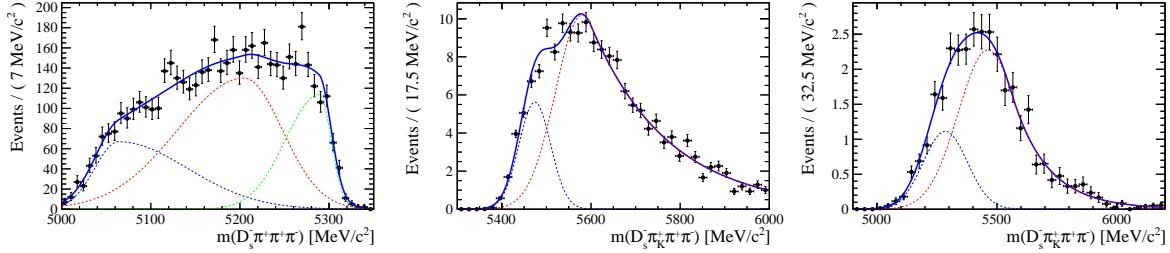


**Figure 4.2:** Left: Invariant mass distribution of simulated  $B_s^0 \rightarrow D_s^* \pi\pi\pi$  events, where the  $\gamma/\pi^0$  is excluded from the reconstruction. Middle: Invariant mass distribution of simulated  $B_s^0 \rightarrow D_s \pi\pi\pi$  events, where one of the pions is reconstructed as a kaon taking the misidentification probability into account. Right: Invariant mass distribution for simulated  $B_s^0 \rightarrow D_s^* \pi\pi\pi$  events, where the  $\gamma/\pi^0$  from the  $D_s^*$  is excluded from reconstruction and one of the pions is reconstructed as a kaon taking the misidentification probability into account. The fitted PDF is shown in blue.

determined in the mass fit to the  $B_s^0 \rightarrow D_s \pi\pi\pi$  data sample which is corrected for the  $\text{PID}(\pi^+) < 0$  requirement. The  $B_s^0 \rightarrow D_s^* \pi^+ \pi^+ \pi^-$  yield is additionally corrected for the efficiency of the cut  $m(D_s K\pi\pi) > 5200$  MeV evaluated on MC. In the fit to data, the misidentified background yields are fixed to the predicted ones.

We consider the  $B_s^0 \rightarrow D_s K\pi\pi$  and  $B_s^0 \rightarrow D_s^* K\pi\pi$  components contributing to the  $B_s^0 \rightarrow D_s \pi\pi\pi$  data sample to be negligible due to the low branching fractions and the tight PID cuts on the bachelor pions.

### 4.3 Results

Figure 4.3 shows the invariant mass distribution for  $B_s^0 \rightarrow D_s \pi\pi\pi$  and  $B_s^0 \rightarrow D_s K\pi\pi$  candidates passing all selection criteria. The projections for all categories of the simultaneous fit are shown in Appendix C together with the results for all fitted parameters. The integrated signal and background yields are listed in Tables 4.1 and 4.2.

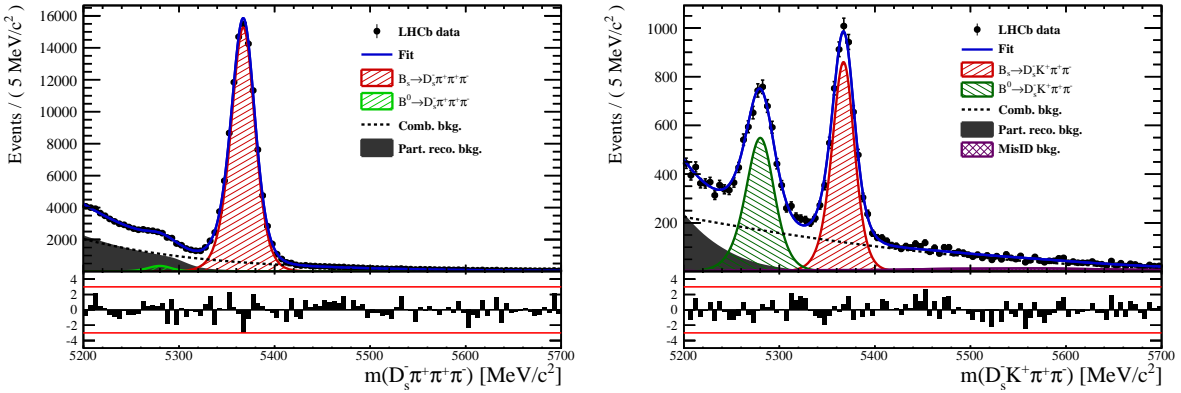


**Figure 4.3:** Invariant mass distribution of  $B_s^0 \rightarrow D_s \pi\pi\pi$  (left) and  $B_s^0 \rightarrow D_s K\pi\pi$  (right) candidates.

**Table 4.1:** Total signal and background yields for the  $B_s \rightarrow D_s\pi\pi\pi$  sample (left) and signal yield for the different  $D_s$  final states contributing to the  $B_s \rightarrow D_s\pi\pi\pi$  sample (right).

Component	Yield		
$B_s \rightarrow D_s\pi\pi\pi$	$101289 \pm 348$		
$B^0 \rightarrow D_s\pi\pi\pi$	$2318 \pm 1763$		
Partially reconstructed bkg.	$29817 \pm 530$		
Combinatorial bkg.	$52256 \pm 603$		
$D_s$ final state	Signal yield		
$D_s^- \rightarrow \phi^0(1020)\pi^-$	$34563 \pm 197$		
$D_s^- \rightarrow K^{*0}(892)K^-$	$28472 \pm 189$		
$D_s^- \rightarrow (K^-h^+\pi^-)$	$21047 \pm 160$		
$D_s^- \rightarrow \pi^+\pi^-\pi^-$	$17208 \pm 145$		

**Table 4.2:** Total signal and background yields for the  $B_s \rightarrow D_sK\pi\pi$  sample (left) and signal yield for the different  $D_s$  final states contributing to the  $B_s \rightarrow D_sK\pi\pi$  sample (right).

Component	Yield		
$B_s \rightarrow D_sK\pi\pi$	$5125 \pm 86$		
$B^0 \rightarrow D_sK\pi\pi$	$4190 \pm 92$		
Partially reconstructed bkg.	$1707 \pm 90$		
Misidentified bkg.	$683 \pm 0$		
Combinatorial bkg.	$9686 \pm 162$		
$D_s$ final state	Signal yield		
$D_s^- \rightarrow \phi^0(1020)\pi^-$	$1613 \pm 47$		
$D_s^- \rightarrow K^{*0}(892)K^-$	$1527 \pm 46$		
$D_s^- \rightarrow (K^-h^+\pi^-)$	$1128 \pm 40$		
$D_s^- \rightarrow \pi^+\pi^-\pi^-$	$857 \pm 37$		

## 462 5 Decay-time Resolution

463 The observed oscillation of B mesons is prone to dilution, if the detector resolution is  
 464 of similar magnitude as the oscillation period. In the  $B_s^0$  system, considering that the  
 465 measured oscillation frequency of the  $B_s^0$  [33] and the average LHCb detector resolution [34]  
 466 are both  $\mathcal{O}(50 \text{ fs}^{-1})$ , this is the case. Therefore, it is crucial to correctly describe the  
 467 decay time resolution in order to avoid a bias on the measurement of time dependent CP  
 468 violation. Since the time resolution depends on the particular event, especially the decay  
 469 time itself, the sensitivity on  $\gamma$  can be significantly improved by using an event dependent  
 470 resolution model rather than an average resolution. For this purpose, we use the per-event  
 471 decay time error that is estimated based on the uncertainty obtained from the global  
 472 kinematic fit of the momenta and vertex positions (DTF) with additional constraints on  
 473 the PV position and the  $D_s$  mass. In order to apply it correctly, it has to be calibrated.  
 474 The raw decay time error distributions for  $B_s^0 \rightarrow D_s\pi\pi\pi$  signal candidates are shown in  
 475 Figure 5.1 for Run-I and Run-II data. Significant deviations between the two different  
 476 data taking periods are observed due to the increase in center of mass energy from Run-I  
 477 to Run-II, as well as (among others) new tunings in the pattern and vertex reconstruction.  
 478 The decay time error calibration is consequently performed separately for both data taking  
 479 periods.

480 For Run-I data, we use the calibration from the closely related  $B_s^0 \rightarrow D_s K$  analysis  
 481 which was performed on a data sample of prompt- $D_s$  candidates combined with a random  
 482 pion track from the PV. We verify the portability to our decay channel on MC.

483 For Run-II data, a new lifetime unbiased stripping line (LTUB) has been implemented  
 484 which selects prompt- $D_s$  candidates combined with random  $K\pi\pi$  tracks from the PV.

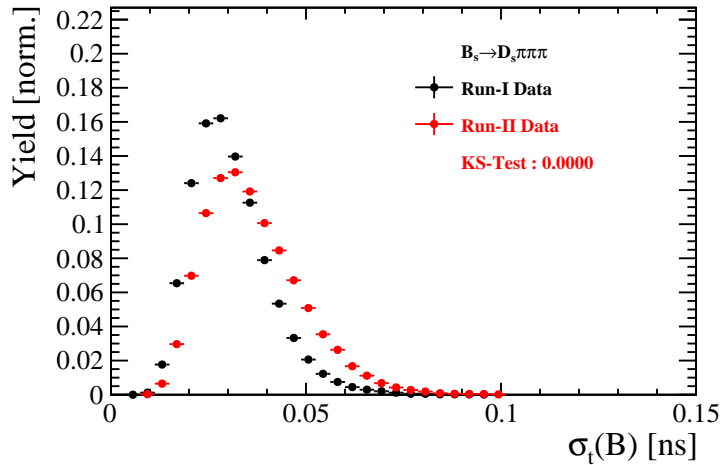


**Figure 5.1:** Distribution of the decay time error for  $B_s^0 \rightarrow D_s\pi\pi\pi$  signal candidates for Run-I (black) and Run-II (red) data (sWeighted).

## 485 5.1 Calibration for Run-I data

486 For simulated  $B_s^0 \rightarrow D_s K \pi\pi$  events, the spread of the differences between reconstructed  
 487 decay time and true decay time,  $\Delta t = t - t_{true}$ , is a direct measure of the decay time  
 488 resolution. The sum of two Gaussian pdfs with common mean but different widths is used  
 489 to fit the distribution of the decay time difference  $\Delta t$  as shown in Fig. 5.2. The effective  
 490 damping of the CP amplitudes due to the finite time resolution is described by the dilution  
 491  $\mathcal{D}$ . In the case of infinite precision, there would be no damping and therefore  $\mathcal{D} = 1$  would  
 492 hold, while for a resolution that is much larger than the  $B_s^0$  oscillation frequency,  $\mathcal{D}$  would  
 493 approach 0. For a double-Gaussian resolution model, the dilution is given by [35]

$$494 \quad \mathcal{D} = f_1 e^{-\sigma_1^2 \Delta m_s^2 / 2} + (1 - f_1) e^{-\sigma_2^2 \Delta m_s^2 / 2}, \quad (5.1)$$

494 where  $\sigma_1$  and  $\sigma_2$  are the widths of the Gaussians,  $f_1$  is the relative fraction of events  
 495 described by the first Gaussian relative to the second and  $\Delta m_s$  is the oscillation frequency  
 496 of  $B_s^0$  mesons. An effective single Gaussian width is calculated from the dilution as,

$$497 \quad \sigma_{eff} = \sqrt{(-2/\Delta m_s^2) \ln \mathcal{D}}, \quad (5.2)$$

497 which converts the resolution into a single-Gaussian function with an effective resolution  
 498 that causes the same damping effect on the magnitude of the  $B_s$  oscillation. For the Run-I  
 499  $B_s^0 \rightarrow D_s K \pi\pi$  MC sample the effective average resolution is found to be  $\sigma_{eff} = 39.1 \pm 0.3$  fs.

500 To analyze the relation between the per-event decay time error  $\delta_t$  and the actual  
 501 resolution  $\sigma_t$ , the simulated  $B_s^0 \rightarrow D_s K \pi\pi$  sample is divided into equal-statistics slices of  
 502  $\delta_t$ . For each slice, the effective resolution is determined as described above. Details of the  
 503 fit results in each slice are shown in appendix D. Figure 5.2 shows the obtained values  
 504 for  $\sigma_{eff}$  as a function of the per-event decay time error  $\sigma_t$ . To account for the variable  
 505 binning, the bin values are not placed at the bin center but at the weighted mean of the  
 506 respective per-event-error bin. A linear function is used to parametrize the distribution.  
 507 The obtained values are

$$508 \quad \sigma_{eff}^{MC}(\sigma_t) = (0.0 \pm 0.0) \text{ fs} + (1.232 \pm 0.010) \sigma_t \quad (5.3)$$

508 where the offset is fixed to 0. For comparison, the calibration function found for  $B_s^0 \rightarrow D_s K$   
 509 MC is also shown in Figure 5.2 [35]:

$$509 \quad \sigma_{eff}^{D_s K, MC}(\sigma_t) = (0.0 \pm 0.0) \text{ fs} + (1.201 \pm 0.013) \sigma_t. \quad (5.4)$$

510 Due to the good agreement between the scale factors for  $B_s^0 \rightarrow D_s K$  and  $B_s^0 \rightarrow D_s K \pi\pi$   
 511 MC, we conclude that the resolution calibration for  $B_s^0 \rightarrow D_s K$  data:

$$512 \quad \sigma_{eff}^{D_s K}(\sigma_t) = (10.26 \pm 1.52) \text{ fs} + (1.280 \pm 0.042) \sigma_t \quad (5.5)$$

512 can be used for our analysis. The following calibration functions were used in the  
 513  $B_s^0 \rightarrow D_s K$  analysis to estimate the systematic uncertainty on the decay-time resolution:

$$514 \quad \sigma_{eff}^{D_s K}(\sigma_t) = (-0.568 \pm 1.570) \text{ fs} + (1.243 \pm 0.044) \sigma_t \quad (5.6)$$

$$514 \quad \sigma_{eff}^{D_s K}(\sigma_t) = (0.0 \pm 0.0) \text{ fs} + (1.772 \pm 0.012) \sigma_t \quad (5.7)$$

515 The difference of the scale factors observed on  $B_s^0 \rightarrow D_s K$  and  $B_s^0 \rightarrow D_s K \pi\pi$  MC is  
 516 assigned as additional systematic uncertainty.

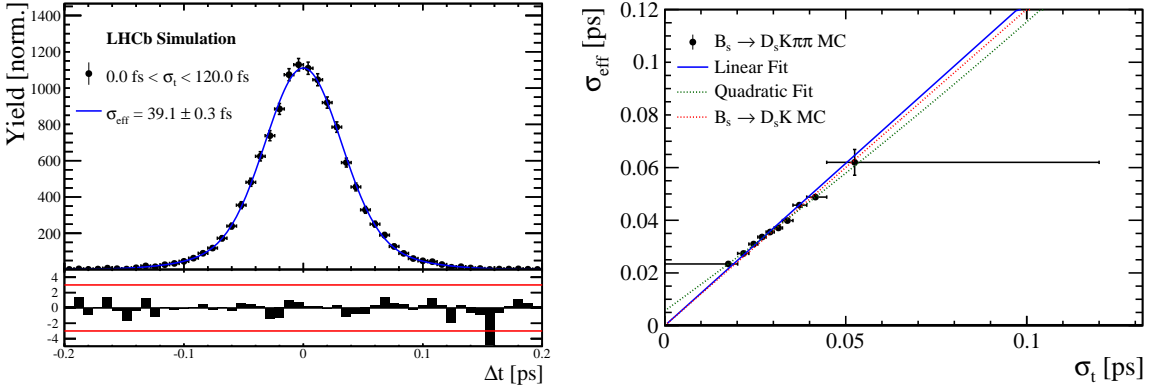


**Figure 5.2:** (Left) Difference of the true and measured decay time of  $B_s^0 \rightarrow D_s K\pi\pi$  MC candidates. (Right) The measured resolution  $\sigma_{eff}$  as function of the per-event decay time error estimate  $\sigma_t$  for  $B_s \rightarrow D_s K\pi\pi$  MC (Run-I). The fitted calibration curve is shown in blue.

## 517 5.2 Calibration for Run-II data

518 For the resolution calibration of Run-II data, a sample of promptly produced  $D_s$  candidates  
 519 is selected using the B02DsKPiPiLTUBD2HHHBeauty2CharmLine stripping line. This  
 520 lifetime-unbiased stripping line does not apply selection requirements related to lifetime  
 521 or impact parameter, allowing for a study of the resolution. In order to reduce the rate  
 522 of this sample it is pre-scaled in the stripping. Each  $D_s$  candidate is combined with a  
 523 random kaon track and two random pion tracks which originate from the PV to obtain a  
 524 sample of fake  $B_s$  candidates with a known true decay-time of  $t_{true} = 0$ . The difference of  
 525 the measured decay time,  $t$ , of these candidates with respect to the true decay time is  
 526 attributed to the decay time resolution.

527 The offline selection of the fake  $B_s$  candidates is summarized in Tab. 5.1. The selection  
 528 is similar than the one for real data with the important difference that the  $D_s$  candidate  
 529 is required to come from the PV by cutting on the impact parameter significance. Even  
 530 after the full selection, a significant number of multiple candidates is observed. These  
 531 are predominantly fake  $B_s$  candidates that share the same  $D_s$  candidate combined with  
 532 different random tracks from the PV. We select one of these multiple candidates randomly  
 533 which retains approximately 20% of the total candidates. The invariant mass distribution  
 534 of the selected  $D_s$  candidates is shown in Fig. 5.3. To separate true  $D_s$  candidates from  
 535 random combinations, the sPlot method is used to statistically subtract combinatorial  
 536 background from the sample.

537 Figure 5.4 shows the sWeighted decay-time distribution for fake  $B_s$  candidates. Similar  
 538 as in the previous section, the decay-time distribution is fitted with a double-Gaussian  
 539 resolution model in slices of the per-event decay time error. Since some  $D_s$  candidates  
 540 might actually originate from true  $B_s$  decays, the decay-time distribution of the fake  $B_s$   
 541 candidates might show a bias towards positive decay times. Therefore, we determine the  
 542 decay-time resolution from the negative decay-time distribution only. Details of the fit  
 543 results in each slice are shown in appendix D. The resulting calibration function:

$$\sigma_{eff}^{Data}(\sigma_t) = (9.7 \pm 1.7) \text{ fs} + (0.915 \pm 0.040) \sigma_t \quad (5.8)$$

<sup>544</sup> is in good agreement with the one obtained for the  $B_s \rightarrow J/\psi\phi$  (Run-II) analysis [36].

$$\sigma_{eff}^{J/\psi\phi}(\sigma_t) = (12.25 \pm 0.33) \text{ fs} + (0.8721 \pm 0.0080) \sigma_t \quad (5.9)$$

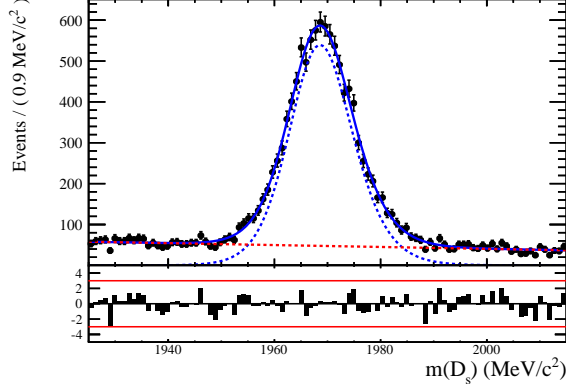


**Figure 5.3:** The invariant mass distribution for prompt  $D_s$  candidates.

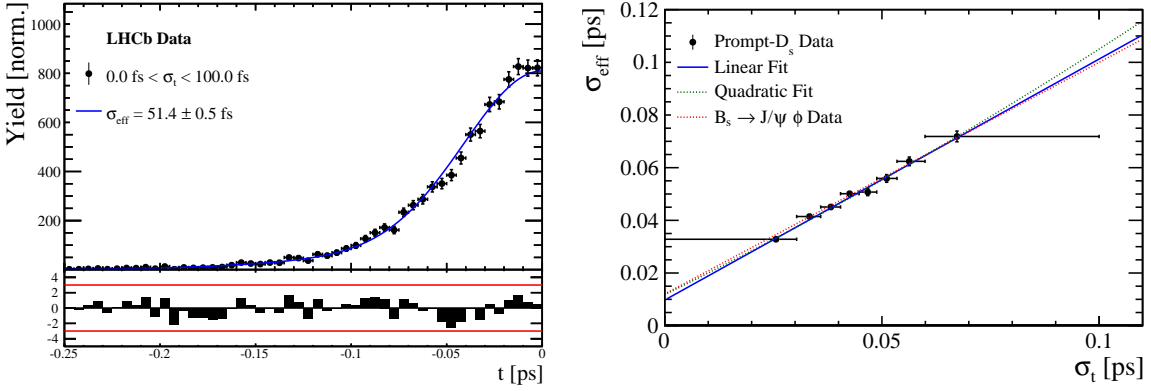


**Figure 5.4:** (Left) Decay-time distribution for fake  $B_s$  candidates from promptly produced  $D_s$  candidates, combined with random prompt  $K\pi\pi$  bachelor tracks. (Right) The measured resolution  $\sigma_{eff}$  as function of the per-event decay time error estimate  $\sigma_t$  for fake  $B_s$  candidates (Run-II data). The fitted calibration curve is shown in blue.

**Table 5.1:** Offline selection requirements for fake  $B_s$  candidates from promptly produced  $D_s$  candidates combined with random prompt  $K\pi\pi$  bachelor tracks.

	Description	Requirement
$B_s \rightarrow D_s K\pi\pi$	$\chi^2_{vtx}/\text{ndof}$	< 8
	$\chi^2_{DTF}/\text{ndof}$	< 15
	$t$	< 0 ps
$D_s \rightarrow hhh$	$\chi^2_{vtx}/\text{ndof}$	< 5
	DIRA	> 0.99994
	$\chi^2_{FD}$	> 9
	$p_T$	> 1800 MeV
	$\chi^2_{IP}$	< 9
	$\chi^2_{IP}(h)$	> 5
	Wrong PV veto	$nPV = 1 \parallel \min(\Delta\chi^2_{IP}) > 20$
$D_s^- \rightarrow KK\pi^-$	$D^0$ veto	$m(KK) < 1840$ MeV
	$D^-$ veto	$m(K^+K_\pi^-\pi^-) \neq m(D^-) \pm 30$ MeV
	$\Lambda_c$ veto	$m(K^+K_p^-\pi^-) \neq m(\Lambda_c) \pm 30$ MeV
$D_s^- \rightarrow \phi\pi^-$	$m(KK)$	$= m_\phi \pm 20$ MeV
	PIDK( $K^+$ )	> -10
	PIDK( $K^-$ )	> -10
	PIDK( $\pi^-$ )	< 20
$D_s^- \rightarrow K^*(892)K^-$	$m(KK)$	$\neq m_\phi \pm 20$ MeV
	$m(K^+\pi^-)$	$= m_{K^*(892)} \pm 75$ MeV
	PIDK( $K^+$ )	> -10
	PIDK( $K^-$ )	> -5
	PIDK( $\pi^-$ )	< 20
$D_s^- \rightarrow (KK\pi^-)_{NR}$	$m(KK)$	$\neq m_\phi \pm 20$ MeV
	$m(K^+\pi^-)$	$\neq m_{K^*(892)} \pm 75$ MeV
	PIDK( $K^+$ )	> 5
	PIDK( $K^-$ )	> 5
	PIDK( $\pi^-$ )	< 10
$D_s \rightarrow \pi\pi\pi$	PIDK( $h$ )	< 10
	PIDp( $h$ )	< 10
	$D^0$ veto	$m(\pi^+\pi^-) < 1700$ MeV
$X_s \rightarrow K\pi\pi$	$\chi^2_{IP}(h)$	< 40
	PIDK( $K$ )	> 10
	PIDK( $\pi$ )	< 5
	isMuon( $h$ )	False
All tracks	$p_T$	> 500 MeV

## 545 6 Acceptance

### 546 6.1 MC corrections

#### 547 6.1.1 Truth matching of simulated candidates

548 We use the `BackgroundCategory` tool to truth match our simulated candidates. Candidates  
 549 with background category (`BKGCAT`) 20 or 50 are considered to be true signal. Background  
 550 category 60 is more peculiar since it contains both badly reconstructed signal candidates  
 551 and ghost background. This is due to the fact that the classification algorithms identifies  
 552 all tracks for which less than 70% of the reconstructed hits are matched to generated  
 553 truth-level quantities as ghosts. In particular for signal decays involving many tracks (as  
 554 in our case), this arbitrary cutoff is not 100% efficient. Moreover, the efficiency is expected  
 555 to depend on the kinematics which would lead to a biased acceptance determination if  
 556 candidates with `BKGCAT`= 60 would be removed. We therefore include `BKGCAT`= 60 and  
 557 statistically subtract the ghost background by using the `sPlot` technique. The `sWeights`  
 558 are calculated from a fit to the reconstructed  $B_s$  mass. The signal contribution is modeled  
 559 as described in Sec. 4.1 and the background with a polynomial. The fit is performed  
 560 simultaneously in two categories; the first includes events with `BKGCAT` = 20 or 50 and  
 561 the second events with `BKGCAT` = 60. To account for the different mass resolution we  
 562 use a different  $\sigma$  for each category, while the mean and the tail parameters are shared  
 563 between them. The background component is only included for the second category.

564 A significant fraction of 8% of the true signal candidates are classified as ghosts, while  
 565 only 20% of the events classified with `BKGCAT`= 60 are indeed genuine ghosts.

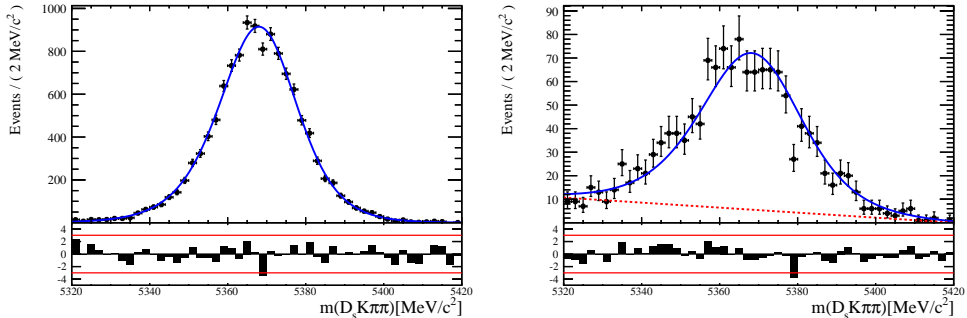


**Figure 6.1:** The reconstructed  $B_s$  mass distribution for simulated  $B_s \rightarrow D_s K\pi\pi$  decays classified with `BKGCAT` = 20 or 50 (left) and `BKGCAT` = 60 (right) after the full selection.

#### 566 6.1.2 Correction of data-simulation differences

567 For the evaluation of phase space efficiency and to a lesser extend also the decay-time  
 568 efficiency we rely on simulated data as discussed in the following sections. A number  
 569 of data-driven corrections are applied to the MC samples to account for known data-  
 570 simulation differences. The MC sample is reweighted to match the two-dimensional  $p_T$  and  
 571  $\eta$  distribution observed on real data. An additional reweighting of the track multiplicity  
 572 is applied on top of that. The distributions before and after reweighting are shown in  
 573 Appendix H. We use the `PIDCorr` tool to correct the simulated PID responses based on  
 574 PID calibration samples [37].

575 **6.2 Decay-time acceptance**

576 The decay-time distribution of the  $B_s^0$  mesons is sculpted due to the geometry of the LHCb  
 577 detector and the applied selection cuts, which are described in Section 3. In particular, any  
 578 requirement on the flight distance, the impact parameter or the direction angle (DIRA)  
 579 of the  $B_s^0$  mesons, as well as the direct cut on the proper-time, will lead to a decay-time  
 580 dependent efficiency  $\epsilon(t)$ .

581 We use a combination of control channels to derive the acceptance function  $\epsilon(t)$ ,  
 582 because for  $B_s^0 \rightarrow D_s K\pi\pi$  decays the decay-time acceptance is strongly correlated with  
 583 the  $CP$ -observables which we aim to measure. Therefore, extracting the  $CP$ -observables  
 584 and the acceptance shape at the same time is not possible. A fit to the decay-time  
 585 distribution of  $B_s^0 \rightarrow D_s \pi\pi\pi$  candidates is performed and the obtained acceptance shape  
 586 is corrected for the small difference observed between the  $B_s^0 \rightarrow D_s K\pi\pi$  and  $B_s^0 \rightarrow D_s \pi\pi\pi$   
 587 MC samples. In addition, we include the control channel  $B^0 \rightarrow D_s K\pi\pi$  to increase  
 588 the statistical precision. A simultaneous fit to the four datasets ( $B_s^0 \rightarrow D_s \pi\pi\pi$  data,  
 589  $B^0 \rightarrow D_s K\pi\pi$  data,  $B_s^0 \rightarrow D_s K\pi\pi$  MC and  $B_s^0 \rightarrow D_s \pi\pi\pi$  MC) is performed to allow for  
 590 a straightforward propagation of uncertainties. In each case, a PDF of the following form

$$\mathcal{P}(t, \delta t) = \left[ e^{-\Gamma t} \cdot \cosh\left(\frac{\Delta\Gamma t'}{2}\right) \otimes \mathcal{R}(t - t', \delta t) \right] \cdot \epsilon(t), \quad (6.1)$$

591 is used to describe the decay-time distribution. For real data, the values for  $\Gamma_{s,d}$  and  
 592  $\Delta\Gamma_{s,d}$  are fixed to the latest HFAG results [38], while for simulated data, the generated  
 593 values are used. A single Gaussian resolution function  $\mathcal{R}(t - t', \delta t)$  is used where the  
 594 decay-time error estimate is scaled with the respective calibration functions determined in  
 595 Sec. 5. Each decay-time acceptance  $\epsilon(t)$  is modeled using cubic splines, allowing for the  
 596 analytical computation of the decay-time integrals appearing in the PDF [39]. The splines  
 597 are parametrized by so-called knots  $(t_0, t_1, \dots, t_N)$  which determine their boundaries. Two  
 598 knots are located by default at the lower and upper edge of the interval allowed for the  
 599 decay time, the remaining ones are chosen such that there is an approximately equal  
 600 amount of data in-between two consecutive knots. In the basis of cubic b-splines,  $b_i(t)$ ,  
 601 the acceptance is then constructed as:

$$\epsilon(t) = \sum_{i=0}^N v_i b_i(t) \quad (6.2)$$

602 where the spline coefficients  $v_i$  are determined from the fit. We fix coefficient  $v_{N-1}$  to unity  
 603 in order to normalize the overall acceptance function. To stabilize the upper decay-time  
 604 acceptance,  $v_N$  is fixed by a linear extrapolation from the two previous coefficients:

$$v_N = v_{N-1} + \frac{v_{N-2} - v_{N-1}}{t_{N-2} - t_{N-1}} \cdot (t_N - t_{N-1}). \quad (6.3)$$

605 It was found that at least  $N = 6$  knots are necessary for a sufficient fit quality.

606 Three distinct splines are used in the following combinations to describe the acceptances  
607 for the four datasets:

- 608 •  $B_s^0 \rightarrow D_s K\pi\pi$  MC:  $\epsilon_{D_s K\pi\pi}^{MC}(t)$   
609 •  $B_s^0 \rightarrow D_s \pi\pi\pi$  MC:  $\epsilon_{D_s \pi\pi\pi}^{MC}(t) = R(t) \cdot \epsilon_{D_s K\pi\pi}^{MC}(t)$   
610 •  $B_s^0 \rightarrow D_s \pi\pi\pi$  data:  $\epsilon_{D_s \pi\pi\pi}^{Data}(t) = R(t) \cdot \epsilon_{D_s K\pi\pi}^{Data}(t)$   
611 •  $B^0 \rightarrow D_s K\pi\pi$  data:  $\epsilon_{D_s K\pi\pi}^{Data}(t)$

612 where  $\epsilon_{D_s K\pi\pi}^{MC}(t)$  represents the acceptance in  $B_s^0 \rightarrow D_s K\pi\pi$  MC,  $R(t)$  represents the  
613 ratio of acceptances in  $B_s^0 \rightarrow D_s \pi\pi\pi$  and  $B_s^0 \rightarrow D_s K\pi\pi$  MC and the final acceptance in  
614  $B_s^0 \rightarrow D_s K\pi\pi$  data is represented by  $\epsilon_{D_s K\pi\pi}^{Data}(t)$ .

615 The acceptances are determined separately for each data-taking period and each  
616 trigger category as discussed in more detail in Appendix E. The fit results are shown in  
617 Figs. 6.2 to 6.5 and the fitted parameters are summarized in Tables 6.1 to 6.4.

618

619

620 As currently there are no Run-II MC samples available, we use the Run-I MC  
samples also for the Run-II fits. An alternative approach would be to fit only the  
 $B^0 \rightarrow D_s K\pi\pi$  data sample in order to remove the MC dependency. The final strat-  
egy will be fixed, depending on the MC availability, during the review.

**Table 6.1:** Time acceptance parameters for events in category [Run-I,L0-TOS].

Knot position	Coefficient	$B_s^0 \rightarrow D_s K\pi\pi$ data	$B_s^0 \rightarrow D_s K\pi\pi$ MC	Ratio
0.4	$v_0$	$0.592 \pm 0.038$	$0.542 \pm 0.021$	$0.972 \pm 0.056$
0.8	$v_1$	$0.805 \pm 0.057$	$0.781 \pm 0.033$	$0.915 \pm 0.064$
1.6	$v_2$	$0.852 \pm 0.077$	$0.917 \pm 0.051$	$1.034 \pm 0.080$
2.5	$v_3$	$1.117 \pm 0.042$	$1.108 \pm 0.029$	$0.955 \pm 0.045$
6.5	$v_4$	1.0 (fixed)	1.0 (fixed)	1.0 (fixed)
10.0	$v_5$	0.898 (interpolated)	0.906 (interpolated)	1.039 (interpolated)

**Table 6.2:** Time acceptance parameters for events in category [Run-I,L0-TIS].

Knot position	Coefficient	$B_s^0 \rightarrow D_s K\pi\pi$ data	$B_s^0 \rightarrow D_s K\pi\pi$ MC	Ratio
0.4	$v_0$	$0.417 \pm 0.038$	$0.415 \pm 0.021$	$0.948 \pm 0.077$
0.8	$v_1$	$0.623 \pm 0.060$	$0.654 \pm 0.035$	$0.873 \pm 0.080$
1.6	$v_2$	$0.901 \pm 0.097$	$0.976 \pm 0.061$	$0.909 \pm 0.087$
2.5	$v_3$	$1.095 \pm 0.052$	$1.076 \pm 0.035$	$1.003 \pm 0.051$
6.5	$v_4$	1.0 (fixed)	1.0 (fixed)	1.0 (fixed)
10.0	$v_5$	0.917 (interpolated)	0.933 (interpolated)	0.998 (interpolated)

**Table 6.3:** Time acceptance parameters for events in category [Run-II,L0-TOS].

Knot position	Coefficient	$B_s^0 \rightarrow D_s K\pi\pi$ data	$B_s^0 \rightarrow D_s K\pi\pi$ MC	Ratio
0.4	$v_0$	$0.568 \pm 0.028$	$0.496 \pm 0.015$	$0.965 \pm 0.044$
0.8	$v_1$	$0.787 \pm 0.043$	$0.738 \pm 0.024$	$0.892 \pm 0.049$
1.6	$v_2$	$0.899 \pm 0.061$	$0.943 \pm 0.039$	$0.984 \pm 0.059$
2.5	$v_3$	$1.079 \pm 0.030$	$1.093 \pm 0.021$	$0.979 \pm 0.030$
6.5	$v_4$	1.0 (fixed)	1.0 (fixed)	1.0 (fixed)
10.0	$v_5$	0.931 (interpolated)	0.919 (interpolated)	1.018 (interpolated)

**Table 6.4:** Time acceptance parameters for events in category [Run-II,L0-TIS].

Knot position	Coefficient	$B_s^0 \rightarrow D_s K\pi\pi$ data	$B_s^0 \rightarrow D_s K\pi\pi$ MC	Ratio
0.4	$v_0$	$0.389 \pm 0.009$	$0.506 \pm 0.015$	$0.908 \pm 0.031$
0.8	$v_1$	$0.592 \pm 0.013$	$0.744 \pm 0.024$	$0.896 \pm 0.035$
1.6	$v_2$	$0.798 \pm 0.052$	$0.965 \pm 0.041$	$0.927 \pm 0.054$
2.5	$v_3$	$1.111 \pm 0.035$	$1.112 \pm 0.023$	$0.941 \pm 0.039$
6.5	$v_4$	1.0 (fixed)	1.0 (fixed)	1.0 (fixed)
10.0	$v_5$	0.903 (interpolated)	0.902 (interpolated)	1.052 (interpolated)

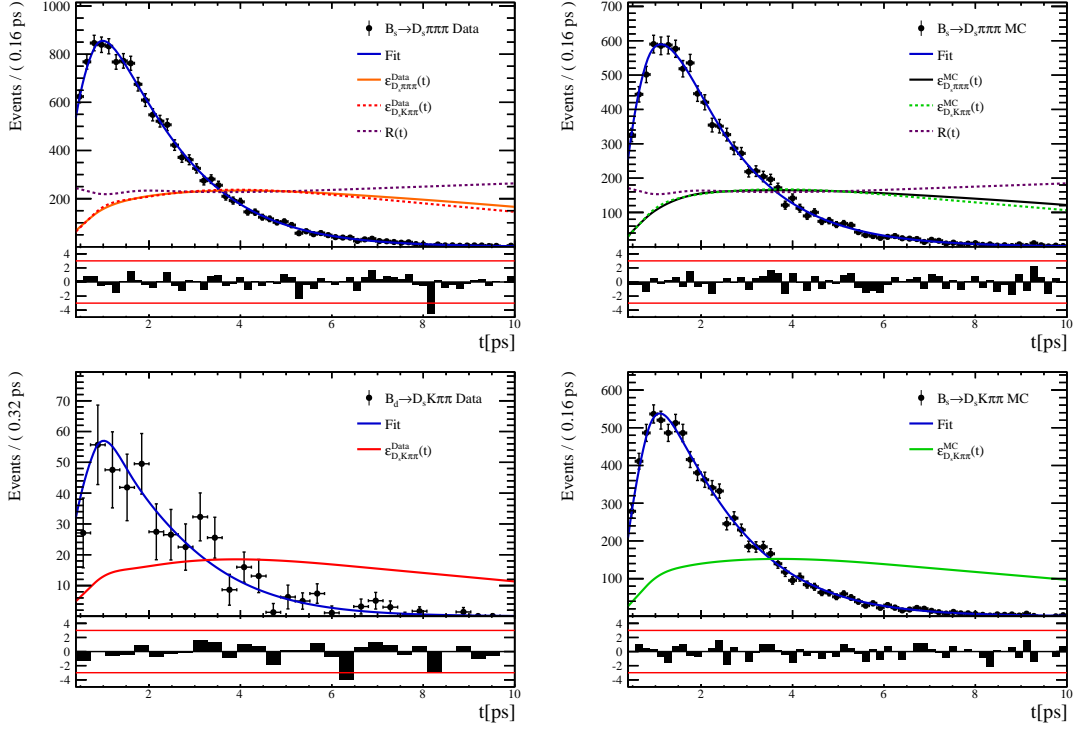


**Figure 6.2:** Decay-time fit projections for  $B_s^0 \rightarrow D_s\pi\pi\pi$  data (top-left),  $B_s^0 \rightarrow D_s\pi\pi\pi$  MC (top-right),  $B_s^0 \rightarrow D_sK\pi\pi$  data (bottom-left) and  $B_s^0 \rightarrow D_sK\pi\pi$  MC (bottom-right) in category [Run-I,L0-TOS]. The respective acceptance function is overlaid in an arbitrary scale.

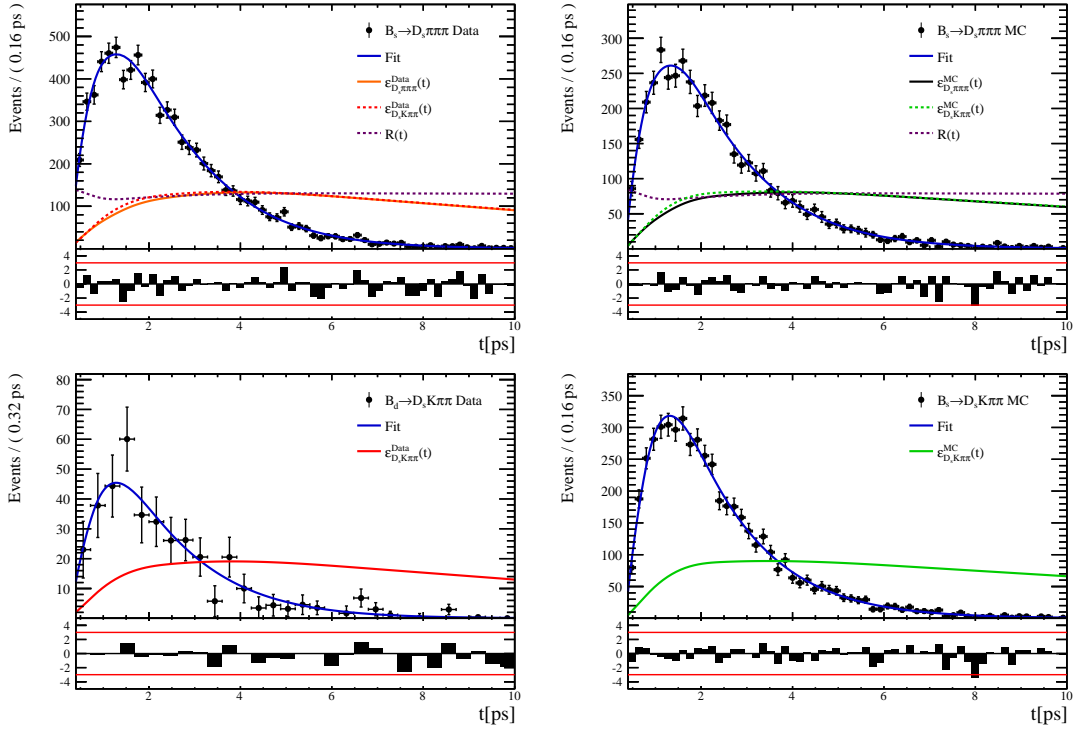


**Figure 6.3:** Decay-time fit projections for  $B_s^0 \rightarrow D_s\pi\pi\pi$  data (top-left),  $B_s^0 \rightarrow D_s\pi\pi\pi$  MC (top-right),  $B_s^0 \rightarrow D_sK\pi\pi$  data (bottom-left) and  $B_s^0 \rightarrow D_sK\pi\pi$  MC (bottom-right) in category [Run-I,L0-TIS]. The respective acceptance function is overlaid in an arbitrary scale.

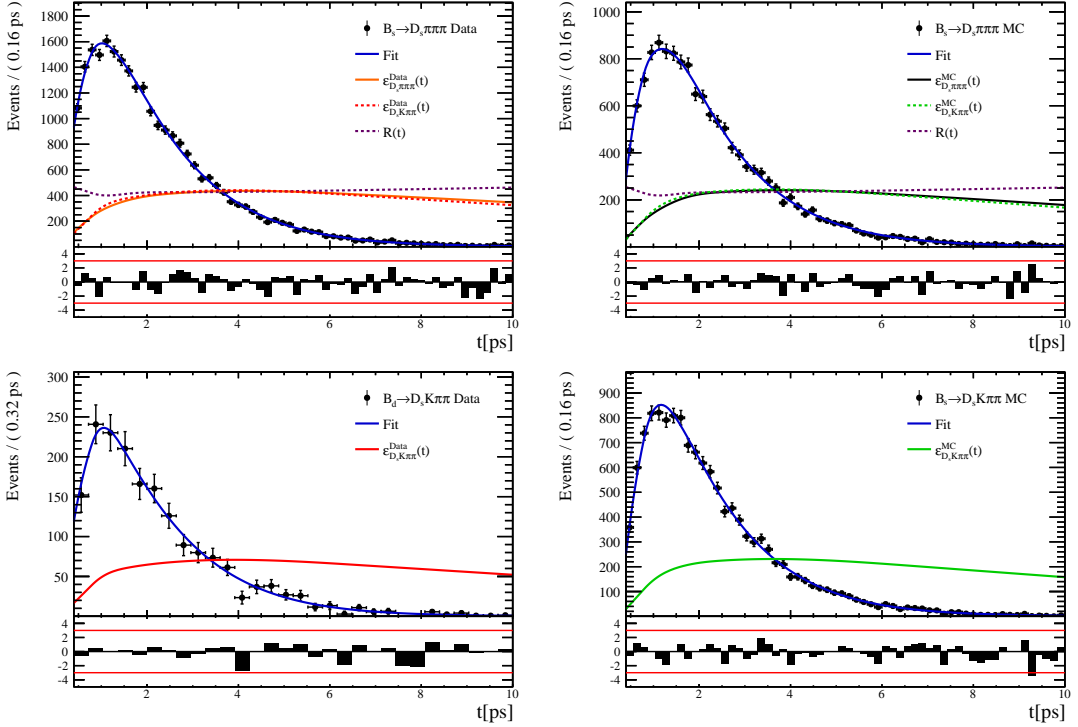


**Figure 6.4:** Decay-time fit projections for  $B_s^0 \rightarrow D_s \pi\pi\pi$  data (top-left),  $B_s^0 \rightarrow D_s \pi\pi\pi$  MC (top-right),  $B^0 \rightarrow D_s K\pi\pi$  data (bottom-left) and  $B_s^0 \rightarrow D_s K\pi\pi$  MC (bottom-right) in category [Run-II,L0-TOS]. The respective acceptance function is overlaid in an arbitrary scale.

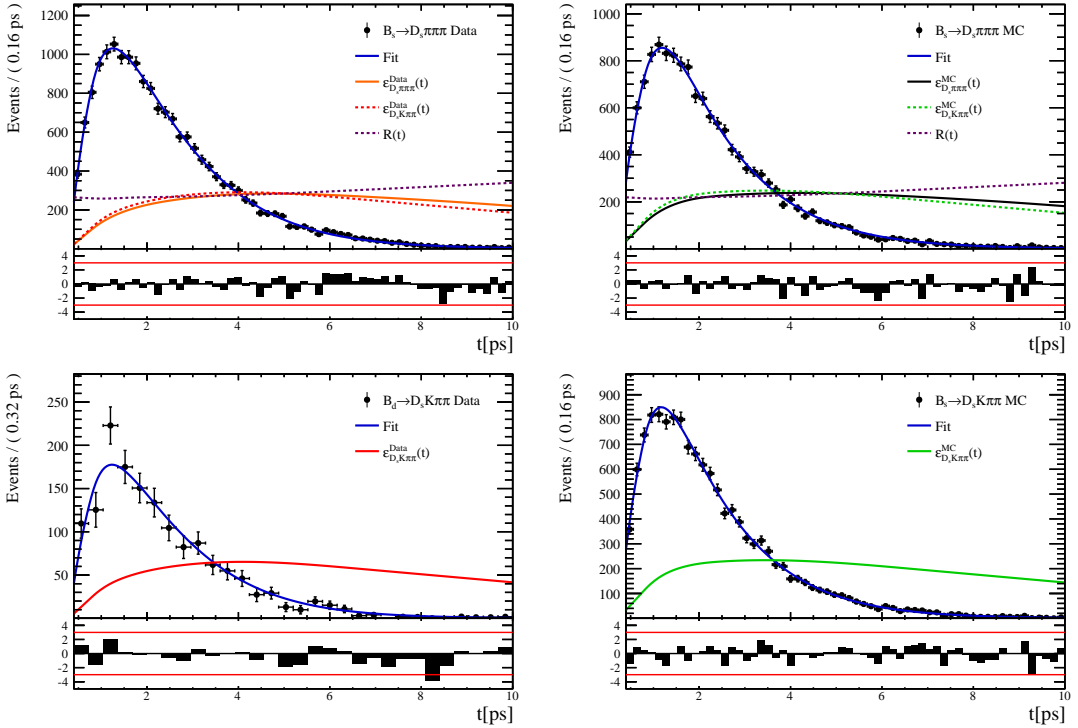


**Figure 6.5:** Decay-time fit projections for  $B_s^0 \rightarrow D_s \pi\pi\pi$  data (top-left),  $B_s^0 \rightarrow D_s \pi\pi\pi$  MC (top-right),  $B^0 \rightarrow D_s K\pi\pi$  data (bottom-left) and  $B_s^0 \rightarrow D_s K\pi\pi$  MC (bottom-right) in category [Run-II,L0-TIS]. The respective acceptance function is overlaid in an arbitrary scale.

### 621 6.3 Phase space acceptance

622 The signal PDF used for the full time-dependent amplitude fit can be written in terms of  
 623 the differential decay rate from Equation 2.29 as

$$\mathcal{P}(\mathbf{x}, t, g, f) = \frac{\left( \frac{d\Gamma(\mathbf{x}, t, q, f)}{dt d\Phi_4} \right) \cdot \epsilon(\mathbf{x}) \cdot \epsilon(t)}{\int \sum_{q,f} \left( \frac{d\Gamma(\mathbf{x}, t, q, f)}{dt d\Phi_4} \right) \cdot \epsilon(\mathbf{x}) \cdot \epsilon(t) dt d\Phi_4} \quad (6.4)$$

624 where  $\epsilon(\mathbf{x})$  is the phase-space efficiency. Note that the efficiency in the numerator appears  
 625 as an additive constant in the log  $\mathcal{L}$  that does not depend on any fit parameters such that it  
 626 can be ignored. However, the efficiency function still enters via the normalization integrals.  
 627 In contrast to the time integrals which can be performed analytically as discussed in  
 628 Sec. 6.2, the phase-space integrals are determined numerically. For this purpose, we use  
 629 simulated events generated with **EVTGEN**, pass them through the full detector simulation  
 630 and apply the same selection criteria as for data in order to perform the MC integrals. As  
 631 an example, the integral of the total  $b \rightarrow c$  amplitude squared can be approximated as

$$\int |\mathcal{A}_f^c(\mathbf{x})|^2 \epsilon(\mathbf{x}) d\Phi_4 \approx \frac{1}{N_{MC}} \sum_k^{N_{MC}} \frac{|\mathcal{A}_f^c(\mathbf{x}_k)|^2}{|A'(\mathbf{x}_k)|^2} \quad (6.5)$$

632 where  $A'$  labels the amplitude model used for the generation and  $x_k$  is the  $k$ -th MC  
 633 event. As a result, the phase-space efficiency can be included in the fit without explicitly  
 634 modeling it.

635

636

Disclaimer: At the moment there is only a small Run-I MC sample available where a DecFile (EventType: 13266007) was used from which we were not able to reproduce the generator pdf  $A'$ . We can therefore not follow our preferred procedure described above. An alternative, provisionally method is briefly described in the following.

637

638 We use a BDTG to map the five-dimensional phase space to an one-dimensional distribution  
 639 [40]. The BDTG is trained to learn the differences between the selected MC and a generator  
 640 level MC sample. As discriminating variables, five invariant mass combinations are used  
 641 as shown in Fig. 6.6. Based on the classifier output distributions, shown in Fig. 6.7, an  
 642 efficiency as function of the BDTG response is derived.

643 A large toy MC sample is generated (500 k events) according to a preliminary amplitude  
 644 model  $A'(\mathbf{x})$  and for each event a weight, depending on the BDTG response, is assigned to  
 645 account for the efficiency variation across phase space. This reweighted toy MC sample is  
 646 then effectively distributed as  $A'(\mathbf{x}) \cdot \epsilon(\mathbf{x})$  and can be used to calculate the normalization  
 647 integrals in Equation 6.5. Figure 6.8 compares the phase space efficiency obtained from  
 648 the reweighted toy MC sample with the 'true' efficiency given by the ratio of selected and  
 649 generated MC events. A fairly good agreement is observed in all dimensions.

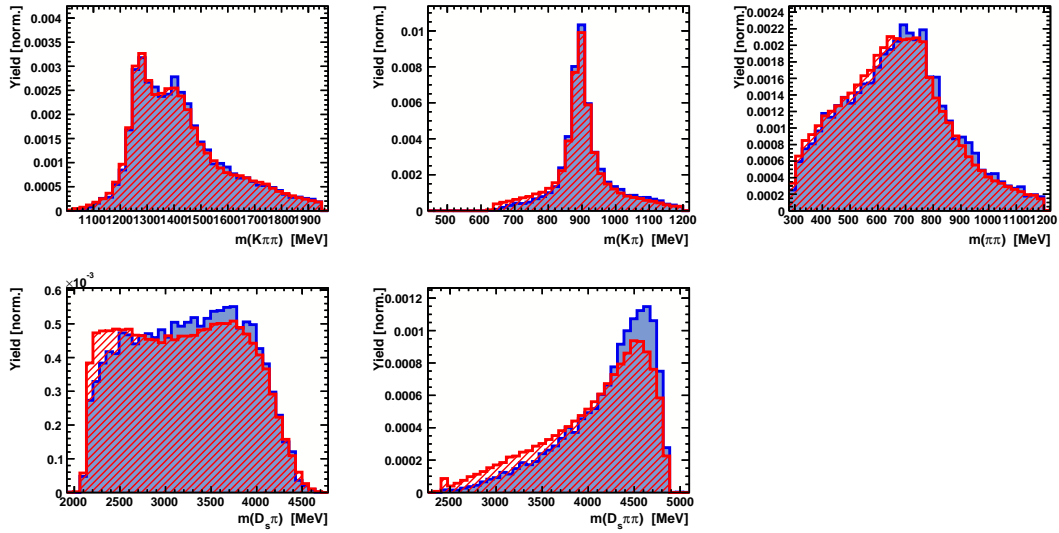


**Figure 6.6:** Discriminating variables used to train the BDTG. The selected MC sample is shown in blue and the generator MC sample in red.

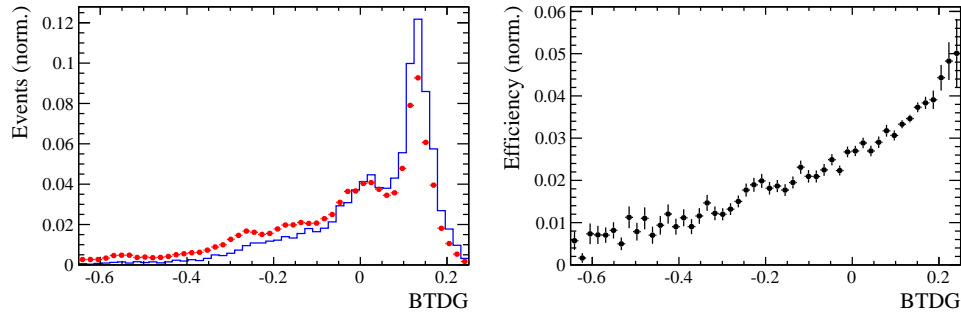


**Figure 6.7:** Left: Output distributions of the BDTG for the simulated MC sample (blue) and the generator level sample (red). Right: Phase space efficiency as function of the BDTG response computed as the ratio of selected and generated decays.

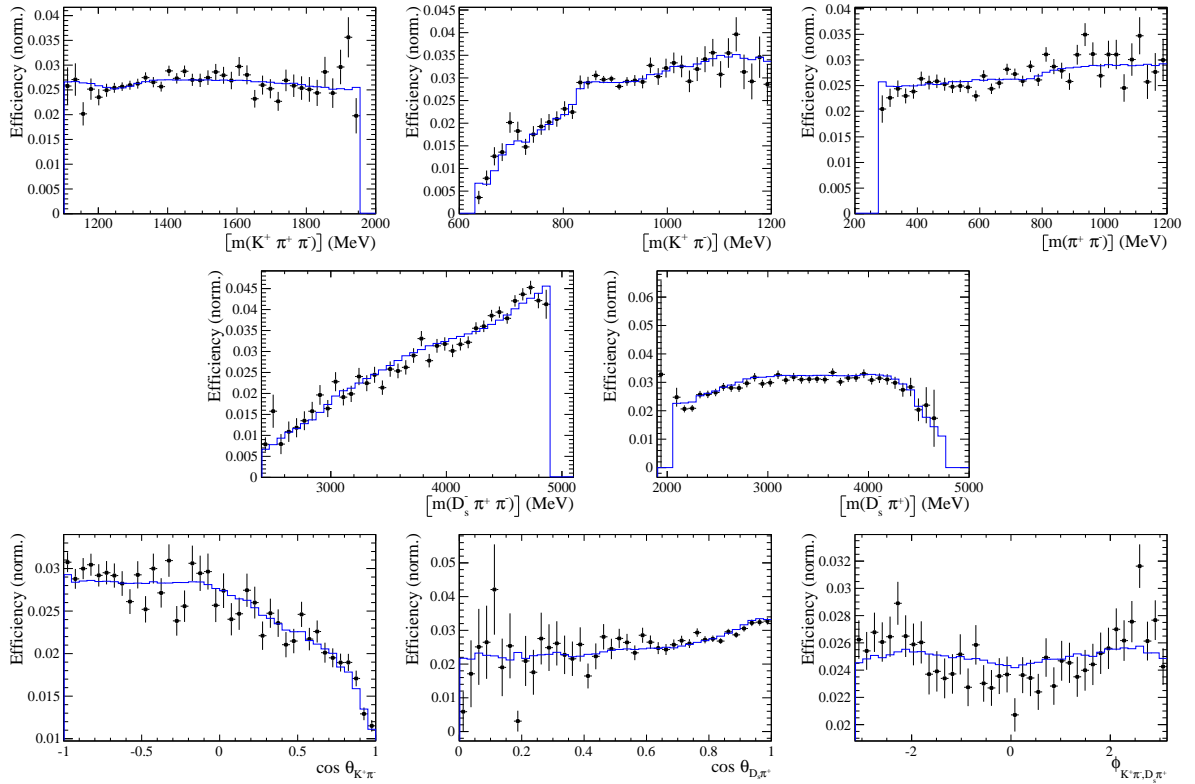


**Figure 6.8:** Efficiency variation as a function of the phase-space variables obtained from the ratio of selected and generated MC events (data points) and efficiency obtained from a reweighted toy MC sample (blue).

## 650 7 Flavour Tagging

651 To identify the initial flavour state of the  $B_s^0$  meson, a number of flavour tagging algorithms  
 652 are used that either determine the flavour of the non-signal b-hadron produced in the  
 653 event (opposite site, OS [41]) or use particles produced in the fragmentation of the signal  
 654 candidate  $B_s^0/\bar{B}_s^0$  (same side, SS [42]). For the same side, the algorithm searching for the  
 655 charge of an additional kaon that accompanies the fragmentation of the signal candidate  
 656 is used (SS-Kaon). For the opposite site, four different taggers are chosen: The algorithms  
 657 that use the charge of an electron or a muon from semi-leptonic B decays (OS- $e,\mu$ ), the  
 658 tagger that uses the charge of a kaon from a  $b \rightarrow c \rightarrow s$  decay chain (OS-nnetKaon) and  
 659 the algorithm that determines the  $B_s^0/\bar{B}_s^0$  candidate flavour from the charge of a secondary  
 660 vertex, reconstructed from the OS b decay product (OS-VtxCharge).

661 Every tagging algorithm is prone to misidentify the signal candidate at a certain  
 662 mistag rate  $\omega$ . This might be caused by particle misidentification, flavour oscillation  
 663 of the neutral opposite site B-meson or by tracks that are wrongly picked up from the  
 664 underlying event. An imperfect determination of the  $B_s^0$  production flavor dilutes the  
 665 observed  $CP$  asymmetry by a factor  $D_{tag} = 1 - 2\omega$ . This means that the statistical  
 666 precision, with which the  $CP$  asymmetry can be measured, scales as the inverse square  
 667 root of the effective tagging efficiency:

$$\epsilon_{eff} = \epsilon_{tag}(1 - 2\omega)^2, \quad (7.1)$$

668 where  $\epsilon_{tag}$  is the fraction of tagged candidates.

669 For each  $B_s^0/\bar{B}_s^0$  candidate, the tagging algorithms provide, besides a flavour tag  
 670  $q = 1, -1, 0$  (for an initial  $B_s^0$ ,  $\bar{B}_s^0$  or no tag), a prediction for the mistag probability  $\eta$   
 671 based on the output of multivariate classifiers. These are trained on simulated samples  
 672 of flavour specific control channels ( $B_s^0 \rightarrow D_s^- \pi^+$  (SS algorithm) and  $B^+ \rightarrow J/\psi K^+$  (OS  
 673 algorithms)) and are optimized for highest  $\epsilon_{eff}$  on data. Utilizing flavour-specific final  
 674 states, the estimated mistag  $\eta$  of each tagger has to be calibrated to match the actual  
 675 mistag probability  $\omega$ . For the calibration, a linear model

$$\omega(\eta) = p_0 + p_1 \cdot (\eta - \langle \eta \rangle), \quad (7.2)$$

676 is used where  $\langle \eta \rangle$  is the average estimated mistag probability. A perfectly calibrated  
 677 tagger would lead to  $\omega(\eta) = \eta$  and one would expect  $p_1 = 1$  and  $p_0 = \langle \eta \rangle$ . Due to the  
 678 different interaction cross-sections of oppositely charged particles, the tagging calibration  
 679 parameters depend on the initial state flavour of the  $B_s^0$ . Therefore, the flavour asymmetry  
 680 parameters  $\Delta p_0$ ,  $\Delta p_1$  and  $\Delta \epsilon_{tag}$  are introduced.

### 681 7.1 OS tagger combination

682 First, the OS electron, muon, neural net kaon and the secondary vertex charge taggers  
 683 are individually calibrated and then combined into a single OS-Combo tagger using the  
 684 `EspressoPerformanceMonitor` tool. We choose the flavour specific decay  $B_s \rightarrow D_s \pi \pi \pi$  as  
 685 calibration mode since it is very similar to the signal decay  $B_s \rightarrow D_s K \pi \pi$ . The calibration  
 686 is performed separately for Run-I and Run-II data. Where available the latest Run-II  
 687 tuning is used for Run-II data, otherwise the Run-I tuning of the taggers is used. Figures  
 688 7.1 and 7.2 show the fitted calibration functions and Tables 7.1 and 7.2 list the measured  
 689 tagging performances.

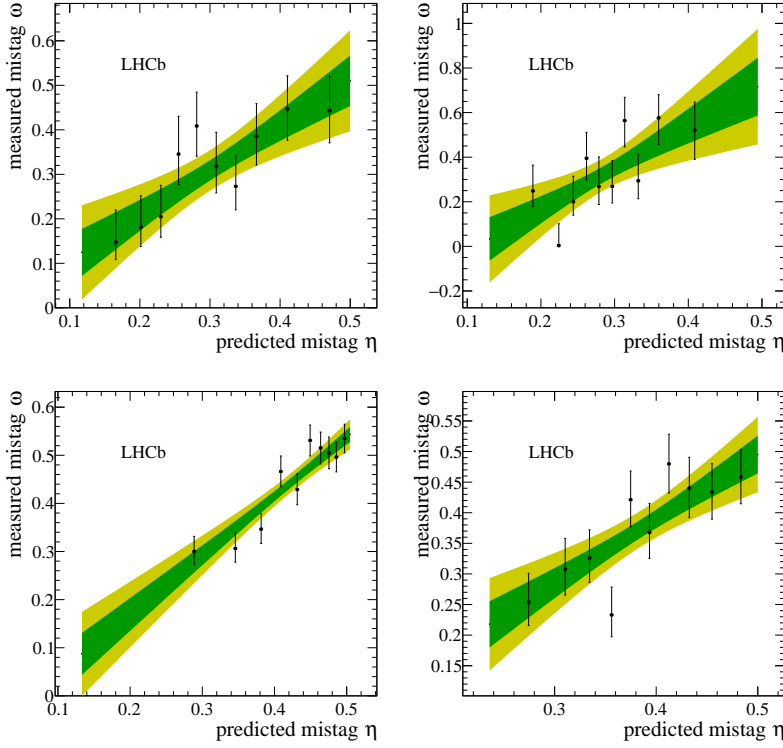


**Figure 7.1:** Predicted versus measured mistag probability for the (top left) OS muon, (top right) OS electron, (bottom left) OS kaon and (bottom right) OS vertex charge tagger for Run-I. A linear fit, including the  $1\sigma$  and  $2\sigma$  error bands is overlaid for each tagger.

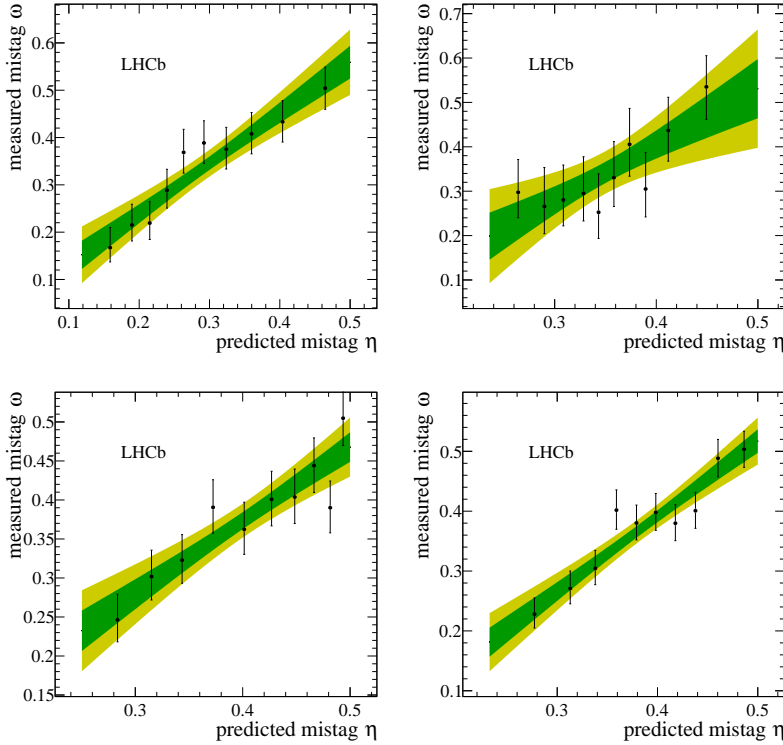


**Figure 7.2:** Predicted versus measured mistag probability for the (top left) OS muon, (top right) OS electron, (bottom left) OS kaon and (bottom right) OS vertex charge tagger for Run-II. A linear fit, including the  $1\sigma$  and  $2\sigma$  error bands is overlaid for each tagger.

**Table 7.1:** The flavour tagging performances for the used OS taggers for Run-I data.

Tagger	$\epsilon$	$\omega$	$\epsilon\langle D^2 \rangle = \epsilon(1 - 2\omega)^2$
OS $\mu$	$(8.775 \pm 0.207)\%$	$(28.935 \pm 0.180(\text{stat}) \pm 2.288(\text{cal}))\%$	$(1.558 \pm 0.045(\text{stat}) \pm 0.338(\text{cal}))\%$
OS $e$	$(3.191 \pm 0.129)\%$	$(28.778 \pm 0.366(\text{stat}) \pm 3.636(\text{cal}))\%$	$(0.575 \pm 0.031(\text{stat}) \pm 0.197(\text{cal}))\%$
OS $K$ NN	$(32.099 \pm 0.342)\%$	$(38.405 \pm 0.094(\text{stat}) \pm 1.152(\text{cal}))\%$	$(1.726 \pm 0.033(\text{stat}) \pm 0.343(\text{cal}))\%$
Vertex Charge	$(21.797 \pm 0.302)\%$	$(35.672 \pm 0.092(\text{stat}) \pm 1.480(\text{cal}))\%$	$(1.790 \pm 0.034(\text{stat}) \pm 0.370(\text{cal}))\%$

**Table 7.2:** The flavour tagging performances for the used OS taggers for Run-II data.

Tagger	$\epsilon$	$\omega$	$\epsilon\langle D^2 \rangle = \epsilon(1 - 2\omega)^2$
OS $\mu$	$(8.904 \pm 0.146)\%$	$(30.119 \pm 0.119(\text{stat}) \pm 1.477(\text{cal}))\%$	$(1.408 \pm 0.029(\text{stat}) \pm 0.209(\text{cal}))\%$
OS $e$	$(3.284 \pm 0.091)\%$	$(32.834 \pm 0.166(\text{stat}) \pm 2.367(\text{cal}))\%$	$(0.387 \pm 0.013(\text{stat}) \pm 0.107(\text{cal}))\%$
OS $K$ NN	$(16.709 \pm 0.191)\%$	$(35.960 \pm 0.075(\text{stat}) \pm 1.076(\text{cal}))\%$	$(1.317 \pm 0.021(\text{stat}) \pm 0.202(\text{cal}))\%$
Vertex Charge	$(20.605 \pm 0.208)\%$	$(34.625 \pm 0.077(\text{stat}) \pm 0.967(\text{cal}))\%$	$(1.948 \pm 0.028(\text{stat}) \pm 0.245(\text{cal}))\%$

## 690 7.2 Tagging performance

691 The OS-Combo and SS-Kaon taggers are calibrated simultaneously by fitting the  $B_s \rightarrow$   
692  $D_s\pi\pi\pi$  decay-time distribution as discussed in Sec. 9. The predicted mistag probabilities  
693  $\eta_{OS}$  and  $\eta_{SS}$ , shown Fig. 7.3 for  $B_s \rightarrow D_s\pi\pi\pi$  and  $B_s \rightarrow D_sK\pi\pi$  data, are included as  
694 per-event observables, effectively giving a larger weight to the events that have a lower  
695 mistag probability. The tagger responses are combined into a single response on an  
696 event-by-event basis during the fit. Tables 7.3 and 7.4 report the tagging performances  
697 for the OS and SS combination considering three mutually exclusive categories of tagged  
698 events: OS only, SS only and both OS and SS.

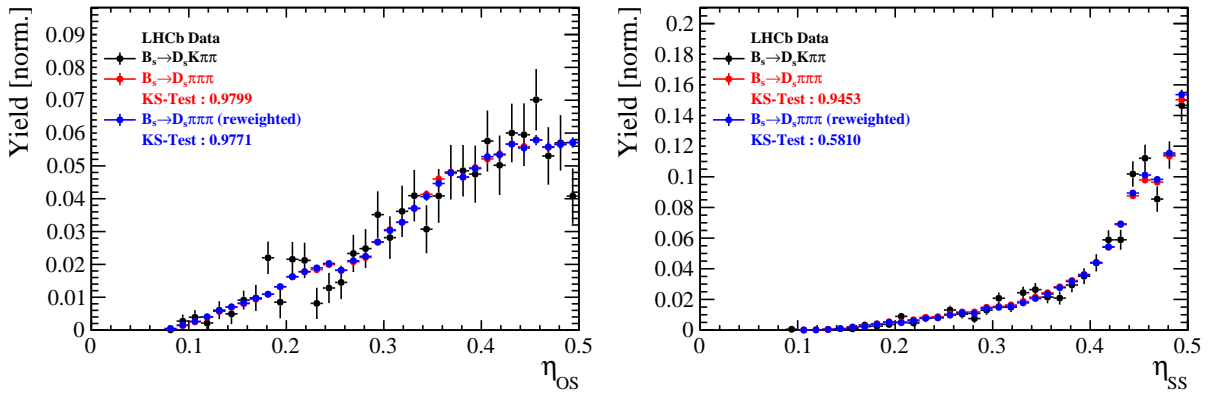


**Figure 7.3:** Distributions of the predicted mistag  $\eta$  for the OS combination (left) and the SS kaon tagger (right) for signal candidates in the  $B_s^0 \rightarrow D_s K\pi\pi$  (black) and  $B_s^0 \rightarrow D_s \pi\pi\pi$  (red) data samples.

**Table 7.3:** The flavour tagging performances for only OS tagged, only SS tagged and both OS and SS tagged events for Run-I data.

$B_s \rightarrow D_s \pi\pi\pi$	$\epsilon_{tag} [\%]$	$\langle \omega \rangle [\%]$	$\epsilon_{eff} [\%]$
Only OS	$14.75 \pm 0.11$	$39.03 \pm 0.82$	$1.27 \pm 0.17$
Only SS	$35.46 \pm 0.18$	$44.15 \pm 0.64$	$1.10 \pm 0.19$
Both OS-SS	$32.92 \pm 0.30$	$37.18 \pm 0.76$	$3.48 \pm 0.35$
Combined	$83.12 \pm 0.37$	$40.48 \pm 0.72$	$5.85 \pm 0.43$

**Table 7.4:** The flavour tagging performances for only OS tagged, only SS tagged and both OS and SS tagged events for Run-II data.

$B_s \rightarrow D_s \pi\pi\pi$	$\epsilon_{tag} [\%]$	$\langle \omega \rangle [\%]$	$\epsilon_{eff} [\%]$
Only OS	$10.92 \pm 0.05$	$36.56 \pm 0.56$	$1.09 \pm 0.07$
Only SS	$43.80 \pm 0.11$	$42.44 \pm 0.37$	$1.99 \pm 0.15$
Both OS-SS	$26.08 \pm 0.14$	$34.87 \pm 0.45$	$3.44 \pm 0.17$
Combined	$80.80 \pm 0.19$	$39.20 \pm 0.42$	$6.52 \pm 0.23$

## 699 8 Production and Detection Asymmetries

### 700 8.1 $B_s$ Production Asymmetry

701 The production rates of  $b$  and  $\bar{b}$  hadrons in  $pp$  collisions are not expected to be identical,  
 702 therefore this effect must be taken into account when computing CP asymmetries. The  
 703 production asymmetry for  $B_s$  mesons is defined as:

$$A_p(B_s^0) = \frac{\sigma(\bar{B}_s^0) - \sigma(B_s^0)}{\sigma(\bar{B}_s^0) + \sigma(B_s^0)} \quad (8.1)$$

704 where  $\sigma$  are the corresponding production cross-section. This asymmetry was measured  
 705 by LHCb in  $pp$  collisions at  $\sqrt{s} = 7$  TeV and  $\sqrt{s} = 8$  TeV by means of a time-dependent  
 706 analysis of  $B_s \rightarrow D_s^- \pi^+$  decays [43]. The results in bins of  $p_T$  and  $\eta$  of the  $B_s$  meson  
 707 are shown in Table 8.1. To correct for the different kinematics of  $B_s \rightarrow D_s^- \pi^+$  and  
 708  $B_s^0 \rightarrow D_s K\pi\pi$  decays, the measured  $B_s$  production asymmetries  $A_p(p_T, \eta)$  are folded with  
 709 the sWeighted  $p_T, \eta$  distribution of our signal channel. The resulting effective production  
 710 asymmetries are:

$$A_p(B_s^0)_{2011} = (-0.506 \pm 1.90)\% \quad (8.2)$$

$$A_p(B_s^0)_{2012} = (-0.164 \pm 1.30)\% \quad (8.3)$$

$$A_p(B_s^0)_{\text{Run-I}} = (-0.045 \pm 1.04)\%. \quad (8.4)$$

711 As for Run-II data no measurement is available yet, we determine the production asym-  
 712 metry from  $B_s \rightarrow D_s \pi\pi\pi$  data together with the tagging parameters.

**Table 8.1:**  $B_s$  production asymmetries in kinematic bins for 2011 and 2012 data. [43]

$p_T$ [ GeV/c ]	$\eta$	$A_p(B_s^0)_{\sqrt{s}=7 \text{ TeV}}$	$A_p(B_s^0)_{\sqrt{s}=8 \text{ TeV}}$
(2.00, 7.00)	(2.10, 3.00)	$0.0166 \pm 0.0632 \pm 0.0125$	$0.0412 \pm 0.0416 \pm 0.0150$
(2.00, 7.00)	(3.00, 3.30)	$0.0311 \pm 0.0773 \pm 0.0151$	$-0.0241 \pm 0.0574 \pm 0.0079$
(2.00, 7.00)	(3.30, 4.50)	$-0.0833 \pm 0.0558 \pm 0.0132$	$0.0166 \pm 0.0391 \pm 0.0092$
(7.00, 9.50)	(2.10, 3.00)	$0.0364 \pm 0.0479 \pm 0.0068$	$0.0482 \pm 0.0320 \pm 0.0067$
(7.00, 9.50)	(3.00, 3.30)	$0.0206 \pm 0.0682 \pm 0.0127$	$0.0983 \pm 0.0470 \pm 0.0155$
(7.00, 9.50)	(3.30, 4.50)	$0.0058 \pm 0.0584 \pm 0.0089$	$-0.0430 \pm 0.0386 \pm 0.0079$
(9.50, 12.00)	(2.10, 3.00)	$-0.0039 \pm 0.0456 \pm 0.0121$	$0.0067 \pm 0.0303 \pm 0.0063$
(9.50, 12.00)	(3.00, 3.30)	$0.1095 \pm 0.0723 \pm 0.0179$	$-0.1283 \pm 0.0503 \pm 0.0171$
(9.50, 12.00)	(3.30, 4.50)	$0.1539 \pm 0.0722 \pm 0.0212$	$-0.0500 \pm 0.0460 \pm 0.0104$
(12.00, 30.00)	(2.10, 3.00)	$-0.0271 \pm 0.0336 \pm 0.0061$	$-0.0012 \pm 0.0222 \pm 0.0050$
(12.00, 30.00)	(3.00, 3.30)	$-0.0542 \pm 0.0612 \pm 0.0106$	$0.0421 \pm 0.0416 \pm 0.0162$
(12.00, 30.00)	(3.30, 4.50)	$-0.0586 \pm 0.0648 \pm 0.0150$	$0.0537 \pm 0.0447 \pm 0.0124$

## 713 8.2 $K^-\pi^+$ Detection Asymmetry

714 The presented measurement of the CKM-angle  $\gamma$  using  $B_s^0 \rightarrow D_s K\pi\pi$  decays is sensitive to  
 715 a possible charge asymmetry of the kaon. Kaons are known to have a nuclear cross-section  
 716 which is asymmetrically dependent on the sign of their charge. It is indispensable to  
 717 determine the charge asymmetry of the kaon, as fitting without taking this effect into  
 718 account would introduce a 'fake' CP violation. Instead of determining the single track  
 719 detection asymmetry of a kaon, it is found that the combined two track asymmetry of a  
 720 kaon-pion pair is much easier to access [44]. Therefore, the two track asymmetry defined  
 721 as

$$A^{det}(K^-\pi^+) = \frac{\epsilon^{det}(K^-\pi^+) - \epsilon^{det}(K^+\pi^-)}{\epsilon^{det}(K^-\pi^+) + \epsilon^{det}(K^+\pi^-)}, \quad (8.5)$$

722 is used.

723 This asymmetry can be measured from the difference in asymmetries in the  $D^+ \rightarrow$   
 724  $K^-\pi^+\pi^+$  and  $D^+ \rightarrow K_s^0\pi^+$  modes [45]:

$$\begin{aligned} A^{det}(K^-\pi^+) &= \frac{N(D^+ \rightarrow K^-\pi^+\pi^+) - N(D^- \rightarrow K^+\pi^-\pi^-)}{N(D^+ \rightarrow K^-\pi^+\pi^+) + N(D^- \rightarrow K^+\pi^-\pi^-)} \\ &\quad - \frac{N(D^+ \rightarrow K_s^0\pi^+) - N(D^- \rightarrow K_s^0\pi^-)}{N(D^+ \rightarrow K_s^0\pi^+) + N(D^- \rightarrow K_s^0\pi^-)} \\ &\quad - A(K^0), \end{aligned} \quad (8.6)$$

725 where possible CP violation in the  $D^+ \rightarrow K_s^0\pi^+$  mode is predicted to be smaller than  
 726  $10^{-4}$  in the Standard Model [46]. The asymmetry in the neutral kaon system,  $A(K^0)$ , has  
 727 to be taken into account as a correction.

728 We use a dedicated LHCb tool to determine  $A^{det}(K^-\pi^+)$  for all data taking periods  
 729 used in this analysis. A detailed description can be found in [45]. The tool provides  
 730 large calibration samples of  $D^\pm \rightarrow K^\pm\pi^\pm\pi^\pm$  and  $D^\pm \rightarrow K_s^0\pi^\pm$  decays, which are used to  
 731 determine the asymmetry following Eq. 8.6. Several weighting steps are performed to  
 732 match the kinematics of the calibration samples to our signal decay sample:

733 First, weights are assigned to the  $K^\pm$  and  $\pi^\pm$  of the  $D^\pm \rightarrow K^\pm\pi^\pm\pi^\pm$  sample, using  
 734  $p, \eta$  of the  $K^\pm$  and  $p_T, \eta$  of the  $\pi^\pm$  from our  $B_s^0 \rightarrow D_s K\pi\pi$  signal decay. Then, weights  
 735 are assigned to the  $D^\pm$  ( $p_T, \eta$ ) and the  $\pi^\pm$  ( $p_T$ ) of the  $D^\pm \rightarrow K_s^0\pi^\pm$  sample to match  
 736 the corresponding, weighted distributions of the  $D^\pm \rightarrow K^\pm\pi^\pm\pi^\pm$  sample. In a last  
 737 step, weights are assigned to match the bachelor pions  $\phi$  distributions between the two  
 738 calibration samples.

739 After the samples are weighted, fits are performed to the invariant  
 740  $m(K^-\pi^+\pi^+)/m(K^+\pi^-\pi^-)$  and  $m(K_s^0\pi^+)/m(K_s^0\pi^-)$  distributions to determine  
 741  $A^{det}(K^-\pi^+)$ . The PDFs used to describe the invariant mass distributions consist of  
 742 gaussian functions for the signal component and exponentials describing the residual  
 743 background.

744 The detection asymmetry is determined separately for every year and (since it is a  
 745 charge asymmetry effect) magnet polarity. Serving as an example for Run-I and Run-  
 746 II, the fits used to determine  $N(D^+ \rightarrow K^-\pi^+\pi^+)/N(D^- \rightarrow K^+\pi^-\pi^-)$  and  $N(D^+ \rightarrow$   
 747  $K_s^0\pi^+)/N(D^- \rightarrow K_s^0\pi^-)$  for 2011, magnet up data and 2015, magnet up data are shown  
 748 in Fig. 8.1 and 8.2 respectively. The obtained values of  $A^{det}(K^-\pi^+) + A(K^0)$  for all years  
 749 and polarities are shown in Table 8.2.

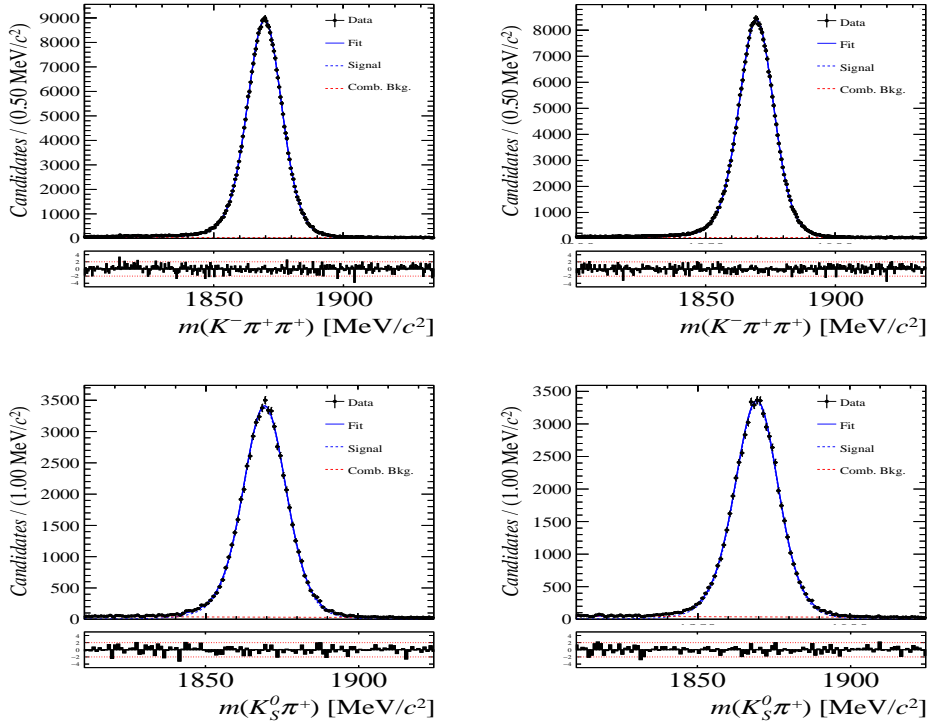


**Figure 8.1:** Distributions of the invariant mass of (top)  $D^\pm \rightarrow K^\pm \pi^\pm \pi^\pm$  and (bottom)  $D^\pm \rightarrow K_S^0 \pi^\pm$  candidates for Run-I data from the calibration samples. A fit described in the text is overlaid.

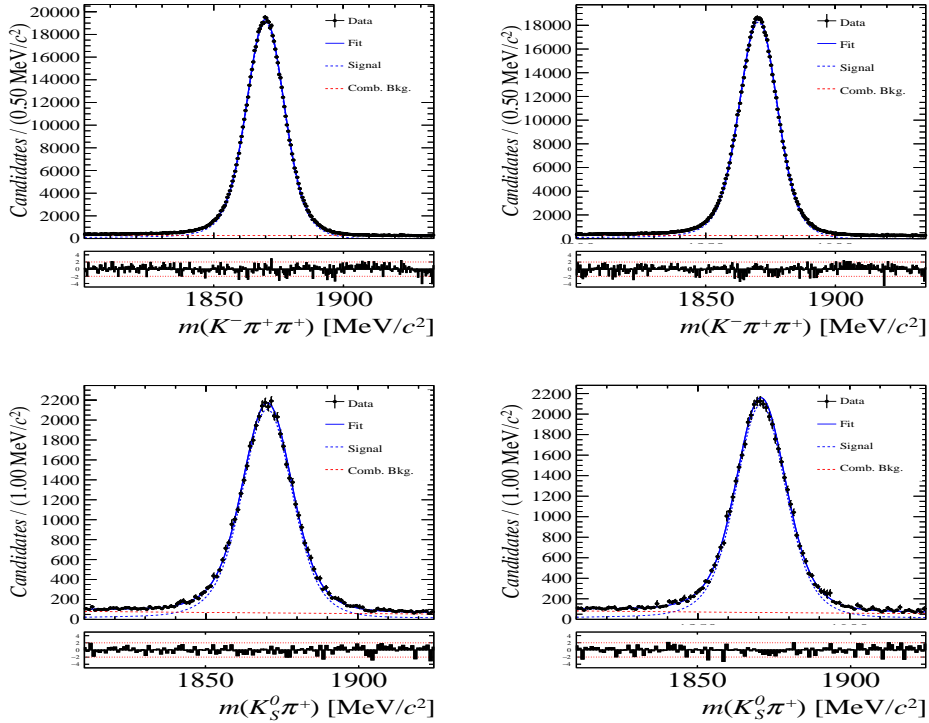


**Figure 8.2:** Distributions of the invariant mass of (top)  $D^\pm \rightarrow K^\pm \pi^\pm \pi^\pm$  and (bottom)  $D^\pm \rightarrow K_S^0 \pi^\pm$  candidates for Run-II data from the calibration samples. A fit described in the text is overlaid.

Data sample	$A^{det}(K^-\pi^+) + A(K^0)$ [%]
Run-I	
2011, mag. up	-2.01 $\pm$ 0.32
2011, mag. down	-0.16 $\pm$ 0.28
2011, average	-1.09 $\pm$ 0.21
2012, mag. up	-0.90 $\pm$ 0.20
2012, mag. down	-1.01 $\pm$ 0.22
2012, average	-0.96 $\pm$ 0.15
Run-II	
mag. up	-1.16 $\pm$ 0.34
mag. down	-0.65 $\pm$ 0.27
average	-0.91 $\pm$ 0.22

**Table 8.2:** Summary of the  $K^-\pi^+$  detection asymmetry obtained from the fits to the Run-I and Run-II calibration samples.

## 9 Decay-time fit

This section covers the (phase space integrated) decay-time fits to  $B_s^0 \rightarrow D_s h\pi\pi$  data. We use the **sFit** technique [47] to statistically subtract the background, leaving only the signal PDF to describe the decay-time. The **sWeights** are calculated based on the fit to the reconstructed  $B_s$  mass distribution described in Sec. 4. The signal PDF is conditional on the tagging decisions  $q_i$ , the mistag estimates  $\eta_i$  ( $i = \text{OS,SS}$ ) and the decay-time error  $\delta t$ :

$$\mathcal{P}(t|\delta t, q_{\text{OS}}, \eta_{\text{OS}}, q_{\text{SS}}, \eta_{\text{SS}}) \propto [p(t' | q_{\text{OS}}, \eta_{\text{OS}}, q_{\text{SS}}, \eta_{\text{SS}}) \otimes \mathcal{R}(t - t', \delta t)] \cdot \epsilon(t) \quad (9.1)$$

where  $p(t|q_{\text{OS}}, \eta_{\text{OS}}, q_{\text{SS}}, \eta_{\text{SS}})$  is given by Equation 2.7 taking the tagging dilution into account. The decay-time acceptance  $\epsilon(t)$  (Sec. 6) and the Gaussian time-resolution function  $\mathcal{R}(t - t', \delta t)$  (Sec. 5) are fixed to the values obtained by the dedicated studies. We fix the values of  $\Gamma_s$  and  $\Delta\Gamma_s$  to the latest HFAG results [38].

The unbinned maximum likelihood fits are performed simultaneously in four categories: [Run-I,L0-TOS], [Run-I,L0-TIS], [Run-II,L0-TOS] and [Run-II,L0-TIS].

### 9.1 Fit to $B_s^0 \rightarrow D_s \pi\pi\pi$ data

Since the decay  $B_s^0 \rightarrow D_s \pi\pi\pi$  is flavour specific, the  $CP$  coefficients can be fixed to  $C = 1$  and  $D_f = D_{\bar{f}} = S_f = S_{\bar{f}} = 0$ . The fit determines the calibration parameters for the OS-Combo and SS-Kaon taggers, the  $B_s^0$  production asymmetry for Run-II data as well as the mixing frequency  $\Delta m_s$ . Table 9.1 summarizes the fitted parameters. The **sWeighted** decay-time distribution and the time-dependent asymmetry  $A_{mix}$  between mixed and unmixed  $B_s^0$  candidates are shown in Fig. 9.1 along with the fit projections.

**Table 9.1:** Parameters determined from a fit to the  $B_s \rightarrow D_s \pi\pi\pi$  decay-time distribution. The uncertainties are statistical and systematic, respectively.

Fit Parameter	Run-I	Run-II
$p_0^{OS}$	$0.397 \pm 0.010 \pm 0.010$	$0.367 \pm 0.005 \pm 0.009$
$p_1^{OS}$	$0.908 \pm 0.087 \pm 0.090$	$0.772 \pm 0.046 \pm 0.063$
$\Delta p_0^{OS}$	$0.030 \pm 0.011 \pm 0.002$	$0.006 \pm 0.006 \pm 0.000$
$\Delta p_1^{OS}$	$0.010 \pm 0.094 \pm 0.015$	$0.085 \pm 0.054 \pm 0.003$
$\epsilon_{\text{tag}}^{OS} [\%]$	$47.667 \pm 0.365 \pm 0.032$	$37.018 \pm 0.181 \pm 0.009$
$\Delta\epsilon_{\text{tag}}^{OS} [\%]$	$0.087 \pm 1.249 \pm 0.093$	$0.185 \pm 0.582 \pm 0.127$
$p_0^{SS}$	$0.443 \pm 0.008 \pm 0.004$	$0.426 \pm 0.004 \pm 0.004$
$p_1^{SS}$	$0.974 \pm 0.110 \pm 0.066$	$0.800 \pm 0.041 \pm 0.050$
$\Delta p_0^{SS}$	$-0.019 \pm 0.009 \pm 0.001$	$-0.017 \pm 0.005 \pm 0.000$
$\Delta p_1^{SS}$	$0.057 \pm 0.125 \pm 0.018$	$0.038 \pm 0.048 \pm 0.004$
$\epsilon_{\text{tag}}^{SS} [\%]$	$0.684 \pm 0.003 \pm 0.000$	$0.699 \pm 0.002 \pm 0.000$
$\Delta\epsilon_{\text{tag}}^{SS} [\%]$	$-0.003 \pm 0.012 \pm 0.001$	$-0.003 \pm 0.006 \pm 0.000$
$A_P [\%]$	$-0.045 \text{ (fixed)}$	$-0.150 \pm 0.618 \pm 0.090$
$\Delta m_s [\text{ps}^{-1}]$		$\text{xx.xx} \pm 0.009 \pm 0.006$

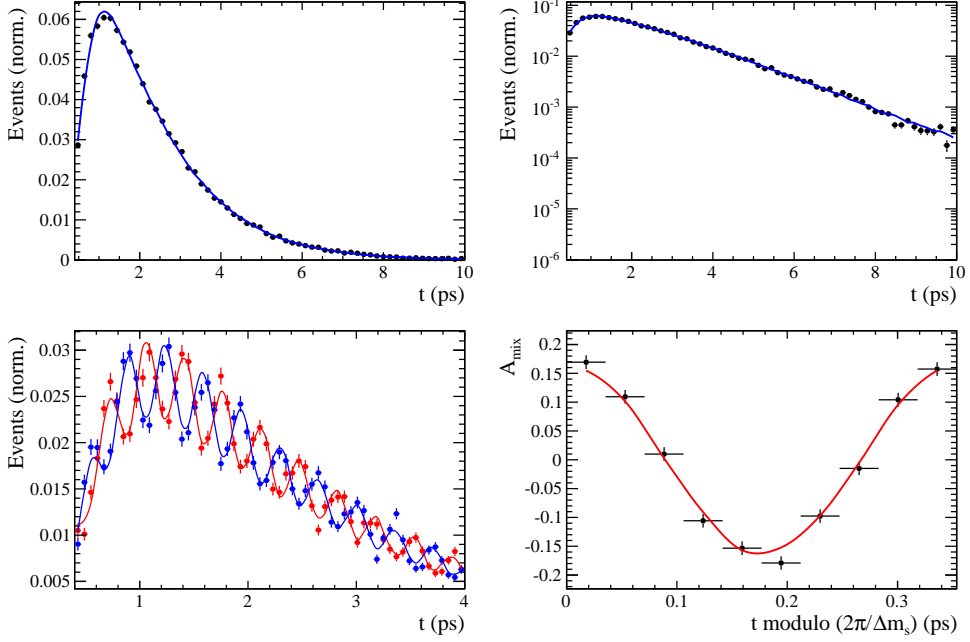


**Figure 9.1:** Top: Flavour averaged decay time distribution of  $B_s^0 \rightarrow D_s\pi\pi\pi$  candidates. Bottom-left: Tagged decay time distribution of mixed (red) and unmixed (blue) signal candidates. Bottom-right: Time-dependent asymmetry  $A_{mix}$  between mixed and unmixed  $B_s^0$  candidates folded into one oscillation period.

## 769 9.2 Fit to $B_s^0 \rightarrow D_s K\pi\pi$ data

770 The measured  $CP$  coefficients  $C, D_f, D_{\bar{f}}, S_f$  and  $S_{\bar{f}}$  extracted from a fit to the  
 771  $B_s \rightarrow D_s K\pi\pi$  decay-time distribution are reported in Table 9.2. The fit projection is  
 772 shown in Fig. 9.2. We included Gaussian-constraints for the tagging calibration parameters  
 773 with the central values and uncertainties determined in Sec. 9.1.

774

775

The  $CP$  coefficients will be converted to the observables  $r, \kappa, \delta, \gamma$  using the Gamma-Combo package after unblinding.

776

Currently the mixing frequency is fixed to the HFAG value. We intend to update  
 777 the fit after unblinding our result from the  $B_s^0 \rightarrow D_s\pi\pi\pi$  fit since our precision is  
 significantly higher.

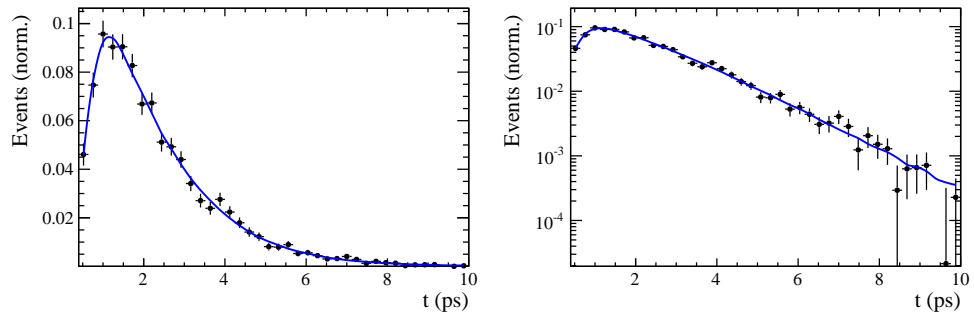


**Figure 9.2:** Decay-time distribution of  $B_s^0 \rightarrow D_s K\pi\pi$  signal candidates with the fit projection overlaid.

**Table 9.2:**  $CP$  coefficients determined from a fit to the  $B_s \rightarrow D_s K\pi\pi$  decay-time distribution. The uncertainties are statistical and systematic, respectively.

Fit Parameter	Value
$C$	x.xx $\pm$ 0.11 $\pm$ 0.02
$D$	x.xx $\pm$ 0.29 $\pm$ 0.08
$\bar{D}$	x.xx $\pm$ 0.27 $\pm$ 0.09
$S$	x.xx $\pm$ 0.16 $\pm$ 0.05
$\bar{S}$	x.xx $\pm$ 0.16 $\pm$ 0.04

## 778 10 Time-dependent amplitude fit

779 The signal PDF used for the full time-dependent fit is defined as

$$\mathcal{P}(\mathbf{x}, t | \delta t, q_{OS}, \eta_{OS}, q_{SS}, \eta_{SS}) \propto [p(\mathbf{x}, t' | q_{OS}, \eta_{OS}, q_{SS}, \eta_{SS}) \otimes \mathcal{R}(t - t', \delta t)] \cdot \epsilon(t) \quad (10.1)$$

780 where  $p(\mathbf{x}, t | q_{OS}, \eta_{OS}, q_{SS}, \eta_{SS})$  is given the differential decay rate in Equation 2.29 taking  
 781 the tagging dilution into account. The phase space efficiency  $\epsilon(\mathbf{x})$  is only included in the  
 782 normalization of  $\mathcal{P}(\mathbf{x}, t | \delta t, q_{OS}, \eta_{OS}, q_{SS}, \eta_{SS})$  as discussed in Sec 6.3. The model selection  
 783 of the amplitude components is described in the following Section. The remaining fitting  
 784 strategy is exactly the same as for the decay-time fits, see Sec. 9.

### 785 10.1 Signal Model Construction

786 The light meson spectrum comprises multiple resonances which are expected to contribute  
 787 to  $B_s \rightarrow D_s K\pi\pi$  decays as intermediate states. Apart from clear contributions coming  
 788 from resonances such as  $K_1(1270)$ ,  $K_1(1400)$ ,  $\rho(770)$  and  $K^*(892)^0$ , the remaining structure  
 789 is impossible to infer due to the cornucopia of broad, overlapping and interfering resonances  
 790 within the phase space boundary. We follow the LASSO [48, 49] approach to limit the  
 791 model complexity in two steps.

792 First, we fit the time-integrated and flavour averaged phase-space distribution of  
 793  $B_s \rightarrow D_s K\pi\pi$  decays. In this case, a single total amplitude can be used:

$$\mathcal{A}_f^{eff}(\mathbf{x}) = \sum_i a_i^{eff} A_i(\mathbf{x}) \quad (10.2)$$

794 which effectively describes the incoherent superposition of the  $b \rightarrow c$  and  $b \rightarrow u$  amplitudes:

$$|A_f^{eff}(\mathbf{x})|^2 = |A_f^c(\mathbf{x})|^2 + |A_f^u(\mathbf{x})|^2. \quad (10.3)$$

795 This significantly simplifies the fitting procedure and allows us to include the whole pool  
 796 of considered intermediate state amplitudes  $A_i$  which can be found in Appendix G. The  
 797 LASSO penalty term added to the likelihood function

$$-2 \log \mathcal{L} \rightarrow -2 \log \mathcal{L} + \lambda \sum_i \sqrt{\int |a_i^{eff} A_i(\mathbf{x})|^2 d\Phi_4}, \quad (10.4)$$

798 shrinks the amplitude coefficients towards zero. The amount of shrinkage is controlled by  
 799 the parameter  $\lambda$ , to be tuned on data. Higher values for  $\lambda$  encourage sparse models, *i.e.*  
 800 models with only a few non-zero amplitude coefficients. The optimal value for  $\lambda$  is found  
 801 by minimizing the Bayesian information criteria [50] (BIC),

$$BIC(\lambda) = -2 \log \mathcal{L} + r \log N_{Sig}, \quad (10.5)$$

802 where  $N_{Sig}$  is the number of signal events and  $r$  is the number of amplitudes with a decay  
 803 fraction above a certain threshold. The fit fractions are defined as

$$F_i \equiv \frac{\int |a_i^{eff} A_i(\mathbf{x})|^2 d\Phi_4}{\int |\mathcal{A}_f^{eff}(\mathbf{x})|^2 d\Phi_4}, \quad (10.6)$$

and are a measure of the relative strength between the different transitions. Figure 10.1(left) shows the distribution of BIC values obtained by scanning over  $\lambda$  where we choose the decay fraction threshold to be 0.5%. At the optimal value of  $\lambda = 50$ , the set of amplitudes with a decay fraction above the threshold are considered further for step two of the model selection. The selected amplitudes and their fractions are summarized in Table 10.1. The fit projections are shown in Fig. 10.2.

In Stage 2, the LASSO procedure is again performed by fitting the full time-dependent amplitude PDF. The components selected by Stage 1 are included for both  $b \rightarrow c$  and  $b \rightarrow u$  transitions and the likelihood is extended as follows:

$$-2 \log \mathcal{L} \rightarrow -2 \log \mathcal{L} + \lambda \sum_i \sqrt{\int |a_i^c A_i(\mathbf{x})|^2 d\Phi_4} + \lambda \sum_i \sqrt{\int |a_i^u A_i(\mathbf{x})|^2 d\Phi_4} \quad (10.7)$$

Figure 10.1(right) shows a plot of the complexity factor  $\lambda$ , against the resulting BIC values. The final set of  $b \rightarrow c$  and  $b \rightarrow u$  amplitudes is selected using the optimal value of  $\lambda = 28$ , and is henceforth called the LASSO model.

**Table 10.1:** Fit fractions of the amplitudes selected by Stage 1 of the model selection procedure.

Decay channel	Fraction [%]
$B_s \rightarrow K(1)(1270)^+ (\rightarrow K^*(892)^0 (\rightarrow K^+ \pi^-) \pi^+) D_s^-$	$8.56 \pm 1.43$
$B_s \rightarrow K(1)(1400)^+ (\rightarrow K^*(892)^0 (\rightarrow K^+ \pi^-) \pi^+) D_s^-$	$43.72 \pm 2.80$
$B_s \rightarrow K(1460)^+ (\rightarrow K^*(892)^0 (\rightarrow K^+ \pi^-) \pi^+) D_s^-$	$3.25 \pm 0.69$
$B_s \rightarrow K^*(1410)^+ (\rightarrow K^*(892)^0 (\rightarrow K^+ \pi^-) \pi^+) D_s^-$	$15.33 \pm 1.13$
$B_s \rightarrow (D_s^- \pi^+)_P K^*(892)^0 (\rightarrow K^+ \pi^-)$	$4.63 \pm 0.69$
$B_s \rightarrow K^*(1410)^+ (\rightarrow \rho(770)^0 (\rightarrow \pi^+ \pi^-) K^+) D_s^-$	$5.58 \pm 0.62$
$B_s \rightarrow (D_s^- K^+)_P \rho(770)^0 (\rightarrow \pi^+ \pi^-)$	$1.49 \pm 0.40$
$B_s \rightarrow K(1)(1270)^+ (\rightarrow K(0)^*(1430)^0 (\rightarrow K^+ \pi^-) \pi^+) D_s^-$	$4.72 \pm 0.54$
$B_s \rightarrow K(1)(1270)^+ (\rightarrow \rho(770)^0 (\rightarrow \pi^+ \pi^-) K^+) D_s^-$	$14.20 \pm 1.56$
Sum	$101.47 \pm 3.86$

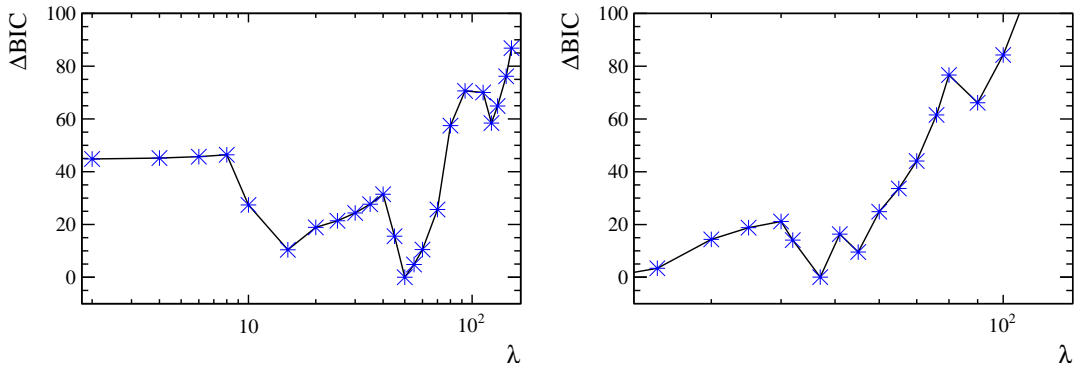


**Figure 10.1:** Difference in the BIC value from its minimum as function of the LASSO parameter  $\lambda$  for step 1 (left) and step 2 (right) of the model selection.

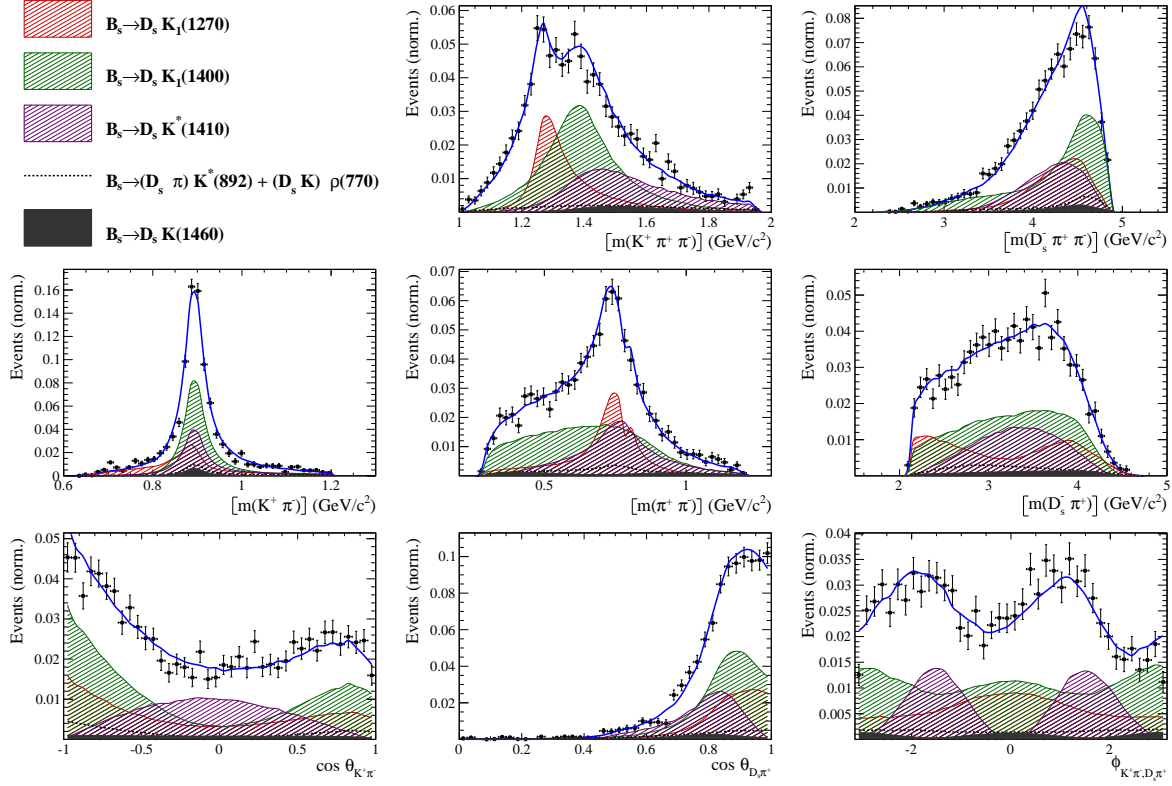


**Figure 10.2:** Projections of the fit result to the time-integrated and flavour averaged phase-space distribution of  $B_s \rightarrow D_s K\pi\pi$  decays.

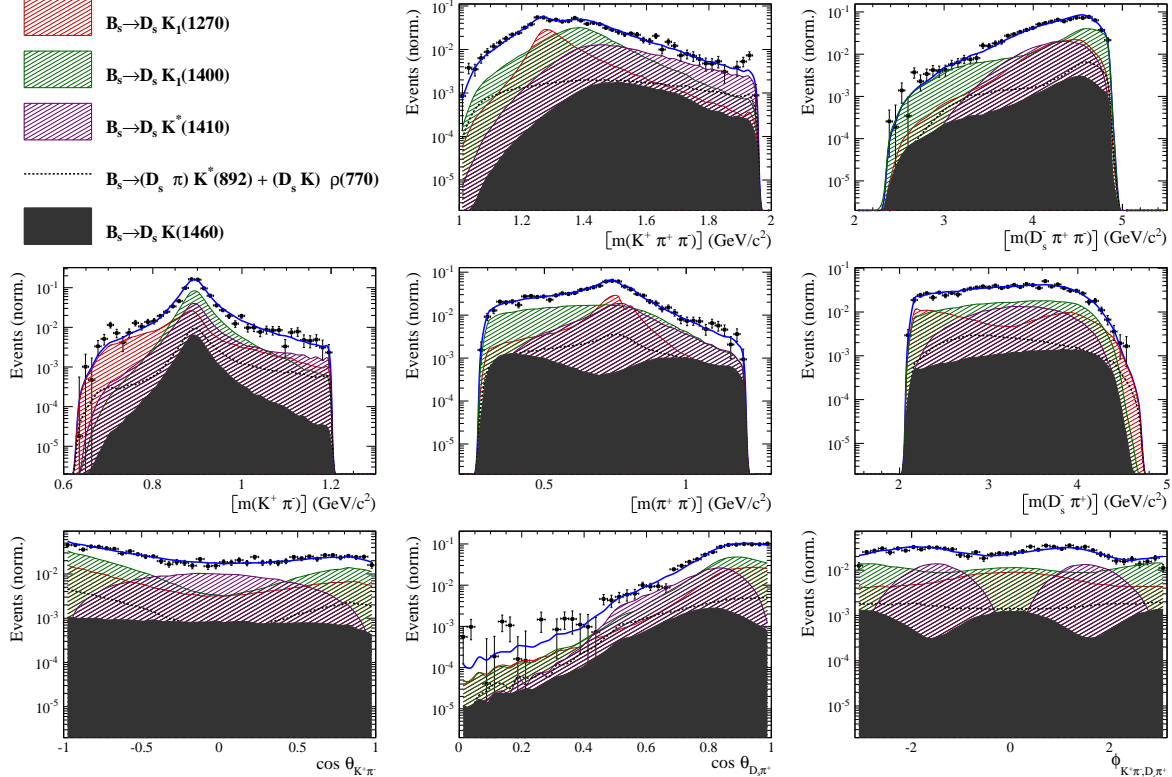


**Figure 10.3:** Projections of the fit result to the time-integrated and flavour averaged phase-space distribution of  $B_s \rightarrow D_s K\pi\pi$  decays in logarithmic scale.

## 816 10.2 Results

817 Table 10.2 lists the modulus and phases of the complex amplitude coefficients  $a_i^c$  and  $a_i^u$ ,  
 818 obtained by fitting the LASSO model to the data. The corresponding fit fractions for the  
 819  $b \rightarrow c$  and  $b \rightarrow u$  amplitudes are individually normalized

$$F_i^{c,u} \equiv \frac{\int |a_i^{c,u} A_i(\mathbf{x})|^2 d\Phi_4}{\int |\mathcal{A}_f^{c,u}(\mathbf{x})|^2 d\Phi_4} \quad (10.8)$$

820 and shown in Table 10.3. In addition to the amplitude coefficients, the amplitude ratio  
 821 and the strong and weak phase differences between the  $b \rightarrow c$  and  $b \rightarrow u$  decays are  
 822 determined. Moreover, the masses and widths of the  $K_1(1400)$  and  $K^*(1410)$  resonances  
 823 are fitted.

824 Figure 10.4 shows the distributions of selected phase space observables, which demon-  
 825 strate reasonable agreement between data and the fit model. We also project into the  
 826 transversity basis to demonstrate good description of the overall angular structure. The  
 827 acoplanarity angle  $\chi$ , is the angle between the two decay planes formed by the  $K^+ \pi^-$   
 828 system and the  $D_s^- \pi^+$  system in the  $B_s$  rest frame; boosting into the rest frames of the  
 829 two-body systems defining these decay planes, the two helicity variables are defined as  
 830 the cosine of the angle,  $\theta$ , of the  $K^+$  or  $D_s^-$  momentum with the  $B_s$  flight direction.

831 In order to quantify the quality of the fit in the five-dimensional phase space, a  $\chi^2$   
 832 value is determined by binning the data;

$$\chi^2 = \sum_{b=1}^{N_{\text{bins}}} \frac{(N_b - N_b^{\text{exp}})^2}{N_b^{\text{exp}}}, \quad (10.9)$$

833 where  $N_b$  is the number of data events in a given bin,  $N_b^{\text{exp}}$  is the event count predicted  
 834 by the fitted PDF and  $N_{\text{bins}}$  is the number of bins. An adaptive binning is used to ensure  
 835 sufficient statistics in each bin for a robust  $\chi^2$  calculation [51]. At least 25 events per  
 836 bin are required. The number of degrees of freedom  $\nu$ , in an unbinned fit is bounded by  
 837  $N_{\text{bins}} - 1$  and  $(N_{\text{bins}} - 1) - N_{\text{par}}$ , where  $N_{\text{par}}$  is the number of free fit parameters. We use  
 838 the  $\chi^2$  value divided by  $\nu = (N_{\text{bins}} - 1) - N_{\text{par}}$  as a conservative estimate. For the LASSO  
 839 model, this amounts to  $\chi^2/\nu = 1.40$  indicating a decent fit quality.

**Table 10.2:** Modulus and phases of the amplitudes contributing to  $b \rightarrow c$  and  $b \rightarrow u$  decays. In case of multiple decay modes of three-body resonances, the amplitude coefficients are defined relative to the one listed first. Additional fit parameters are listed below. The first quoted uncertainty is statistical, while the second arises from systematic sources. The third uncertainty arises from the alternative models considered.

Decay Channel	$A_{b \rightarrow c}$		$A_{b \rightarrow u}$	
	$ a_i $	$\arg(a_i)[^\circ]$	$ a_i $	$\arg(a_i)[^\circ]$
$B_s \rightarrow D_s (K_1(1270) \rightarrow K \rho(770))$	1.0	0.0	1.0	0.0
$K_1(1270) \rightarrow K^*(892) \pi$	$0.76 \pm 0.11 \pm 0.16$	$60.9 \pm 9.6 \pm 14.1$		
$K_1(1270) \rightarrow K_0^*(1430) \pi$	$0.68 \pm 0.06 \pm 0.34$	$116.5 \pm 5.1 \pm 43.5$		
$B_s \rightarrow D_s (K_1(1400) \rightarrow K^*(892) \pi)$	$2.53 \pm 0.27 \pm 0.57$	$12.9 \pm 7.4 \pm 8.2$	$0.67 \pm 0.20 \pm 0.51$	$-76.3 \pm 16.9 \pm 22.9$
$B_s \rightarrow D_s (K^*(1410) \rightarrow K^*(892) \pi)$	$1.28 \pm 0.12 \pm 0.25$	$54.9 \pm 5.6 \pm 10.0$		
$K^*(1410) \rightarrow K \rho(770)$	$0.66 \pm 0.04 \pm 0.04$	$-172.9 \pm 5.0 \pm 6.7$		
$B_s \rightarrow D_s (K(1460) \rightarrow K^*(892) \pi)$			$0.77 \pm 0.11 \pm 0.62$	$-93.6 \pm 11.2 \pm 12.6$
$B_s \rightarrow (D_s \pi)_P K^*(892)$	$1.02 \pm 0.13 \pm 0.41$	$-28.4 \pm 8.0 \pm 10.5$	$0.79 \pm 0.18 \pm 0.36$	$3.7 \pm 12.5 \pm 15.1$
$B_s \rightarrow (D_s K)_P \rho(770)$			$0.61 \pm 0.08 \pm 0.26$	$36.4 \pm 7.7 \pm 14.5$
Fit parameter	Value			
$m_{K_1(1400)} [\text{MeV}]$	$1394.9 \pm 8.8 \pm 12.7 \pm 21.2$			
$\Gamma_{K_1(1400)} [\text{MeV}]$	$224.0 \pm 15.9 \pm 22.3 \pm 20.9$			
$m_{K^*(1410)} [\text{MeV}]$	$1419.6 \pm 10.8 \pm 26.9 \pm 24.1$			
$\Gamma_{K^*(1410)} [\text{MeV}]$	$342.4 \pm 23.5 \pm 51.7 \pm 52.9$			
$r$	$xx.xx \pm 0.04 \pm 0.05 \pm 0.04$			
$\delta [^\circ]$	$xx.xx \pm 16.1 \pm 6.8 \pm 6.8$			
$\gamma - 2\beta_s [^\circ]$	$xx.xx \pm 16.1 \pm 11.6 \pm 6.2$			

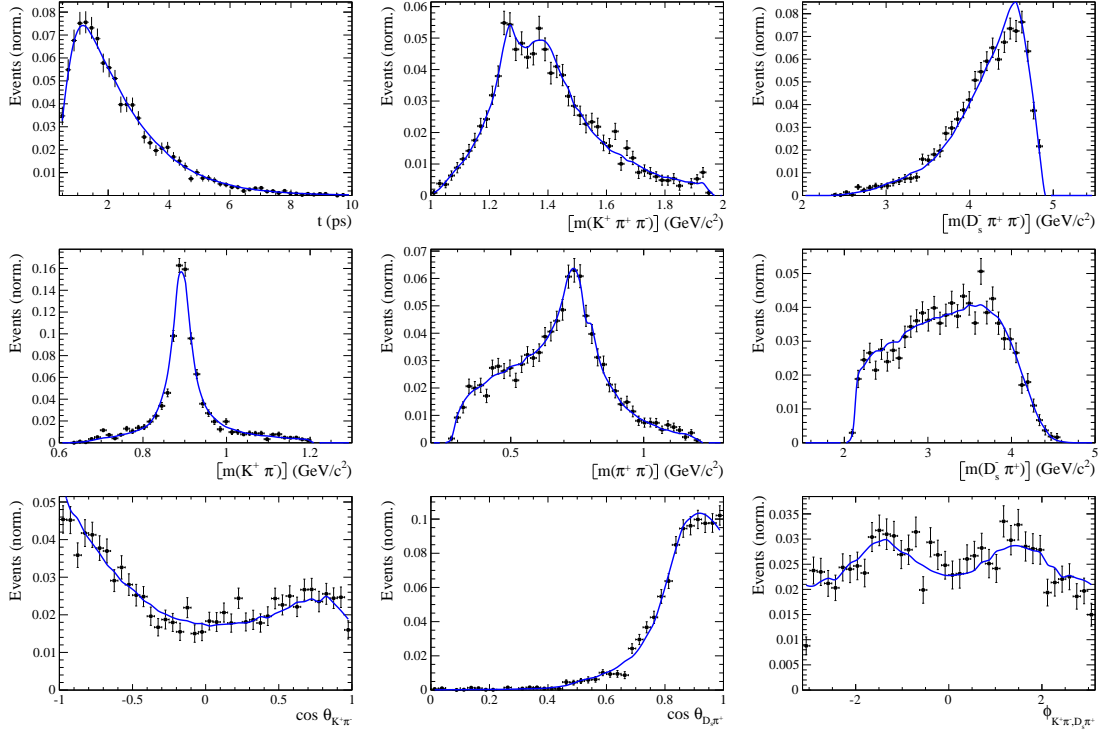


**Figure 10.4:** Projections of the full time-dependent amplitude fit.

**Table 10.3:** Fit fractions of the amplitudes contributing to  $b \rightarrow c$  and  $b \rightarrow u$  decays.

Decay Channel	$F_{b \rightarrow c} [\%]$	$F_{b \rightarrow u} [\%]$
$B_s \rightarrow D_s (K_1(1270) \rightarrow K^*(892) \pi)$	$5.2 \pm 1.2$	$17.6 \pm 4.2$
$B_s \rightarrow D_s (K_1(1270) \rightarrow K \rho(770))$	$9.4 \pm 1.1$	$32.0 \pm 4.9$
$B_s \rightarrow D_s (K_1(1270) \rightarrow K_0^*(1430) \pi)$	$4.5 \pm 0.6$	$15.2 \pm 2.4$
$B_s \rightarrow D_s (K_1(1400) \rightarrow K^*(892) \pi)$	$59.9 \pm 5.0$	$16.6 \pm 8.5$
$B_s \rightarrow D_s (K^*(1410) \rightarrow K^*(892) \pi)$	$14.8 \pm 0.9$	
$B_s \rightarrow D_s (K^*(1410) \rightarrow K \rho(770))$	$7.0 \pm 0.6$	
$B_s \rightarrow D_s (K(1460) \rightarrow K^*(892) \pi)$		$18.8 \pm 4.2$
$B_s \rightarrow (D_s \pi)_P K^*(892)$	$9.7 \pm 1.8$	$21.8 \pm 7.2$
$B_s \rightarrow (D_s K)_P \rho(770)$		$13.5 \pm 4.0$
<i>Sum</i>	$110.5 \pm 5.4$	$135.4 \pm 10.3$

## 840 11 Systematic uncertainties

841 The systematic uncertainties on the measured observables are summarized in Table 11.1 for  
842 the decay-time fit to  $B_s \rightarrow D_s \pi\pi\pi$ , in Table 11.2 for the decay-time fit to  $B_s \rightarrow D_s K\pi\pi$   
843 and in Table 11.3 for the full time-dependent amplitude fit to  $B_s \rightarrow D_s K\pi\pi$  decays. A  
844 description of each systematic effect is given in the following subsections starting with the  
845 ones common to all fits. Afterwards, systematic effect specific to the amplitude description  
846 are discussed.

### 847 11.1 Fit bias

848 Pseudo-experiments are performed, where a signal toy sample of the same size as the  
849 number of observed signal data events is generated according to the nominal fit model  
850 and subsequently fitted with the same model. The means of the pull distributions are  
851 taken as systematic uncertainties of the fit parameters.

### 852 11.2 Background subtraction

853 The statistical subtraction of the residual background [47], left after the full selection,  
854 relies on the correct description of the invariant  $B_s^0$  mass distribution. Since the choice of  
855 signal and background models is not unique, alternative parameterizations are tested:

- 856 • The Johnson's SU function which is used as nominal signal model is replaced by the  
857 sum of two Crystal Ball functions [52].
- 858 • For the combinatorial background, the nominal second order polynomial is replaced  
859 by an exponential function.
- 860 • For the description of the partially reconstructed background, a combination of the  
861 RooHILLdini and RooHORNsdini model [53] is used instead of the nominal model of  
862 three bifurcated gaussians.
- 863 • For the shape of the mis-ID background, the nominal approach is to use a simulated  
864 sample of  $B_s^0 \rightarrow D_s^- \pi^+ \pi^- \pi^+$  or  $B_s^0 \rightarrow D_s^{*-} \pi^+ \pi^- \pi^+$  decays and flip the mass  
865 hypothesis of the  $\pi^+$  with the higher misidentification probability (see Sec. 4).  
866 Two alternative approaches are considered: we flip the mass hypothesis of the  $\pi^+$   
867 candidate with the lower probability of being misidentified; we randomly flip the  
868 mass hypothesis of a  $\pi^+$  candidate.

869 To evaluate the possible source of systematic uncertainty arising from the fixed yields of  
870 the mis-ID backgrounds, the yields are fixed to zero or doubled.

871 In total 15 (7) different combinations of the modifications discussed above are tested  
872 for the fit to the  $D_s K\pi\pi$  ( $D_s \pi\pi\pi$ ) mass distribution. For each case, new signal **sWeights**  
873 are calculated and the **sFits** to data are repeated. The sample variance of the obtained  
874 differences to the nominal fit value are used as systematic uncertainty due to the background  
875 subtraction.

876 **11.3 Decay-time acceptance**

877 The systematic uncertainty related to the decay-time efficiency as well as  $\Gamma_s$  and  $\Delta\Gamma_s$  are  
 878 studied simultaneously. We generate toys in the nominal configuration and fit back in  
 879 both this nominal configuration and a configuration in which we have randomized the  
 880 acceptance parameters together with  $\Gamma_s$  and  $\Delta\Gamma_s$  within their uncertainties. For each toy,  
 881 a pull is calculated by dividing the difference between the fitted values of the nominal  
 882 and shifted configurations by the uncertainty in the nominal toy. We add the bias in the  
 883 mean of this pull to its width, in quadrature, in order to arrive at the final systematic  
 884 uncertainty.

885 To improve the coverage of the multi-dimensional parameter space, a Cholesky decom-  
 886 position [54] is used to generate a set of uncorrelated vectors from the covariance matrix  
 887  $\text{cov}(\lambda_i, \lambda_j)$ , where the vector  $\lambda$  includes the parameters  $\Gamma_s$ ,  $\Delta\Gamma_s$  and the  $N = 4$  spline  
 888 coefficients for each category of the simultaneous fit. The correlations between  $\Gamma_s$  ( $\Delta\Gamma_s$ )  
 889 and the spline coefficients are measured by rerunning the acceptance fits described in  
 890 Sec. 6.2 with the values of  $\Gamma_s$  ( $\Delta\Gamma_s$ ) varied by  $\pm 1\sigma$  and measuring the shift in the spline  
 891 coefficients as a fraction of their uncertainty. For the correlation between  $\Gamma_s$  and  $\Delta\Gamma_s$  we  
 892 use the HFAG value [38].

893 **11.4 Decay-time resolution and tagging**

894 To study systematic effects originating from the scaling of the decay-time error estimate,  
 895 two different approaches which either slightly overestimate or underestimate the resolution  
 896 are used:

- 897 • A double Gaussian is fit to the decay-time distributions of fake  $B_s^0$  candidates, but  
 898 only the width of the core Gaussian is considered to represent the time resolution in  
 899 the respective bin. Therefore the resolution is slightly underestimated in this case.
- 900 • A single Gaussian is fit to the decay-time distributions of fake  $B_s^0$  candidates in a  
 901 wide range of  $[-3\sigma_t : 1.5\sigma_t]$ . Due to the tails of the distribution, which broaden the  
 902 width of the Gaussian function, this method slightly overestimates the decay-time  
 903 resolution.

904 For each case, a new scaling function is derived:

$$\sigma_{\text{eff}}^{\text{core-Gauss}}(\sigma_t) = (4.9 \pm 2.0) \text{ fs} + (0.821 \pm 0.050) \sigma_t \quad (11.1)$$

$$\sigma_{\text{eff}}^{\text{single-Gauss}}(\sigma_t) = (8.3 \pm 1.5) \text{ fs} + (0.997 \pm 0.037) \sigma_t \quad (11.2)$$

905 which are compared to the nominal result in Fig. 11.1.

906 Due to the high correlation between the decay-time resolution and the tagging calibra-  
 907 tion, their systematic uncertainty has to be studied simultaneously. First, the decay-time  
 908 fits to  $B_s \rightarrow D_s \pi \pi$  data are repeated using the alternative decay-time error scaling  
 909 functions. New tagging calibration parameters are obtained which are then used (together  
 910 with the respective decay-time error scaling function) in the fits to  $B_s \rightarrow D_s K \pi \pi$  data  
 911 to define the Gaussian-constraints as discussed in Sec. 9. For the width of the Gaussians  
 912 only the statistical error of the tagging calibration parameters are used since systematic  
 913 uncertainties (except the systematic arising from the decay-time resolution which is already  
 914

included by the procedure described above) are found to be negligible, see Table 11.1.  
 Finally, we take the biggest change in fit central value as the systematic for each parameter  
 of the  $B_s \rightarrow D_s K \pi \pi$  fits.

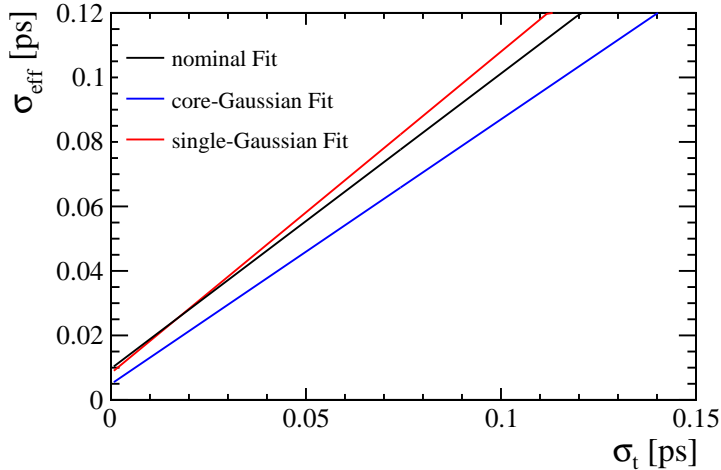


**Figure 11.1:** The measured resolution scaling function of the per-event decay time error estimate  $\sigma_t$  for fake  $B_s$  candidates (Run-II data) for (black line) the nominal scaling, (blue line) only using the narrow gaussian width of the double gaussian fit model or (red line) when determining the resolution using a single gaussian model.

## 11.5 Production, detection asymmetries and mixing frequency

The systematic from the production, detection asymmetries and  $\Delta m_s$  (in case of  $B_s \rightarrow D_s K \pi \pi$  decays) which are fixed in the fit are evaluated by means of a toy study similar to the procedure performed for the time-acceptance. The parameters are assumed to be uncorrelated.

## 11.6 Multiple candidates

The fraction of events with multiple candidates has been found to be very small, it is 1.6% for  $D_s K \pi \pi$  and 1.5% for  $D_s \pi \pi \pi$ . Thus the nominal result is obtained keeping all candidates, while a systematic uncertainty is assigned by repeating the fit randomly keeping only one candidate when multiple ones are founds. No shifts in the fit central values are observed.

## 11.7 Length and momentum scales

The uncertainty on the LHCb length scale is estimated to be at most 0.020% [55], which translates directly in an uncertainty on  $\Delta m_s$  of 0.020% with other parameters being unaffected. The momentum scale uncertainty is at most 0.022%.

933 **11.8 Phase space acceptance**

934 For the phase space acceptance we rely on simulated data. The integration error due  
935 to the limited size of the MC sample used to normalize the signal PDF is evaluated by  
936 bootstrapping the MC sample and repeating the full time-dependent amplitude fit.

937 To asses the uncertainty due to possible data-simulation differences, we determine  
938 alternative phase space efficiencies by varying the selection requirements on quantities  
939 that are expected not to be well described by the simulation. In particular, we consider  
940 the following variations:

- 941     • No BDT cut is applied
- 942     • A tighter BDT requirement is used ( $\text{BDTG} > 0.6$ )
- 943     • No reweighting is applied
- 944     • Instead of the PID responses obtained from the `PIDCorr` tool, we use the `PIDGen`  
945       tool to resample the PID variables [37]
- 946     • The raw MC PID variables are used
- 947     • Candidates with `BKGAT= 60` are removed

948 We assign the sample variance of the fitted values using the alternative phase space  
949 acceptances as systematic.

950 This will be done when the final MC samples are available. We expect the integration  
error to be negligible and the systematic error from data-simulation differences  
to be small. At the moment we estimate a systematic by assuming a flat phase space  
acceptance. The resulting uncertainties shown in Table 11.3 should be considered as  
upper limit and illustrate that we are not highly sensitive to the details of the phase  
space acceptance shape.

951 **11.9 Resonance description**

952 The following alternative line shape parameterizations are considered as part of the  
953 systematic studies:

- 954     • The Lass description for the  $K\pi$   $S$ -wave is replaced by a relativistic Breit-Wigner  
955       propagator (Equation 2.16)
- 956     • The Gounaris-Sakurai description for the  $\rho(770)$  is replaced by a relativistic Breit-  
957       Wigner propagator (Equation 2.16)
- 958     • The  $\omega$  contribution to the decay channel  $K_1(1270) \rightarrow K \rho(770)/\omega$  is set to zero
- 959     • For the decay channel  $K^*(1410) \rightarrow K \rho(770)$ , we include  $\rho(770) - \omega$  mixing with a  
960       relative magnitude and phase determined from data
- 961     • Instead of taking the energy-dependent widths of the three-body resonances from  
962       Refs. [9, 21], we derive them from Equation 2.17 assuming an uniform phase space  
963       population.

964 The data fits are repeated for each alternative model and the shifts of the central values  
965 are taken as systematic uncertainties. They are added in quadrature.

966 The uncertainties due to fixed masses and widths of resonances are evaluated from  
967 toys where we vary them one-by-one within their quoted errors. In our nominal fit, the  
968 Blatt-Weisskopf radial parameter is set to  $r_{BW} = 1.5 \text{ GeV}^{-1}$ . Again, toys are generated  
969 according to this nominal configuration and then fitted whereby the radial parameter is  
970 uniformly varied within the interval  $[0, 3] \text{ GeV}^{-1}$ .

## 971 11.10 Alternative amplitude models

972 We tested several modifications of the LASSO model to assign an additional model  
973 uncertainty to the measured observables  $r, \delta$  and  $\gamma - 2\beta_s$  as well as to the measured  
974 masses and widths of the  $K_1(1400)$  and  $K^*(1410)$  resonances. The amplitude coefficients  
975 are by definition parameters of a given model which is why we do not evaluate a model  
976 uncertainty for them.

- 977 • All amplitudes selected by Stage 1 of the model selection are included for both  
978  $b \rightarrow c$  and  $b \rightarrow u$  transitions
- 979 • The decay channel  $K_1(1270)[D] \rightarrow K^*(892)\pi$  is added where the  $K^*(892)\pi$  system  
980 is in relative a D-wave state
- 981 • The decay channel  $K_1(1400) \rightarrow K\rho(770)$  is added
- 982 • The decay channels  $K_2^*(1430) \rightarrow K\rho(770)$  and  $K_2^*(1430) \rightarrow K^*(892)\pi$  are added
- 983 • The decay channels  $K(1460) \rightarrow K\rho(770)$  and  $K(1460) \rightarrow K\sigma$  are added
- 984 • The  $K(1460)$  resonance is removed
- 985 • The decay channels  $K^*(1680) \rightarrow K\rho(770)$  and  $K^*(1680) \rightarrow K^*(892)\pi$  are added
- 986 • The decay channels  $K_2(1770) \rightarrow K\rho(770)$  and  $K_2(1770) \rightarrow K^*(892)\pi$  are added
- 987 • The amplitudes  $B_s \rightarrow (D_s\pi)_P K^*(892)$  and  $B_s \rightarrow (D_sK)_P \rho(770)$  are replaced by  
988  $B_s \rightarrow (D_s\pi)_S K^*(892)$  and  $B_s \rightarrow (D_sK)_S \rho(770)$
- 989 • Higher orbital angular momentum states are added for the amplitudes:  $B_s[S, P, D] \rightarrow$   
990  $(D_s\pi)_P K^*(892)$  and  $B_s[S, P, D] \rightarrow (D_sK)_P \rho(770)$
- 991 • The amplitudes  $B_s \rightarrow (D_s\pi)_P K^*(892)$  and  $B_s \rightarrow (D_sK)_P \rho(770)$  are removed
- 992 • The amplitudes  $B_s \rightarrow (D_sK)_P \sigma$ ,  $B_s \rightarrow (D_sK)_P f_2(1270)$  and  $B_s \rightarrow$   
993  $(D_sK)_P f_0(1370)$  are added
- 994 • The amplitudes  $B_s \rightarrow (D_s\pi)_P K_0^*(1430)$  and  $B_s \rightarrow (D_sK)_S K_2^*(1430)$  are added

995 In total 20 different sets of amplitudes are fitted. In some cases, the fit fractions of  
996 additionally added amplitudes turn out to be exactly zero. These model are effectively  
997 not distinguishable from the baseline LASSO model and are not considered further. From  
998 the remaining 15 models, we compute the sample variance for each observable and take it  
999 as model uncertainty.

**Table 11.1:** Systematic uncertainties on the fit parameters of the fit to  $B_s \rightarrow D_s\pi\pi\pi$  data in units of statistical standard deviations.

Fit Parameter	Fit-bias	Acceptance	Resolution	Asymmetries	Background	Mult.-Cand.	Mom./z-Scale	Total
$p_0^{OS}$ Run-I	0.04	0.00	0.99	0.01	0.04	0.00		0.99
$p_1^{OS}$ Run-I	0.01	0.00	1.03	0.00	0.05	0.00		1.03
$\Delta p_0^{OS}$ Run-I	0.03	0.00	0.02	0.15	0.02	0.00		0.16
$\Delta p_1^{OS}$ Run-I	0.02	0.00	0.03	0.16	0.02	0.00		0.16
$\epsilon_{tag}^{OS}$ Run-I	0.02	0.00	0.00	0.01	0.09	0.00		0.09
$\Delta \epsilon_{tag}^{OS}$ Run-I	0.03	0.00	0.07	0.01	0.02	0.00		0.07
$p_0^{SS}$ Run-I	0.01	0.00	0.55	0.00	0.03	0.00		0.55
$p_1^{SS}$ Run-I	0.04	0.00	0.60	0.01	0.03	0.00		0.60
$\Delta p_0^{SS}$ Run-I	0.00	0.00	0.00	0.10	0.01	0.00		0.10
$\Delta p_1^{SS}$ Run-I	0.07	0.00	0.01	0.12	0.03	0.00		0.15
$\epsilon_{tag}^{SS}$ Run-I	0.02	0.00	0.00	0.01	0.01	0.00		0.03
$\Delta \epsilon_{tag}^{SS}$ Run-I	0.04	0.00	0.05	0.01	0.02	0.00		0.07
$p_0^{OS}$ Run-II	0.01	0.01	1.65	0.00	0.10	0.00		1.65
$p_1^{OS}$ Run-II	0.01	0.00	1.37	0.00	0.10	0.00		1.38
$\Delta p_0^{OS}$ Run-II	0.05	0.00	0.06	0.00	0.03	0.00		0.08
$\Delta p_1^{OS}$ Run-II	0.02	0.00	0.03	0.00	0.04	0.00		0.05
$\epsilon_{tag}^{OS}$ Run-II	0.02	0.00	0.00	0.00	0.04	0.00		0.05
$\Delta \epsilon_{tag}^{OS}$ Run-II	0.01	0.00	0.21	0.00	0.04	0.00		0.22
$p_0^{SS}$ Run-II	0.00	0.00	1.06	0.00	0.03	0.00		1.06
$p_1^{SS}$ Run-II	0.07	0.00	1.22	0.00	0.03	0.00		1.22
$\Delta p_0^{SS}$ Run-II	0.00	0.00	0.02	0.00	0.03	0.00		0.04
$\Delta p_1^{SS}$ Run-II	0.07	0.00	0.03	0.00	0.03	0.00		0.08
$\epsilon_{tag}^{SS}$ Run-II	0.00	0.00	0.00	0.00	0.04	0.00		0.04
$\Delta \epsilon_{tag}^{SS}$ Run-II	0.02	0.00	0.05	0.00	0.02	0.00		0.06
$A_P$ Run-II	0.10	0.00	0.10	0.01	0.03	0.00		0.14
$\Delta m_s$	0.01	0.00	0.15	0.03	0.06	0.00	0.61	0.63

**Table 11.2:** Systematic uncertainties on the fit parameters of the phase-space integrated fit to  $B_s \rightarrow D_s K\pi\pi$  data in units of statistical standard deviations.

Fit Parameter	Fit bias	Acceptance	Resolution	$\Delta m_s$	Asymmetries	Background	Total
$C$	0.02	0.04	0.07	0.06	0.03	0.09	0.14
$D$	0.04	0.26	0.00	0.02	0.05	0.11	0.29
$\bar{D}$	0.05	0.26	0.01	0.02	0.05	0.16	0.32
$S$	0.01	0.02	0.03	0.24	0.03	0.15	0.29
$\bar{S}$	0.04	0.03	0.06	0.23	0.03	0.13	0.27

**Table 11.3:** Systematic uncertainties on the fit parameters of the full time-dependent amplitude fit to  $B_s \rightarrow D_s K\pi\pi$  data in units of statistical standard deviations.

Fit Parameter	Fit bias	Time-Acc.	Resolution	$\Delta m_s$	Asymmetries	Background	Lineshapes	Resonances $m, \Gamma$	Form-Factors	Phsp-Acc.	Amp. Model	Total
$B_s \rightarrow D_s(K_1(1270) \rightarrow K^*(892)\pi)$ Mag	0.04	0.17	0.01	0.01	0.02	0.15	1.30	0.28	0.42	0.06		1.42
$B_s \rightarrow D_s(K_1(1270) \rightarrow K^*(892)\pi)$ Phase	0.08	0.20	0.03	0.01	0.16	0.06	0.85	0.31	0.20	1.10		1.47
$B_s \rightarrow D_s(K_1(1270) \rightarrow K_0^*(1430)\pi)$ Mag	0.07	0.17	0.02	0.01	0.11	0.25	3.96	3.69	0.45	2.20		5.87
$B_s \rightarrow D_s(K_1(1270) \rightarrow K_0^*(1430)\pi)$ Phase	0.24	0.16	0.02	0.01	0.18	0.15	7.28	0.21	0.51	4.47		8.57
$B_s \rightarrow D_s(K_1(1400) \rightarrow K^*(892)\pi)$ Mag( $b \rightarrow c$ )	0.08	0.13	0.02	0.03	0.43	0.27	1.38	0.28	0.38	1.44		2.12
$B_s \rightarrow D_s(K_1(1400) \rightarrow K^*(892)\pi)$ Phase( $b \rightarrow c$ )	0.07	0.24	0.01	0.03	0.13	0.28	0.66	0.25	0.32	0.69		1.11
$B_s \rightarrow D_s(K_1(1400) \rightarrow K^*(892)\pi)$ Mag( $b \rightarrow u$ )	0.21	0.19	0.02	0.04	0.06	0.19	0.83	0.24	0.56	2.27		2.52
$B_s \rightarrow D_s(K_1(1400) \rightarrow K^*(892)\pi)$ Phase( $b \rightarrow u$ )	0.01	0.16	0.04	0.10	0.15	0.36	0.79	0.43	0.25	0.88		1.36
$B_s \rightarrow D_s(K^*(1410) \rightarrow K^*(892)\pi)$ Mag( $b \rightarrow c$ )	0.32	0.13	0.03	0.05	0.19	0.18	1.08	0.28	1.60	0.09		2.00
$B_s \rightarrow D_s(K^*(1410) \rightarrow K^*(892)\pi)$ Phase( $b \rightarrow c$ )	0.25	0.23	0.01	0.01	0.21	0.10	1.42	0.22	0.75	0.62		1.79
$B_s \rightarrow D_s(K^*(1410) \rightarrow K\rho(770))$ Mag	0.49	0.20	0.01	0.01	0.12	0.17	0.60	0.18	0.19	0.15		0.88
$B_s \rightarrow D_s(K^*(1410) \rightarrow K\rho(770))$ Phase	0.23	0.22	0.01	0.01	0.10	0.13	0.34	0.12	0.29	1.22		1.35
$B_s \rightarrow D_s(K(1460) \rightarrow K^*(892)\pi)$ Mag( $b \rightarrow u$ )	0.03	0.24	0.02	0.04	0.23	0.22	0.68	0.76	5.39	1.96		5.84
$B_s \rightarrow D_s(K(1460) \rightarrow K^*(892)\pi)$ Phase( $b \rightarrow u$ )	0.02	0.30	0.03	0.04	0.13	0.21	0.64	0.40	0.48	0.55		1.12
$B_s \rightarrow (D_s\pi)_P K^*(892)$ Mag( $b \rightarrow c$ )	0.15	0.16	0.02	0.02	0.35	0.24	1.28	0.20	2.66	0.99		3.16
$B_s \rightarrow (D_s\pi)_P K^*(892)$ Phase( $b \rightarrow c$ )	0.01	0.20	0.01	0.01	0.20	0.47	0.95	0.18	0.34	0.59		1.30
$B_s \rightarrow (D_s\pi)_P K^*(892)$ Mag( $b \rightarrow u$ )	0.15	0.14	0.04	0.03	0.37	0.13	0.47	0.27	1.73	0.68		1.99
$B_s \rightarrow (D_s\pi)_P K^*(892)$ Phase( $b \rightarrow u$ )	0.01	0.26	0.05	0.03	0.88	0.28	0.56	0.21	0.42	0.10		1.21
$B_s \rightarrow (D_sK)_P \rho(770)$ Mag( $b \rightarrow u$ )	0.45	0.24	0.01	0.05	0.83	0.49	1.34	0.38	2.81	0.33		3.34
$B_s \rightarrow (D_sK)_P \rho(770)$ Phase( $b \rightarrow u$ )	0.31	0.31	0.02	0.03	0.24	0.66	0.25	0.60	0.71	1.37		1.87
$m_{K_1(1400)}$	0.04	0.18	0.02	0.01	0.36	0.17	1.15	0.16	0.33	0.66		2.41
$\Gamma_{K_1(1400)}$	0.05	0.22	0.02	0.01	0.29	0.13	1.23	0.12	0.25	0.46		1.31
$m_{K^*(1410)}$	0.08	0.19	0.01	0.01	0.51	0.11	1.69	0.27	1.63	0.51		2.22
$\Gamma_{K^*(1410)}$	0.30	0.17	0.01	0.01	0.10	0.18	1.17	0.59	1.71	0.15		2.25
$r$	0.07	0.19	0.05	0.10	0.38	0.29	1.02	0.20	0.18	0.58		1.64
$\delta$	0.02	0.17	0.04	0.06	0.03	0.10	0.24	0.07	0.14	0.23		0.60
$\gamma - 2\beta_s$	0.01	0.11	0.05	0.07	0.28	0.25	0.30	0.29	0.06	0.42		0.82
										0.39		

## 1000 A Stripping and Trigger cuts

1001 The following text describes variables which are used in Table 1.1 and might be ambiguous,  
 1002 or which benefits are not straight forward. Where noted, different cut values are applied  
 1003 for Run-I and Run-II data. In Table 1.1, DOCA is the abbreviation for distance of closest  
 1004 approach. This variable is used to ensure that all  $D_s$  and  $X_{s,d}$  daughters originate from  
 1005 the same vertex. DIRA is the abbreviation for the cosine of the angle  $\theta$  between the  
 hadron's flight direction  $\vec{x}$  and it's corresponding momentum vector  $\vec{p}$ ,  $\cos \theta_{\vec{x}-\vec{p}}$ .

**Table 1.1:** Summary of the stripping selections for  $B_s^0 \rightarrow D_s K \pi \pi$  decays. The requirements for Run-II are only given if they have been changed.

Variable	Stripping Cut (Run-I)	Stripping Cut (Run-II)
Track $\chi^2/\text{nDoF}$	$< 3$	
Track $p$	$> 1000 \text{ MeV}/c$	
Track $p_T$	$> 100 \text{ MeV}/c$	
Track IP $\chi^2$	$> 4$	
Track ghost-prob.	$< 0.4$	
$D_s$ mass	$m_{D_s} \pm 100 \text{ MeV}$	$m_{D_s} \pm 80 \text{ MeV}$
$D_s$ Daughter $p_T$	$\sum_{i=1}^3 p_{t,i} > 1800 \text{ MeV}/c$	
$D_s$ Daughter DOCA	$< 0.5 \text{ mm}$	
$D_s$ Vertex $\chi^2/\text{nDoF}$	$< 10$	
$D_s$ $\chi^2$ -separation from PV	$> 36$	
$D_s$ daughter PID( $\pi$ )	$< 20$	
$D_s$ daughter PID(K)	$> -10$	
$X_{s,d}$ mass	$< 4000 \text{ MeV}$	$< 3500 \text{ MeV}$
$X_{s,d}$ Daughter $p$	$> 2 \text{ GeV}/c$	
$X_{s,d}$ Daughter DOCA	$< 0.4 \text{ mm}$	
$X_{s,d}$ Daughter $p_T$	$\sum_{i=1}^3 p_{t,i} > 1250 \text{ MeV}/c$	
$X_{s,d}$ Vertex $\chi^2/\text{nDoF}$	$< 8$	
$X_{s,d}$ $\chi^2$ -separation from PV	$> 16$	
$X_{s,d}$ DIRA	$> 0.98$	
$X_{s,d}$ $\Delta\rho$	$> 0.1 \text{ mm}$	
$X_{s,d}$ $\Delta z$	$> 2.0 \text{ mm}$	
$X_{s,d}$ daughter PID( $\pi$ )	$< 10$	
$X_s$ daughter PID(K)	$> -2$	$> 4$
$B_s^0$ mass	$[4750, 7000] \text{ MeV}/c^2$	$[5000, 6000] \text{ MeV}/c^2$
$B_s^0$ DIRA	$> 0.98$	$> 0.99994$
$B_s^0$ min IP $\chi^2$	$< 25$	$< 20$
$B_s^0$ Vertex $\chi^2/\text{nDoF}$	$< 10$	$< 8$
$B_s^0 \tau_{B_s^0}$	$> 0.2 \text{ ps}$	

1007 Table 1.2 summarizes the trigger requirements imposed by the Hlt1 line used in this  
1008 analysis for Run-I. At least one of the six decay particles must pass the listed requirements  
1009 in order for the event to be stored for further analysis. For Run-II, this trigger line was  
1010 updated and uses a multivariate classifier which takes the variables listed in Table 1.2 as  
1011 input, rather than directly cutting on them.

1012 The Hlt2 2, 3 and 4-body topological lines use a Boosted Decision Tree based on the  
1013 b-hadron  $p_T$ , its flight distance  $\chi^2$  from the nearest PV and the sum of the  $B_s^0$  and  $D_s$   
1014 vertex  $\chi^2$  divided by the sum of their number of degrees of freedom. Table 1.3 summarizes  
1015 the cuts applied by the inclusive  $\phi$  trigger, which requires that a  $\phi \rightarrow KK$  candidate can  
 be formed out of two tracks present in the event.

**Table 1.2:** Summary of the cuts applied by the Hlt1TrackAllL0 trigger for Run-I. At least one of the six decay particles must pass this requirements, in order for the event to be accepted.

Quantity	Hlt1TrackAllL0 requirement
Track IP [mm]	$> 0.1$
Track IP $\chi^2$	$> 16$
Track $\chi^2/\text{nDoF}$	$< 2.5$
Track $p_T$	$> 1.7 \text{ GeV}/c$
Track $p$	$> 10 \text{ GeV}/c$
Number VELO hits/track	$> 9$
Number missed VELO hits/track	$< 3$
Number OT+IT $\times 2$ hits/track	$> 16$

**Table 1.3:** Summary of the cuts applied by the Hlt2 inclusive  $\phi$  trigger. A  $\phi \rightarrow KK$  candidate, formed by two tracks in the event, must pass this requirements in order for the event to be accepted.

Quantity	Hlt2IncPhi requirement
$\phi$ mass	$m_\phi \pm 12 \text{ MeV}/c^2$ of PDG value
$\phi p_T$	$> 2.5 \text{ GeV}/c$
$\phi$ vertex $\chi^2/\text{nDoF}$	$< 20$
$\phi$ IP $\chi^2$ to any PV	$> 5$

1016

## B Details of multivariate classifier

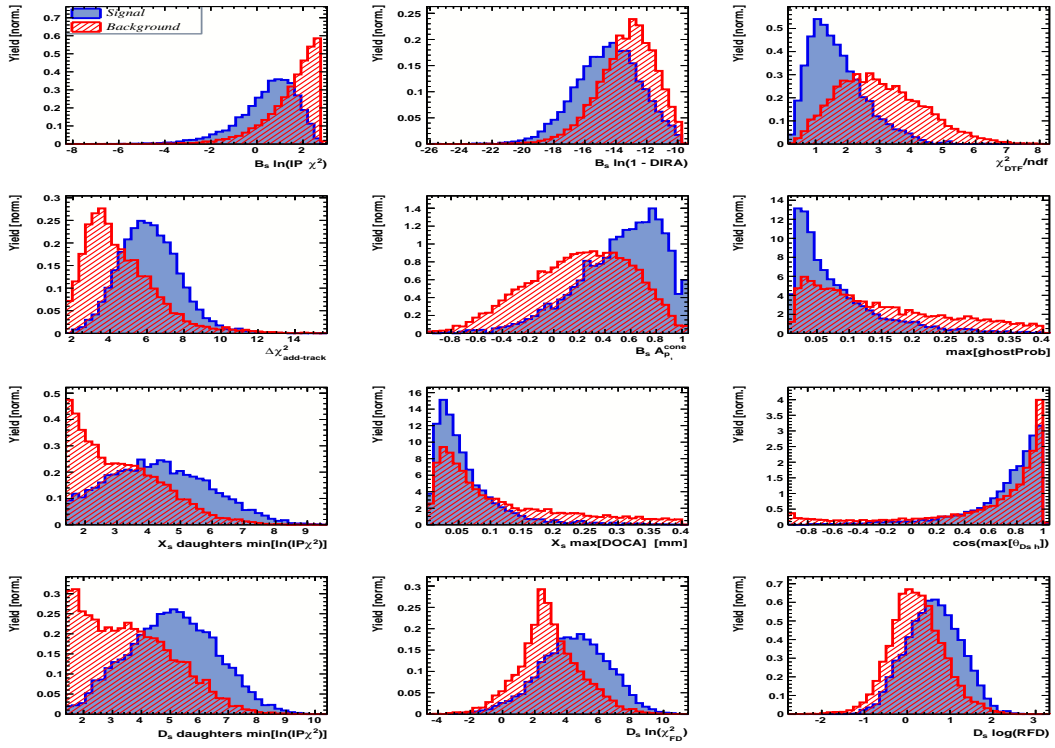


**Figure A.1:** Variables used to train the BDTG for category [Run-I,L0-TOS].

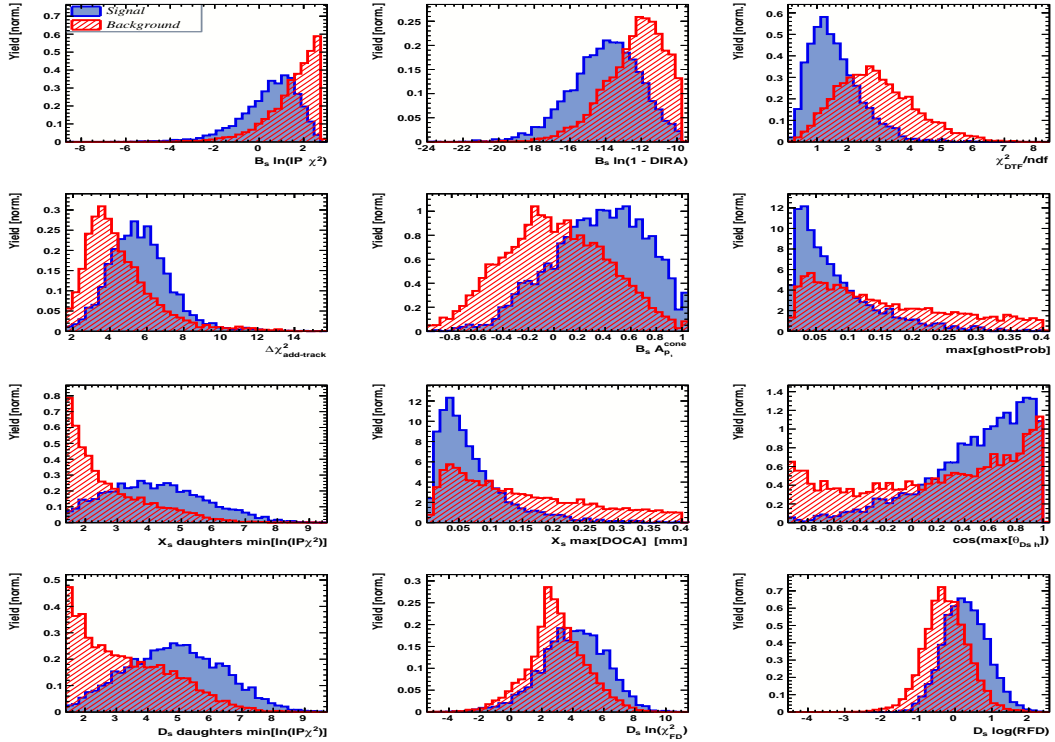


**Figure A.2:** Variables used to train the BDTG for category [Run-I,L0-TIS].

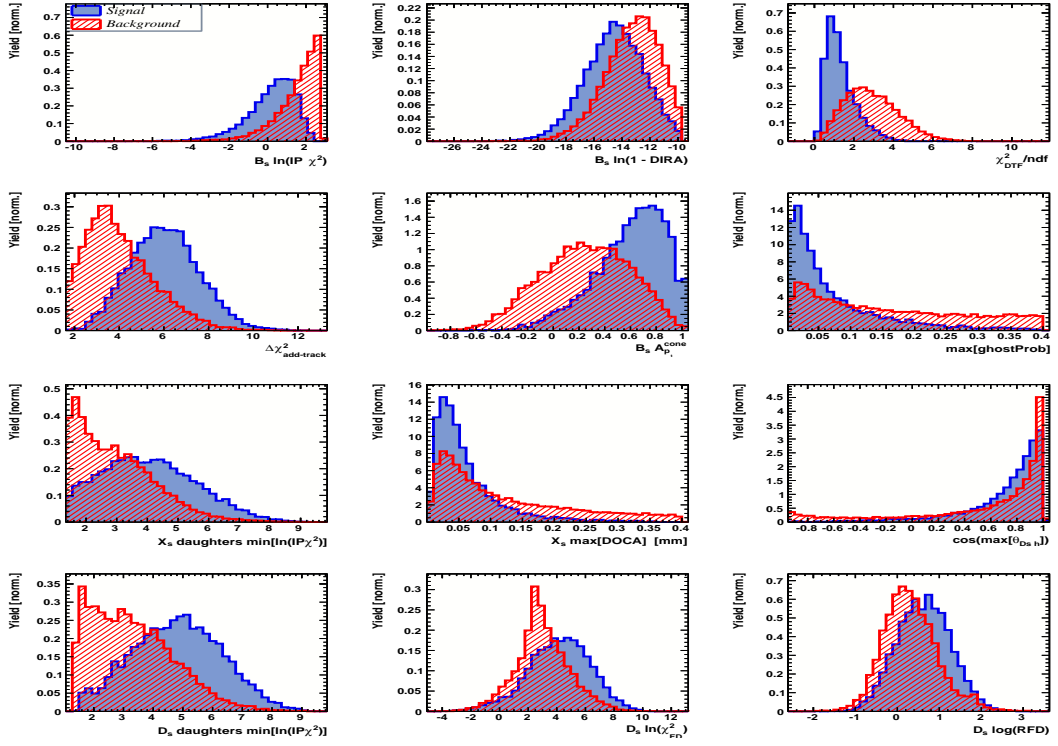


**Figure A.3:** Variables used to train the BDTG for category [Run-II,L0-TOS].

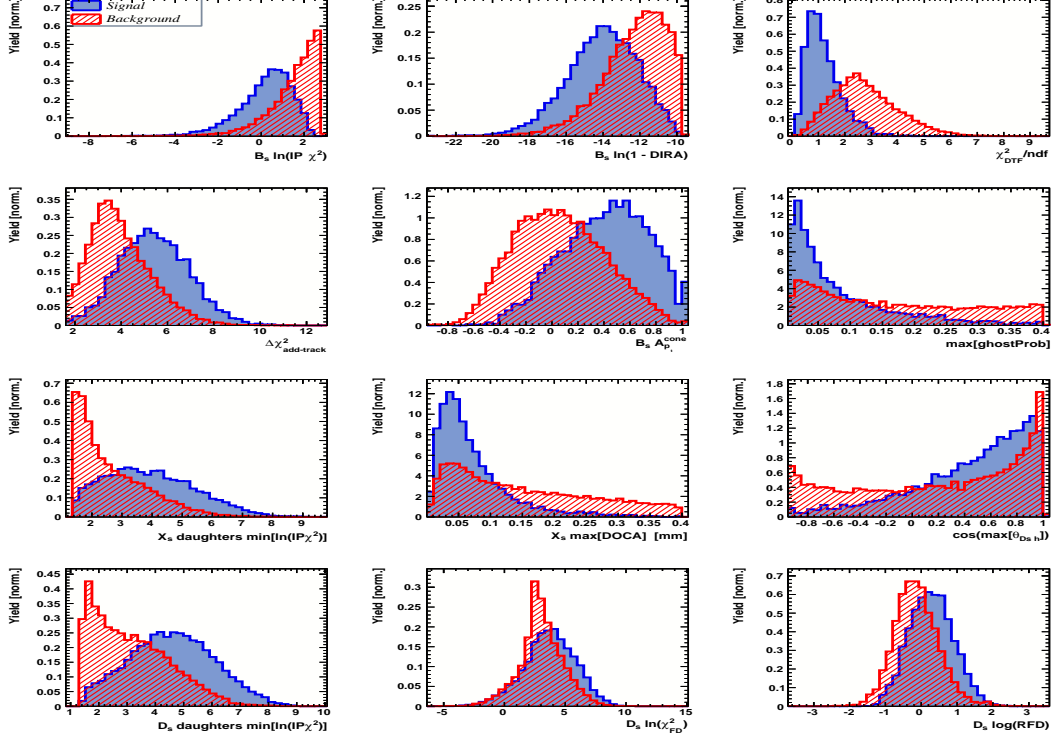


**Figure A.4:** Variables used to train the BDTG for category [Run-II,L0-TIS].

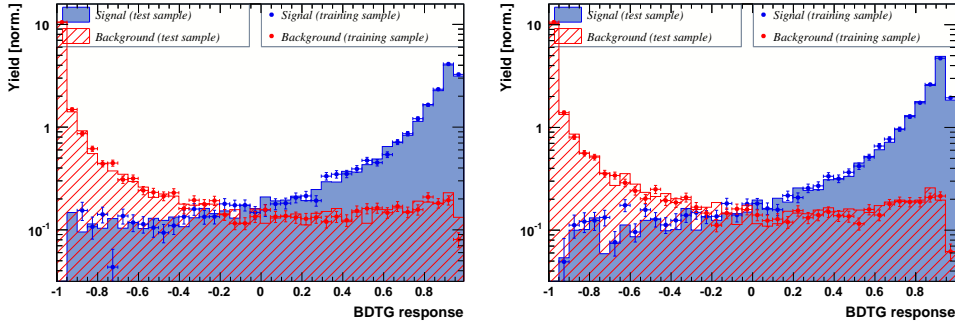


**Figure A.5:** Response of the classifier trained on the even and tested on the odd sample (left) and trained on the odd and tested on the even sample (right) for category [Run-I,L0-TOS].

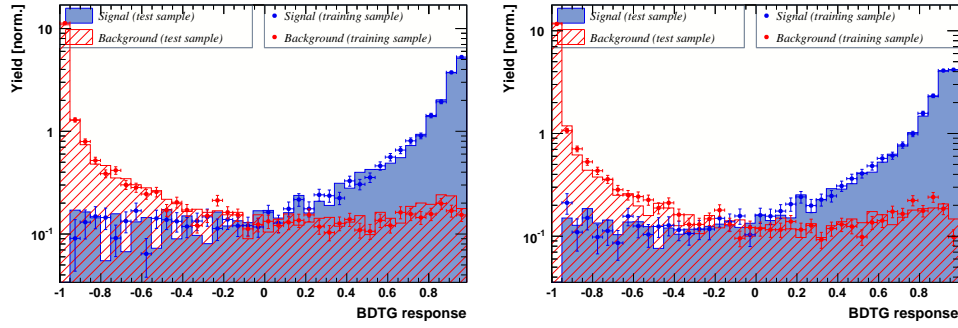


**Figure A.6:** Response of the classifier trained on the even and tested on the odd sample (left) and trained on the odd and tested on the even sample (right) for category [Run-I,L0-TIS].

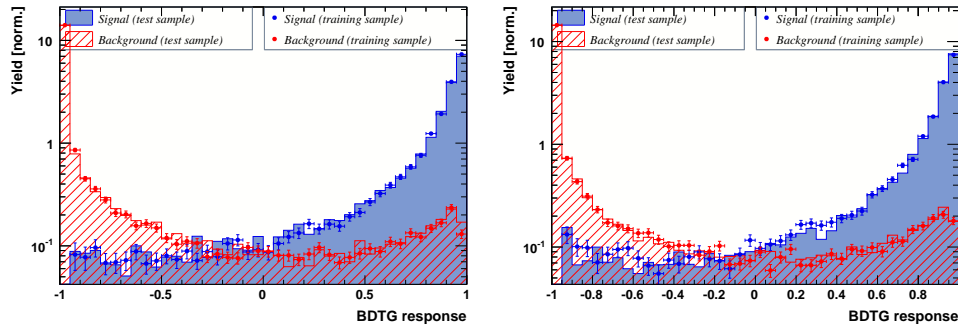


**Figure A.7:** Response of the classifier trained on the even and tested on the odd sample (left) and trained on the odd and tested on the even sample (right) for category [Run-II,L0-TOS].

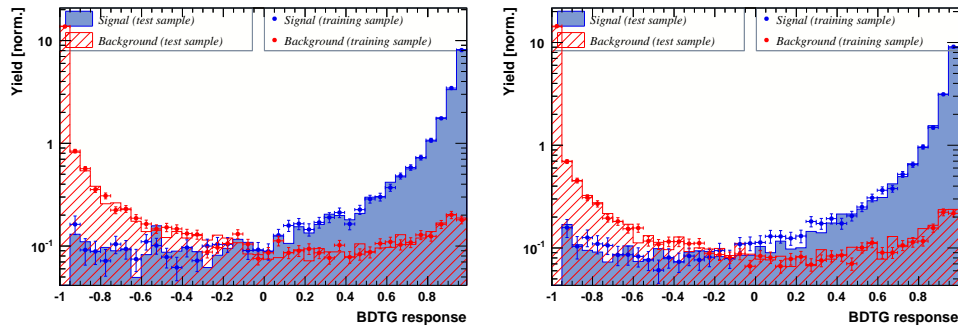


**Figure A.8:** Response of the classifier trained on the even and tested on the odd sample (left) and trained on the odd and tested on the even sample (right) for category [Run-II,L0-TIS].

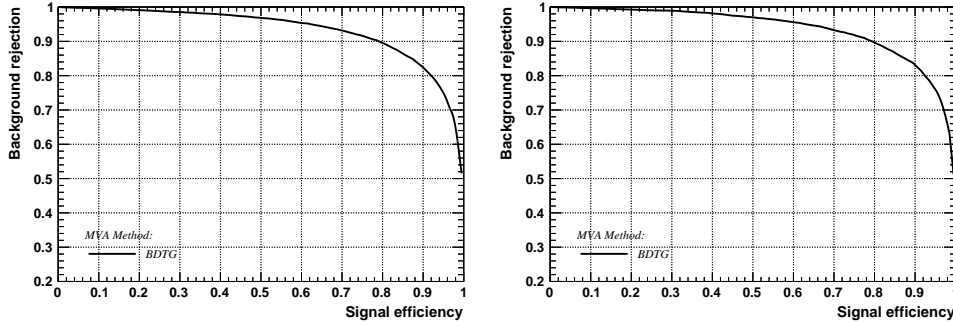


**Figure A.9:** Signal efficiency versus background rejection for the BDT trained on the even (left) and odd (right) sample for category [Run-I,L0-TOS].

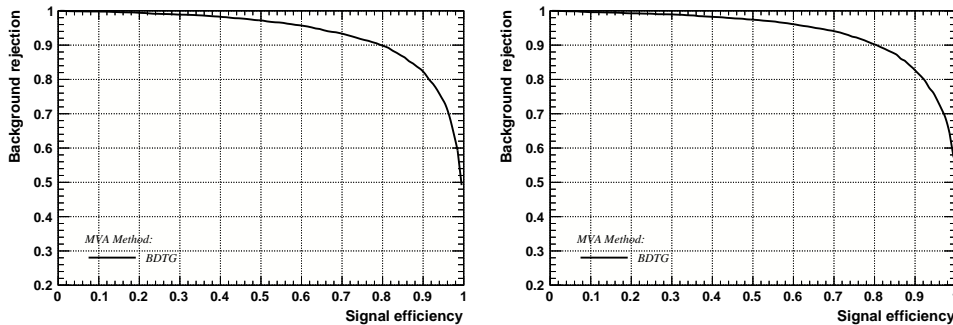


**Figure A.10:** Signal efficiency versus background rejection for the BDT trained on the even (left) and odd (right) sample for category [Run-I,L0-TIS].

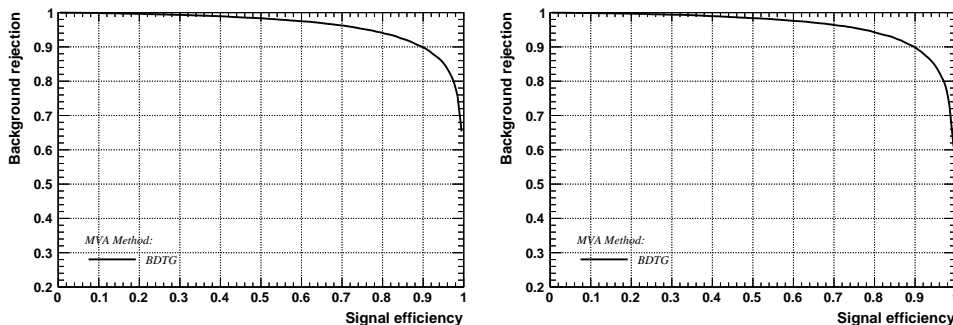


**Figure A.11:** Signal efficiency versus background rejection for the BDT trained on the even (left) and odd (right) sample for category [Run-II,L0-TOS].

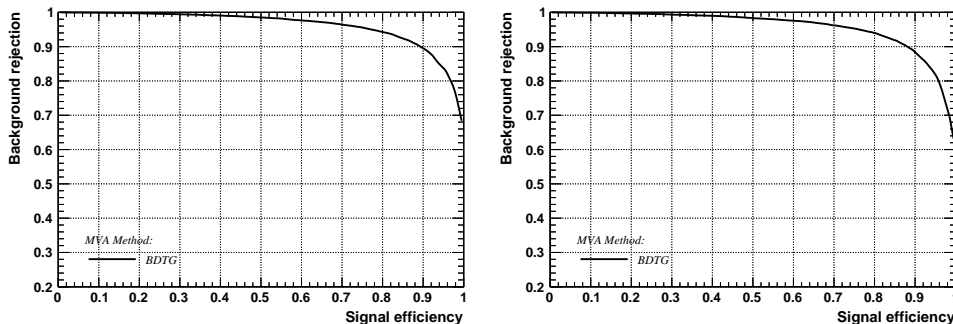


**Figure A.12:** Signal efficiency versus background rejection for the BDT trained on the even (left) and odd (right) sample for category [Run-II,L0-TIS].

## 1018 C Detailed mass fits

1019 In this section, all fits to the mass distribution of  $B_s^0 \rightarrow D_s\pi\pi\pi$  and  $B_s^0 \rightarrow D_sK\pi\pi$   
 1020 candidates are shown. The fits are performed simultaneously in run period (Run-I, Run-  
 1021 II),  $D_s$  final state ( $D_s \rightarrow KK\pi$  non-resonant,  $D_s \rightarrow \phi\pi$ ,  $D_s \rightarrow K^*K$ , or  $D_s \rightarrow \pi\pi\pi$ ) and  
 1022 L0 trigger category.

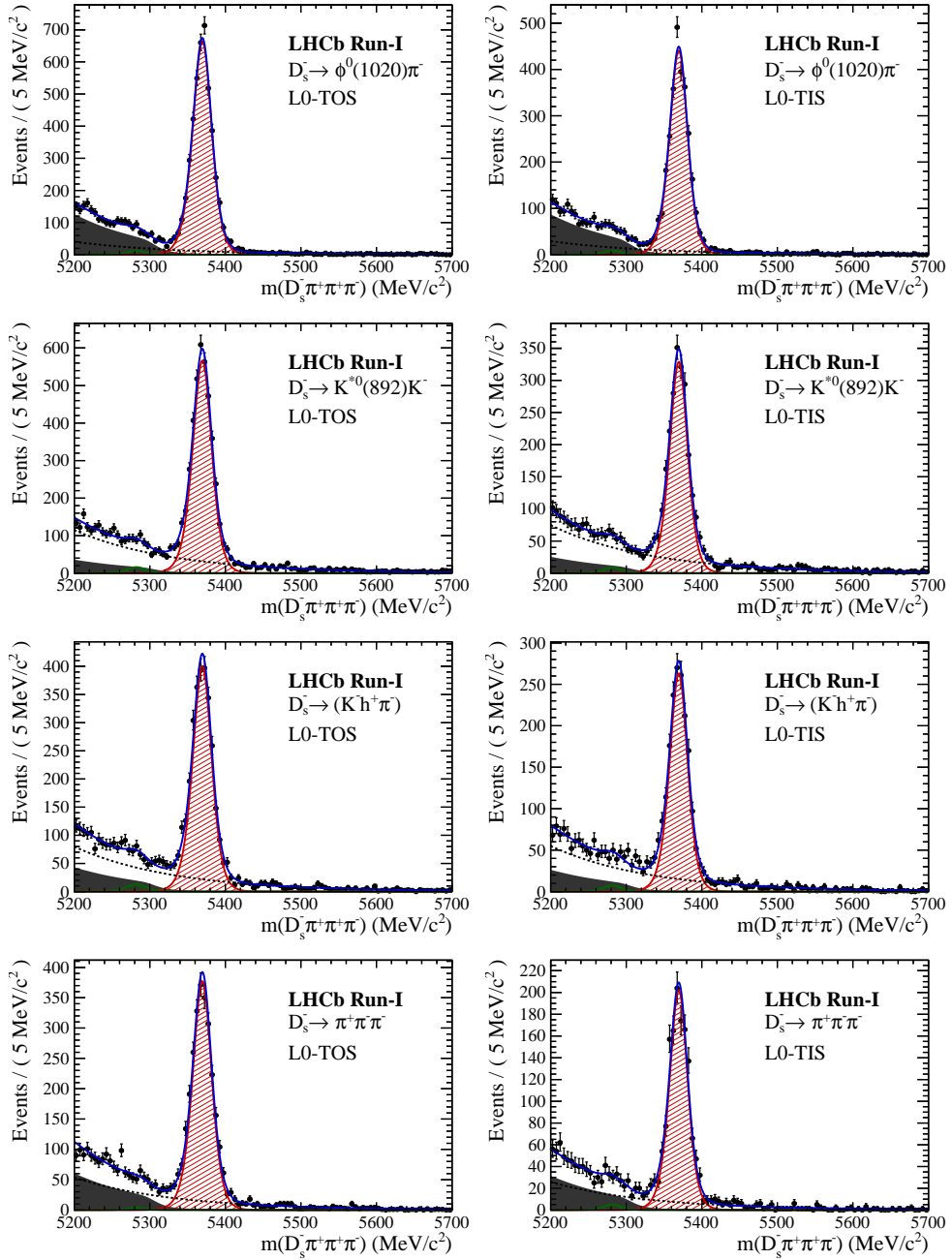
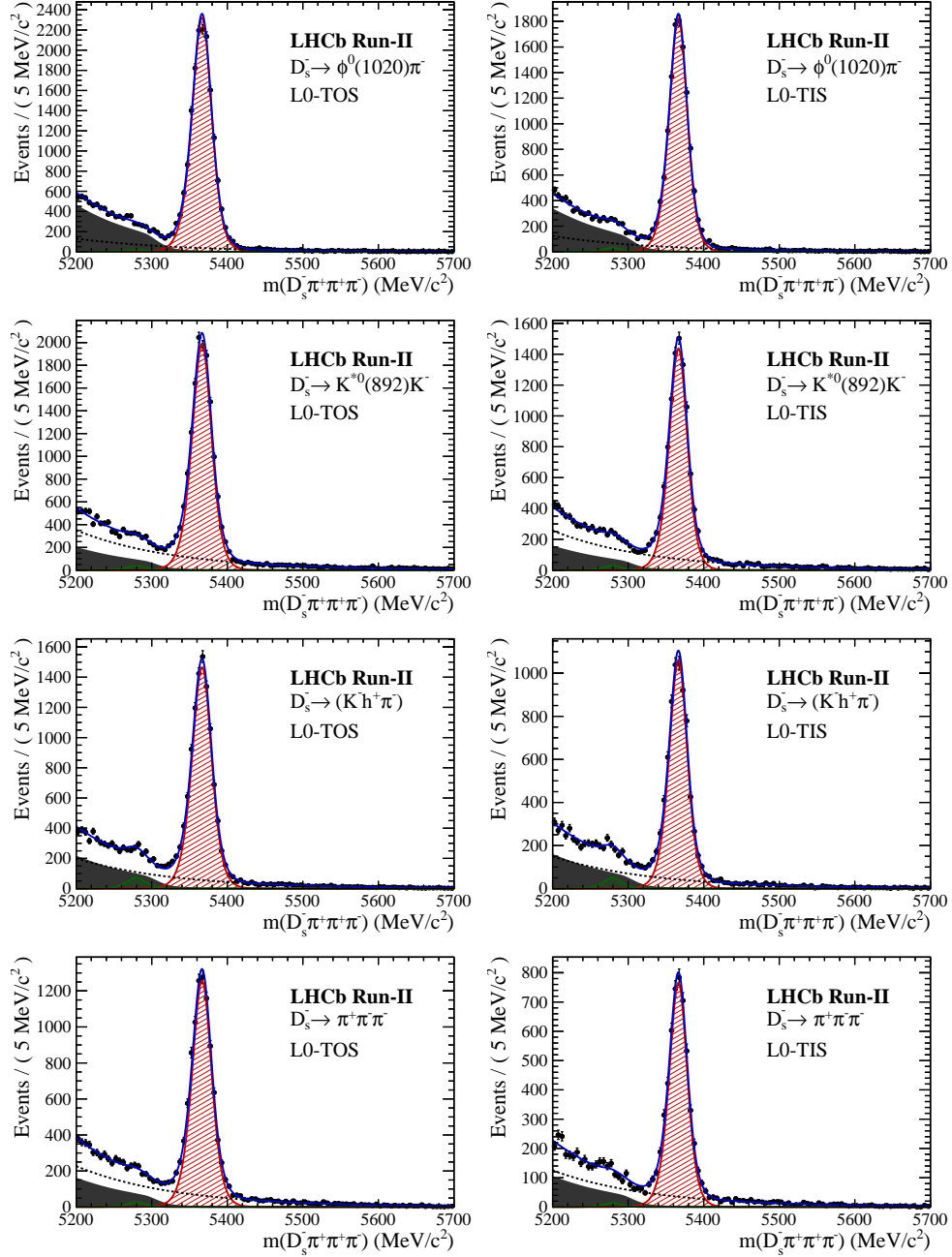
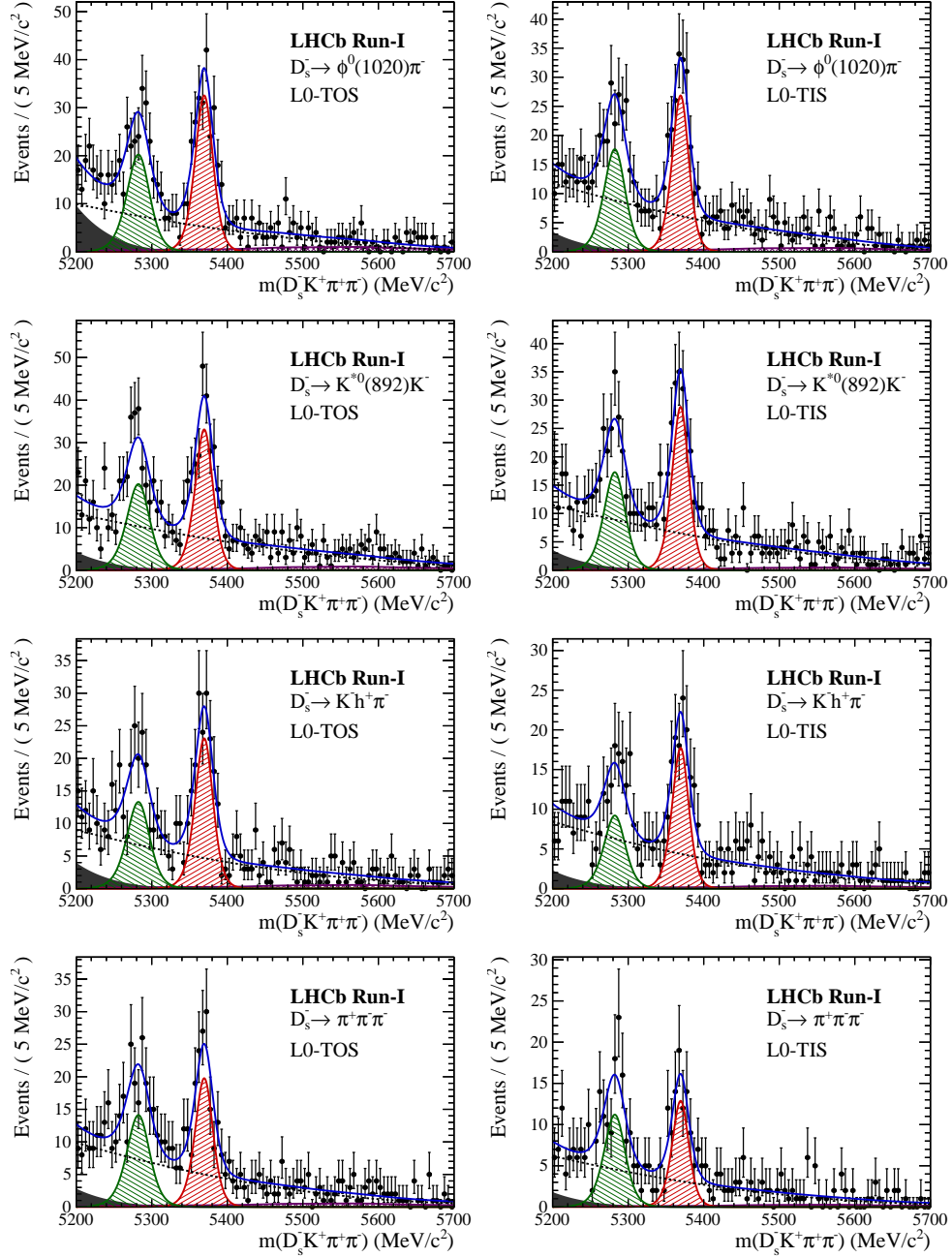


Figure B.1: Invariant mass distributions of  $B_s^0 \rightarrow D_s\pi\pi\pi$  candidates for Run-I data.



**Figure B.2:** Invariant mass distributions of  $B_s^0 \rightarrow D_s\pi\pi\pi$  candidates for Run-II data.



**Figure B.3:** Invariant mass distributions of  $B_s^0 \rightarrow D_s K \pi\pi$  candidates for Run-I data.

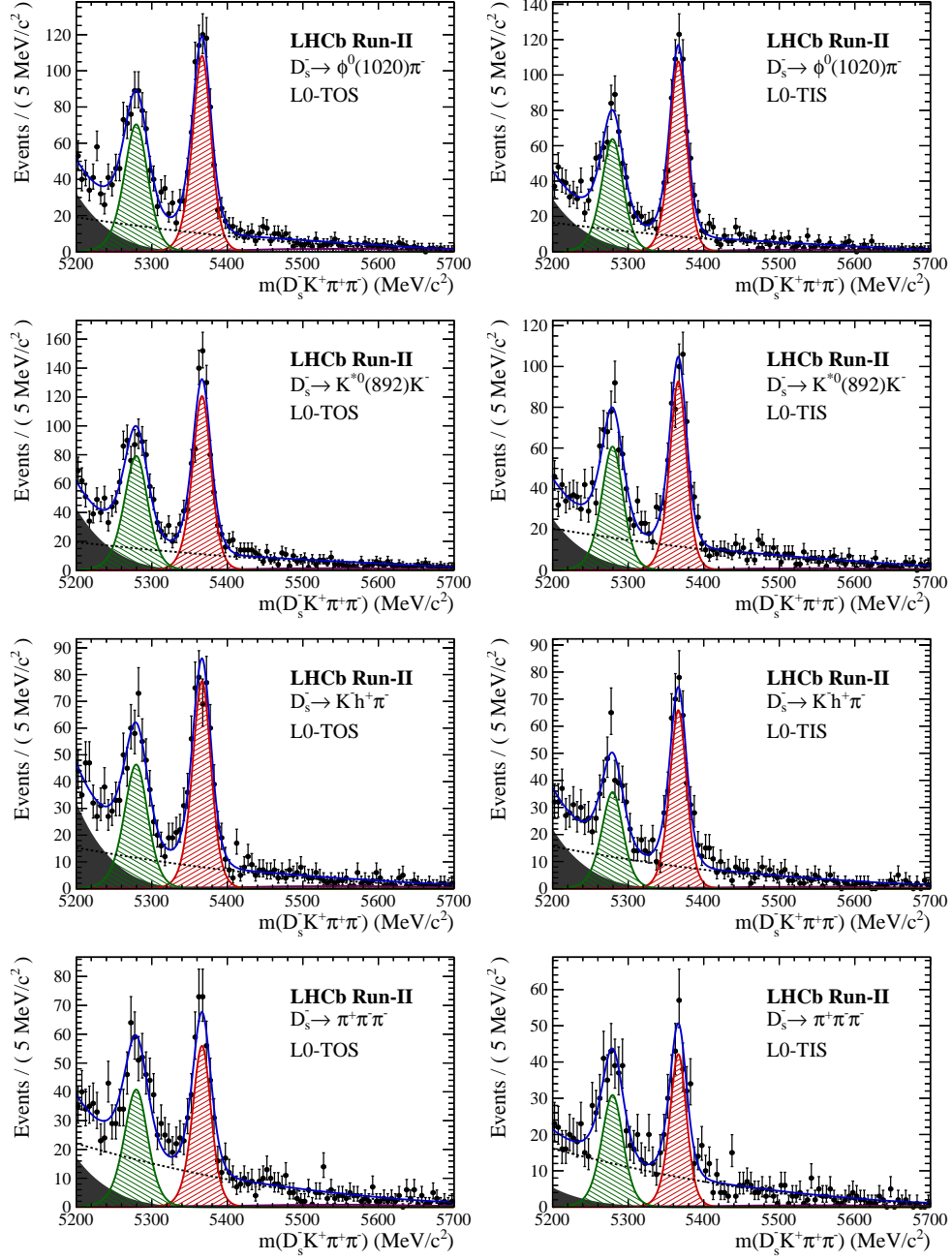


**Figure B.4:** Invariant mass distributions of  $B_s^0 \rightarrow D_s K \pi \pi$  candidates for Run-II data.

## 1023 D Decay-time Resolution fits

1024 This section contains all fits to the distributions of the decay time difference  $\Delta t$  between  
 1025 the true and the reconstructed decay time of the truth-matched  $B_s^0$  candidates on MC.  
 1026 The fits are performed in bins of the decay time error  $\sigma_t$ , where an adaptive binning  
 1027 scheme is used to ensure that approximately the same number of events are found in each  
 1028 bin.

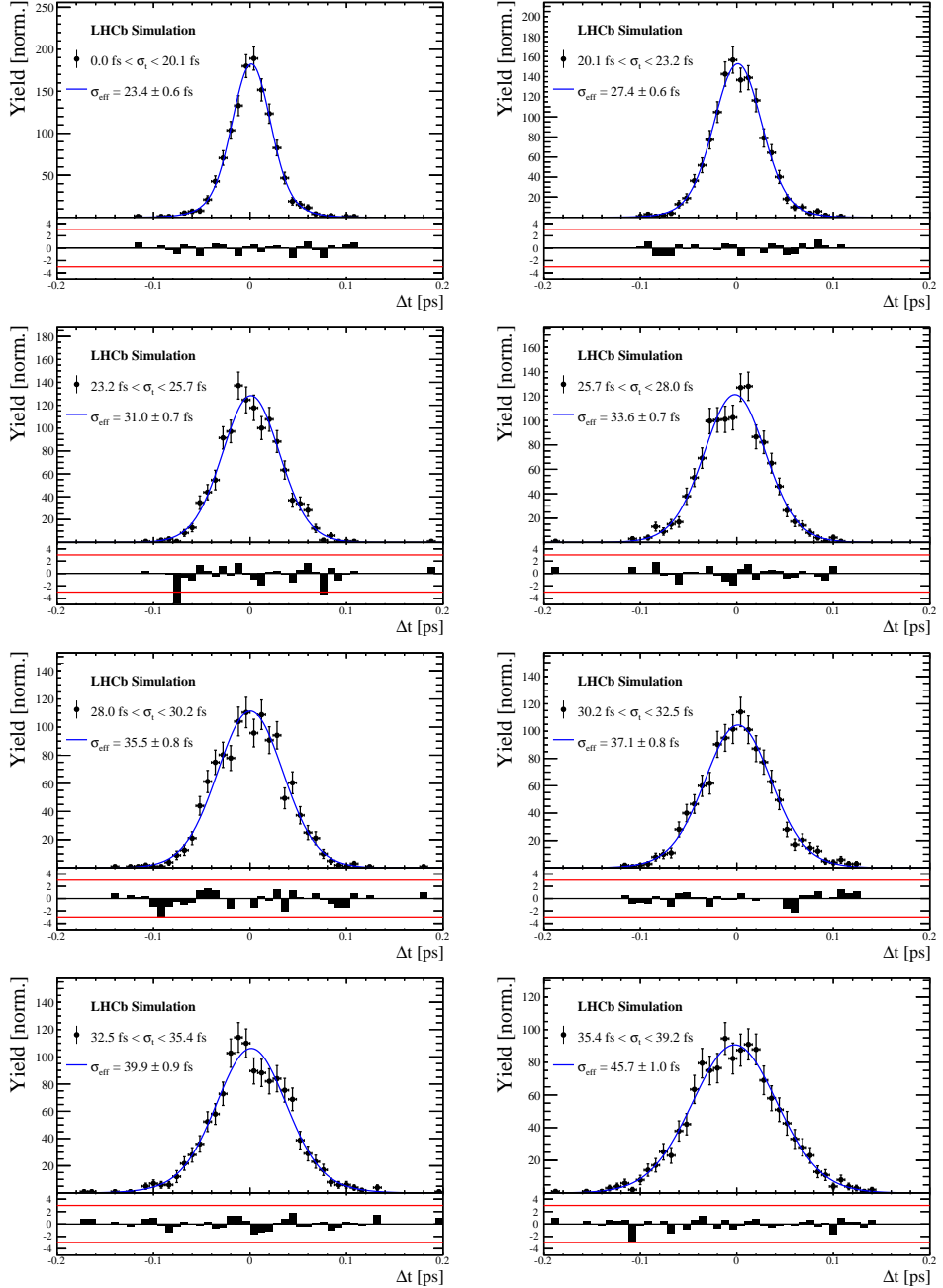


**Figure C.1:** Difference of the true and measured decay time of  $B_s^0 \rightarrow D_s K \pi \pi$  MC candidates in bins of the per-event decay time error estimate..

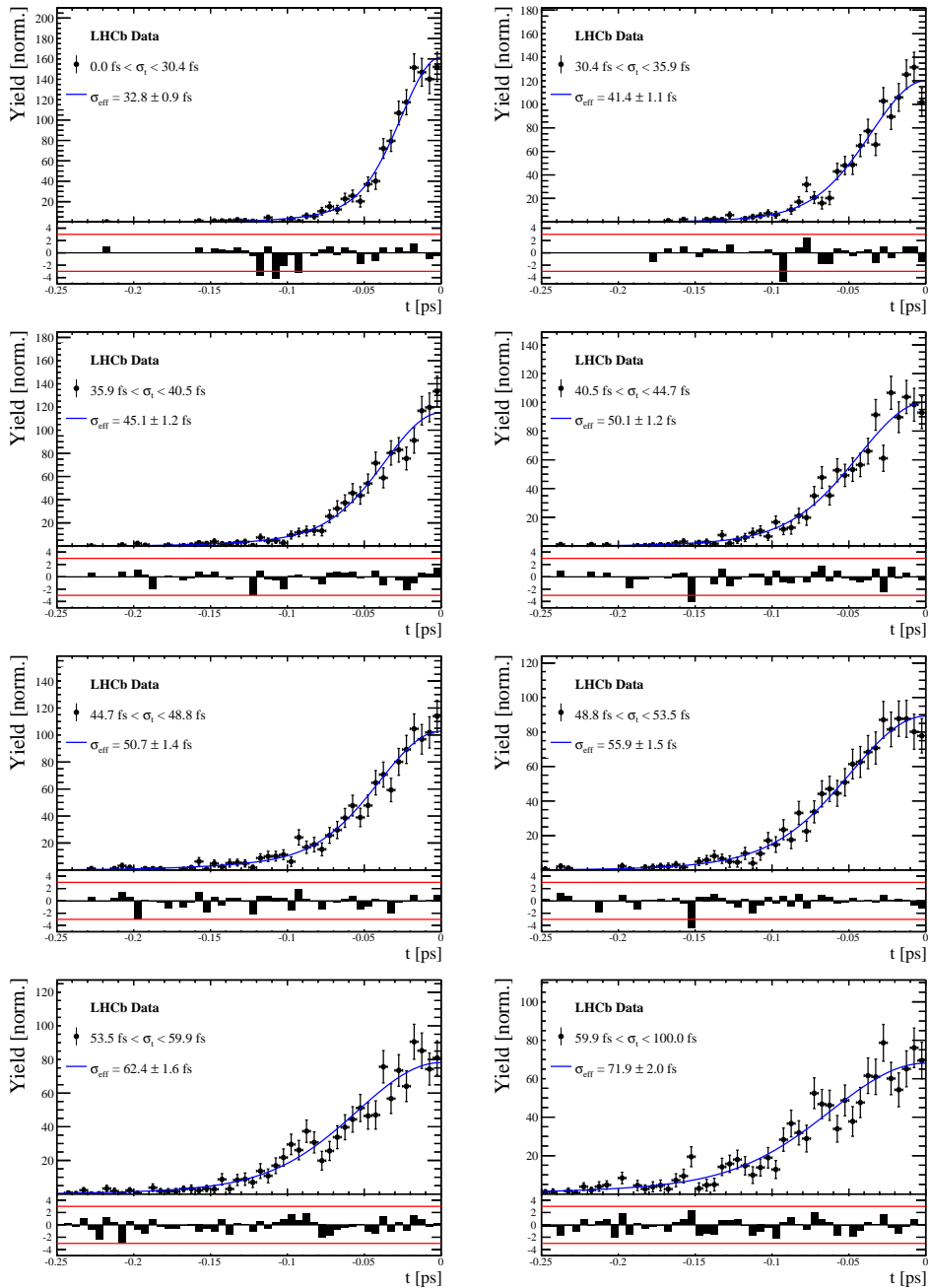


**Figure C.2:** Decay-time distribution for fake  $B_s$  candidates from promptly produced  $D_s$  candidates, combined with random prompt  $K\pi\pi$  bachelor tracks, for bins in the per-event decay time error estimate.

$\sigma_t$ Bin [fs]	$\sigma_1$ [fs]	$\sigma_2$ [fs]	$f_1$	D	$\sigma_{eff}$ [fs]
0.0 - 20.1	$19 \pm 0.675$	$33.8 \pm 1.77$	$0.75 \pm 0$	$0.917 \pm 0.00406$	$23.4 \pm 0.599$
20.1 - 23.2	$23.4 \pm 0.86$	$37.4 \pm 1.95$	$0.75 \pm 0$	$0.888 \pm 0.00477$	$27.4 \pm 0.621$
23.2 - 25.7	$28.1 \pm 1.02$	$38.7 \pm 2.32$	$0.75 \pm 0$	$0.86 \pm 0.00563$	$31 \pm 0.671$
25.7 - 28.0	$30.1 \pm 1.12$	$43.2 \pm 2.56$	$0.75 \pm 0$	$0.837 \pm 0.00651$	$33.6 \pm 0.734$
28.0 - 30.2	$32.4 \pm 1.12$	$44.2 \pm 2.59$	$0.75 \pm 0$	$0.819 \pm 0.00694$	$35.5 \pm 0.756$
30.2 - 32.5	$32.6 \pm 1.38$	$49.2 \pm 3.04$	$0.75 \pm 0$	$0.805 \pm 0.00792$	$37.1 \pm 0.841$
32.5 - 35.4	$34.4 \pm 1.19$	$54.7 \pm 2.85$	$0.75 \pm 0$	$0.778 \pm 0.0086$	$39.9 \pm 0.879$
35.4 - 39.2	$41.9 \pm 1.8$	$56.9 \pm 4.18$	$0.75 \pm 0$	$0.719 \pm 0.00997$	$45.7 \pm 0.962$
39.2 - 44.7	$42.2 \pm 1.56$	$68.1 \pm 4.01$	$0.75 \pm 0$	$0.687 \pm 0.0114$	$48.8 \pm 1.08$
44.7 - 120.0	$55.5 \pm 2.59$	$83 \pm 14.7$	$0.75 \pm 0$	$0.546 \pm 0.0521$	$62 \pm 4.89$

**Table 4.1:** Measured time resolution for  $B_s \rightarrow D_s K\pi\pi$  MC in bins of the per-event decay time error estimate.

$\sigma_t$ Bin [fs]	$\sigma_1$ [fs]	$\sigma_2$ [fs]	$f_1$	D	$\sigma_{eff}$ [fs]
0.0 - 30.4	$25.4 \pm 1.03$	$50.7 \pm 2.77$	$0.75 \pm 0$	$0.844 \pm 0.00822$	$32.8 \pm 0.942$
30.4 - 35.9	$34.5 \pm 1.46$	$60.2 \pm 3.48$	$0.75 \pm 0$	$0.763 \pm 0.0108$	$41.4 \pm 1.08$
35.9 - 40.5	$35.6 \pm 1.35$	$71.3 \pm 3.84$	$0.75 \pm 0$	$0.726 \pm 0.0121$	$45.1 \pm 1.18$
40.5 - 44.7	$42.3 \pm 1.65$	$73.3 \pm 4.21$	$0.75 \pm 0$	$0.673 \pm 0.0132$	$50.1 \pm 1.24$
44.7 - 48.8	$39.6 \pm 1.64$	$84.8 \pm 5.07$	$0.75 \pm 0$	$0.666 \pm 0.0145$	$50.7 \pm 1.36$
48.8 - 53.5	$47.6 \pm 1.94$	$82.4 \pm 5.48$	$0.75 \pm 0$	$0.611 \pm 0.0157$	$55.9 \pm 1.46$
53.5 - 59.9	$53 \pm 2.15$	$95.3 \pm 6.84$	$0.75 \pm 0$	$0.541 \pm 0.0174$	$62.4 \pm 1.63$
59.9 - 100.0	$60.5 \pm 2.8$	$125 \pm 14$	$0.75 \pm 0$	$0.443 \pm 0.0204$	$71.9 \pm 2.03$

**Table 4.2:** Measured time resolution for prompt- $D_s$  data in bins of the per-event decay time error estimate.

## 1029 E Comparison of time-acceptance in subsamples

1030 Figure C.1 shows the spline coefficients obtained by fitting the decay-time distribution of  
 1031  $B_s^0 \rightarrow D_s\pi\pi\pi$  data candidates in different subsamples. Sufficient agreement is observed  
 1032 within a given data-taking period, while the acceptance shapes for Run-I and Run-II  
 1033 data differ significantly. The fitted splines for the different  $D_s$  final states are in a good  
 1034 agreement. The largest deviations are observed between the different L0 categories.

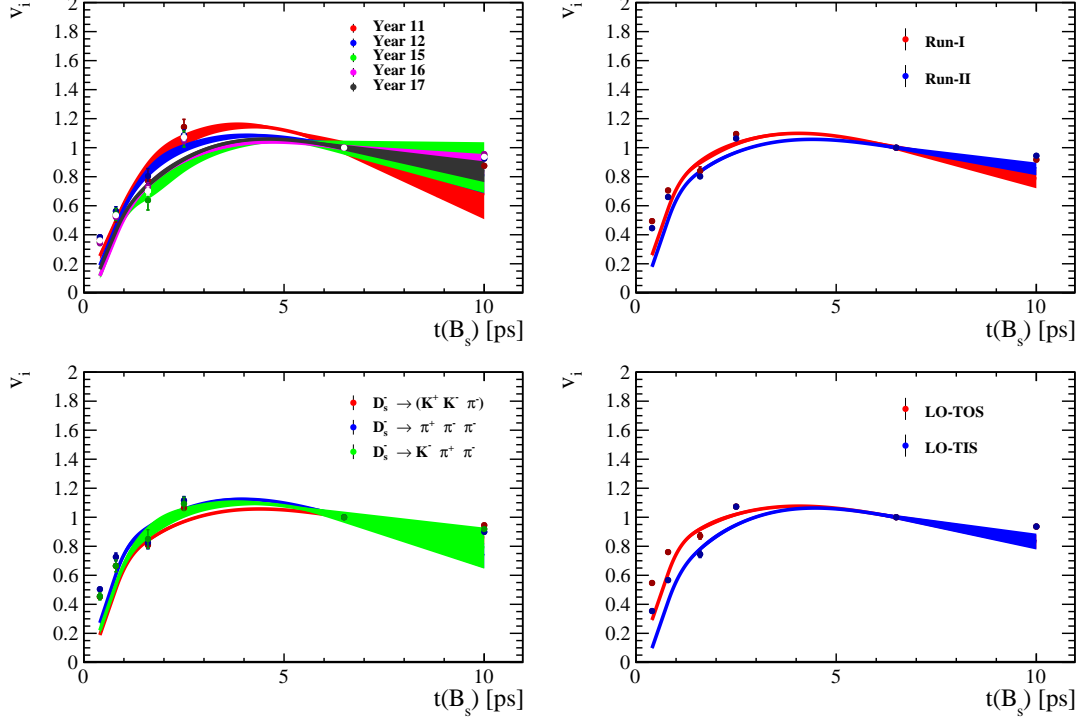


**Figure C.1:** Comparison of the spline coefficients (point with error bars) obtained from time-dependent fits to the  $B_s^0 \rightarrow D_s\pi\pi\pi$  decay-time for different subsamples: (top-left) different years of data-taking; (top-right) different data-taking periods; (bottom-left) different  $D_s$  final states; (bottom-right) different trigger categories. The interpolated splines are overlaid.

1035 **F Spin Amplitudes**

1036 The spin factors used for  $B \rightarrow P_1 P_2 P_3 P_4$  decays are given in Table 6.1.

**Table 6.1:** Spin factors for all topologies considered in this analysis. In the decay chains,  $S$ ,  $P$ ,  $V$ ,  $A$ ,  $T$  and  $PT$  stand for scalar, pseudoscalar, vector, axial vector, tensor and pseudotensor, respectively. If no angular momentum is specified, the lowest angular momentum state compatible with angular momentum conservation and, where appropriate, parity conservation, is used.

Number	Decay chain	Spin amplitude
1	$B \rightarrow (P P_1)$ , $P \rightarrow (S P_2)$ , $S \rightarrow (P_3 P_4)$	1
2	$B \rightarrow (P P_1)$ , $P \rightarrow (V P_2)$ , $V \rightarrow (P_3 P_4)$	$L_{(1)\alpha}(P) L_{(1)}^\alpha(V)$
3	$B \rightarrow (A P_1)$ , $A \rightarrow (V P_2)$ , $V \rightarrow (P_3 P_4)$	$L_{(1)\alpha}(B) P_{(1)}^{\alpha\beta}(A) L_{(1)\beta}(V)$
4	$B \rightarrow (A P_1)$ , $A[D] \rightarrow (P_2 V)$ , $V \rightarrow (P_3 P_4)$	$L_{(1)\alpha}(B) L_{(2)}^{\alpha\beta}(A) L_{(1)\beta}(V)$
5	$B \rightarrow (A P_1)$ , $A \rightarrow (S P_2)$ , $S \rightarrow (P_3 P_4)$	$L_{(1)\alpha}(B) L_{(1)}^\alpha(A)$
6	$B \rightarrow (A P_1)$ , $A \rightarrow (T P_2)$ , $T \rightarrow (P_3 P_4)$	$L_{(1)\alpha}(B) L_{(1)\beta}(A) L_{(2)}^{\alpha\beta}(T)$
7	$B \rightarrow (V_1 P_1)$ , $V_1 \rightarrow (V_2 P_2)$ , $V_2 \rightarrow (P_3 P_4)$	$L_{(1)\mu}(B) P_{(1)}^{\mu\alpha}(V_1) \epsilon_{\alpha\beta\gamma\delta} L_{(1)}^\beta(V_1) p_{V_1}^\gamma L_{(1)}^\delta(V_2)$
8	$B \rightarrow (PT P_1)$ , $PT \rightarrow (V P_2)$ , $V \rightarrow (P_3 P_4)$	$L_{(2)\alpha\beta}(B) P_{(2)}^{\alpha\beta\gamma\delta}(PT) L_{(1)\gamma}(PT) L_{(1)\delta}(V)$
9	$B \rightarrow (PT P_1)$ , $PT \rightarrow (S P_2)$ , $S \rightarrow (P_3 P_4)$	$L_{(2)\alpha\beta}(B) L_{(2)}(PT)^{\alpha\beta}$
10	$B \rightarrow (PT P_1)$ , $PT \rightarrow (T P_2)$ , $T \rightarrow (P_3 P_4)$	$L_{(2)\alpha\beta}(B) P_{(2)}^{\alpha\beta\gamma\delta}(PT) L_{(2)\gamma\delta}(T)$
11	$B \rightarrow (T P_1)$ , $T \rightarrow (V P_2)$ , $V \rightarrow (P_3 P_4)$	$L_{(2)\mu\nu}(B) P_{(2)}^{\mu\nu\rho\alpha}(T) \epsilon_{\alpha\beta\gamma\delta} L_{(2)\rho}^\beta(T) p_T^\gamma P_{(1)}^{\delta\sigma}(T) L_{(1)\sigma}(V)$
12	$B \rightarrow (T_1 P_1)$ , $T_1 \rightarrow (T_2 P_2)$ , $T_2 \rightarrow (P_3 P_4)$	$L_{(2)\mu\nu}(B) P_{(2)}^{\mu\nu\rho\alpha}(T_1) \epsilon_{\alpha\beta\gamma\delta} L_{(1)}^\beta(T_1) p_{T_1}^\gamma L_{(2)\rho}^\delta(T_2)$
13	$B \rightarrow (S_1 S_2)$ , $S_1 \rightarrow (P_1 P_2)$ , $S_2 \rightarrow (P_3 P_4)$	1
14	$B \rightarrow (V S)$ , $V \rightarrow (P_1 P_2)$ , $S \rightarrow (P_3 P_4)$	$L_{(1)\alpha}(B) L_{(1)}^\alpha(V)$
15	$B \rightarrow (V_1 V_2)$ , $V_1 \rightarrow (P_1 P_2)$ , $V_2 \rightarrow (P_3 P_4)$	$L_{(1)\alpha}(V_1) L_{(1)}^\alpha(V_2)$
16	$B[P] \rightarrow (V_1 V_2)$ , $V_1 \rightarrow (P_1 P_2)$ , $V_2 \rightarrow (P_3 P_4)$	$\epsilon_{\alpha\beta\gamma\delta} L_{(1)}^\alpha(B) L_{(1)}^\beta(V_1) L_{(1)}^\gamma(V_2) p_B^\delta$
17	$B[D] \rightarrow (V_1 V_2)$ , $V_1 \rightarrow (P_1 P_2)$ , $V_2 \rightarrow (P_3 P_4)$	$L_{(2)\alpha\beta}(B) L_{(1)}^\alpha(V_1) L_{(1)}^\beta(V_2)$
18	$B \rightarrow (T S)$ , $T \rightarrow (P_1 P_2)$ , $S \rightarrow (P_3 P_4)$	$L_{(2)\alpha\beta}(B) L_{(2)}^{\alpha\beta}(T)$
19	$B \rightarrow (V T)$ , $T \rightarrow (P_1 P_2)$ , $V \rightarrow (P_3 P_4)$	$L_{(1)\alpha}(B) L_{(2)}^{\alpha\beta}(T) L_{(1)\beta}(V)$
20	$B[D] \rightarrow (TV)$ , $T \rightarrow (P_1 P_2)$ , $V \rightarrow (P_3 P_4)$	$\epsilon_{\alpha\beta\delta\gamma} L_2^{\alpha\mu}(B) L_{2\mu}^\beta L_{(1)}^\gamma(V) p_B^\delta$
21	$B \rightarrow (T_1 T_2)$ , $T_1 \rightarrow (P_1 P_2)$ , $T_2 \rightarrow (P_3 P_4)$	$L_{(2)\alpha\beta}(T_1) L_{(2)}^{\alpha\beta}(T_2)$
22	$B[P] \rightarrow (T_1 T_2)$ , $T_1 \rightarrow (P_1 P_2)$ , $T_2 \rightarrow (P_3 P_4)$	$\epsilon_{\alpha\beta\gamma\delta} L_{(1)}^\alpha(B) L_{(2)}^{\beta\mu}(T_1) L_{(2)\mu}^\gamma(T_2) p_B^\delta$
23	$B[D] \rightarrow (T_1 T_2)$ , $T_1 \rightarrow (P_1 P_2)$ , $T_2 \rightarrow (P_3 P_4)$	$L_{(2)\alpha\beta}(B) L_{(2)}^{\alpha\gamma}(T_1) L_{(2)\gamma}^\beta(T_2)$

## 1037 G Considered Decay Chains

1038 The various decay channels considered in the model building are listed in Table 7.1.

**Table 7.1:** Decays considered in the LASSO model building.

Decay channel
$B_s \rightarrow D_s^- [K_1(1270)^+ [S, D] \rightarrow \pi^+ K^*(892)^0]$
$B_s \rightarrow D_s^- [K_1(1270)^+ \rightarrow \pi^+ K^*(1430)^0]$
$B_s \rightarrow D_s^- [K_1(1270)^+ [S, D] \rightarrow K^+ \rho(770)^0]$
$B_s \rightarrow D_s^- [K_1(1270)^+ [S, D] \rightarrow K^+ \omega(782)]$
$B_s \rightarrow D_s^- [K_1(1400)^+ [S, D] \rightarrow \pi^+ K^*(892)^0]$
$B_s \rightarrow D_s^- [K_1(1400)^+ [S, D] \rightarrow K^+ \rho(770)^0]$
$B_s \rightarrow D_s^- [K(1460)^+ \rightarrow \pi^+ \kappa]$
$B_s \rightarrow D_s^- [K(1460)^+ \rightarrow K^+ \sigma]$
$B_s \rightarrow D_s^- [K(1460)^+ \rightarrow \pi^+ K^*(892)^0]$
$B_s \rightarrow D_s^- [K(1460)^+ \rightarrow K^+ \rho(770)^0]$
$B_s \rightarrow D_s^- [K^*(1410)^+ \rightarrow \pi^+ K^*(892)^0]$
$B_s \rightarrow D_s^- [K^*(1410)^+ \rightarrow K^+ \rho(770)^0]$
$B_s \rightarrow D_s^- [K_2^*(1430)^+ \rightarrow \pi^+ K^*(892)^0]$
$B_s \rightarrow D_s^- [K_2^*(1430)^+ \rightarrow K^+ \rho(770)^0]$
$B_s \rightarrow D_s^- [K^*(1680)^+ \rightarrow \pi^+ K^*(892)^0]$
$B_s \rightarrow D_s^- [K^*(1680)^+ \rightarrow K^+ \rho(770)^0]$
$B_s \rightarrow D_s^- [K_2(1770)^+ \rightarrow \pi^+ K^*(892)^0]$
$B_s \rightarrow D_s^- [K_2(1770)^+ \rightarrow K^+ \rho(770)^0]$
$B_s \rightarrow \sigma^0(D_s^- K^+)_S$
$B_s [S, P, D] \rightarrow \sigma^0(D_s^- K^+)_V$
$B_s \rightarrow \rho(770)^0(D_s^- K^+)_S$
$B_s [S, P, D] \rightarrow \rho(770)^0(D_s^- K^+)_V$
$B_s \rightarrow K^*(892)^0(D_s^- \pi^+)_S$
$B_s [S, P, D] \rightarrow K^*(892)^0(D_s^- \pi^+)_V$
$B_s \rightarrow (D_s^- K^+)_S (\pi^+ \pi^-)_S$

## H Data-simulation comparisson

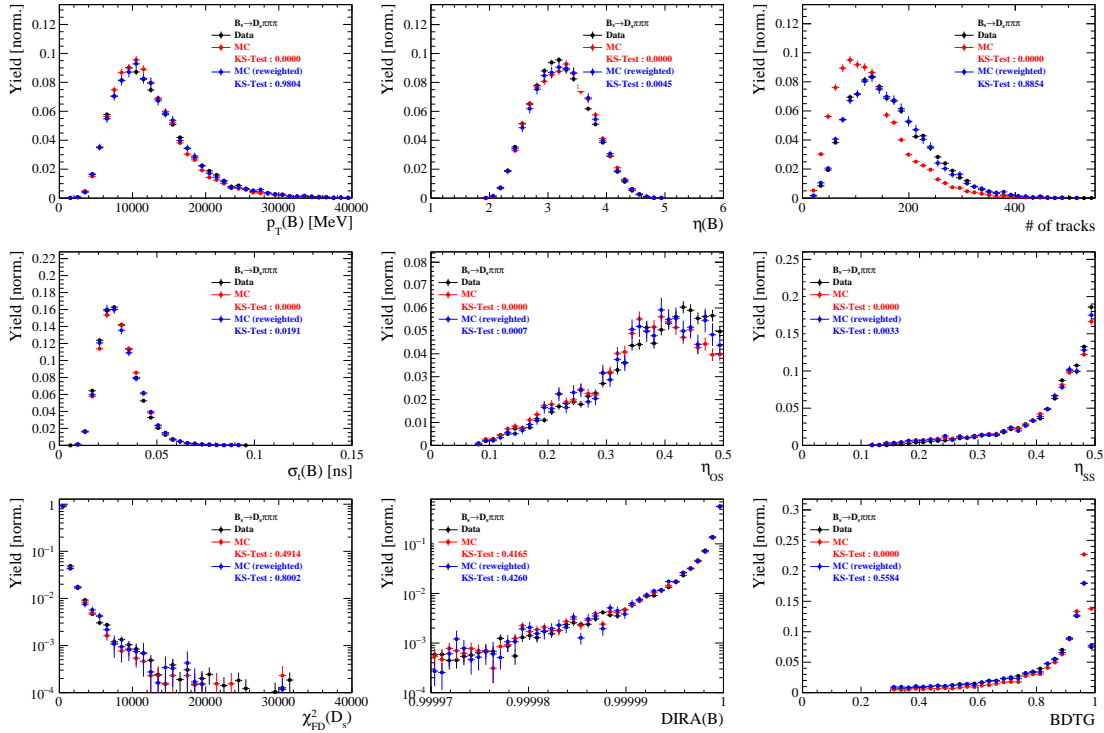


**Figure C.1:** Comparison between data and MC of selected variables for  $B_s \rightarrow D_s \pi\pi\pi$  decays.

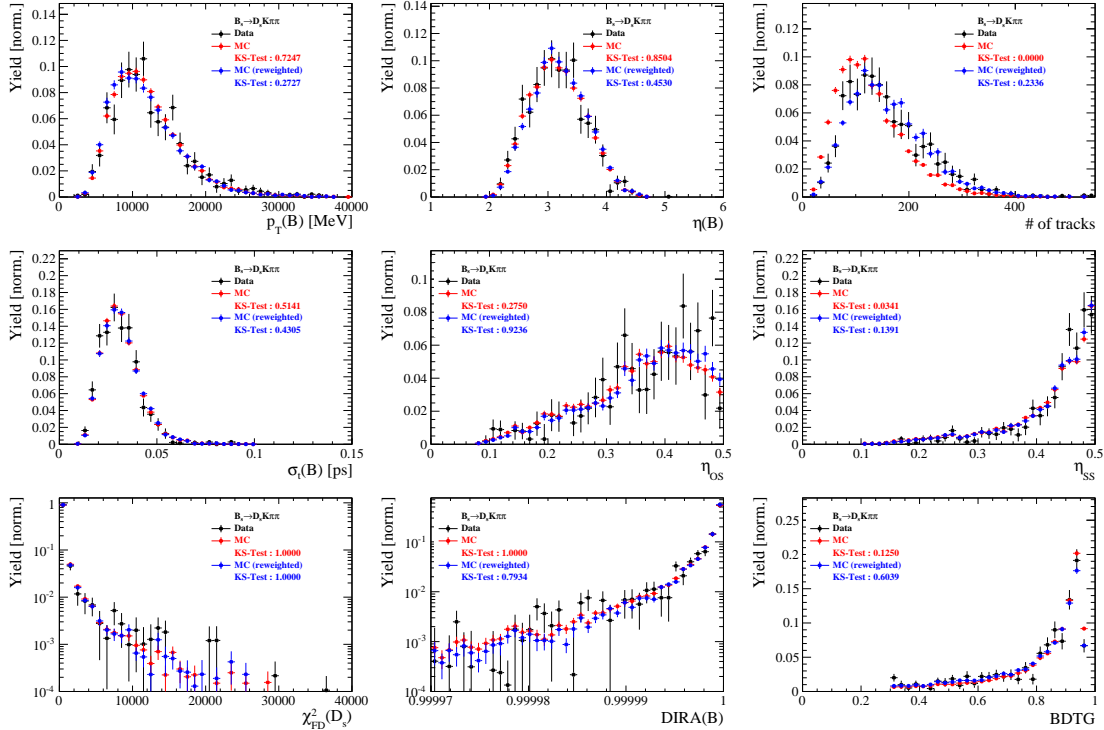


**Figure C.2:** Comparison between data and MC of selected variables for  $B_s \rightarrow D_s K\pi\pi$  decays.

1040 I Data distributions

1041 I.1 Comparison of signal and calibration channels

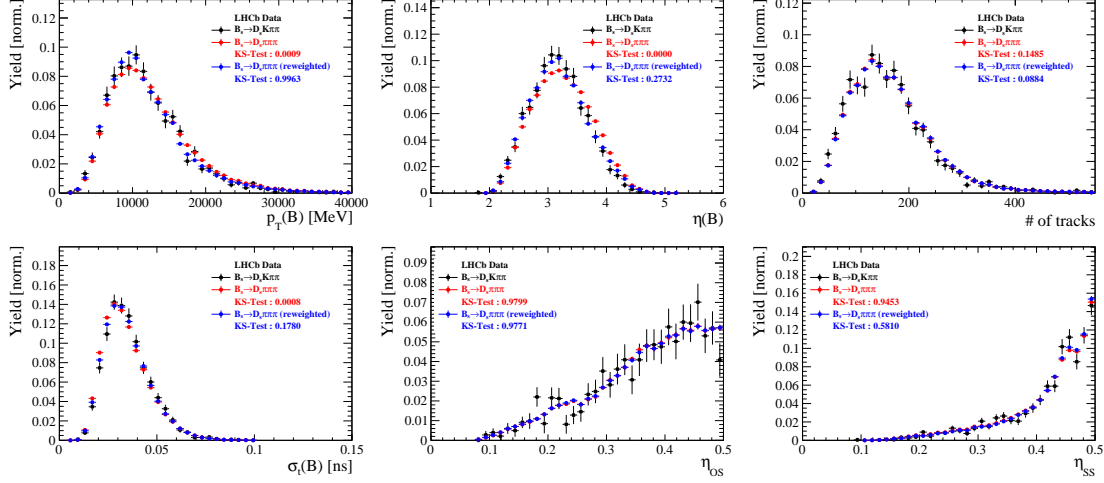


**Figure C.1:** Comparison between  $B_s \rightarrow D_s K\pi\pi$  and  $B_s \rightarrow D_s \pi\pi\pi$  decays for selected variables.

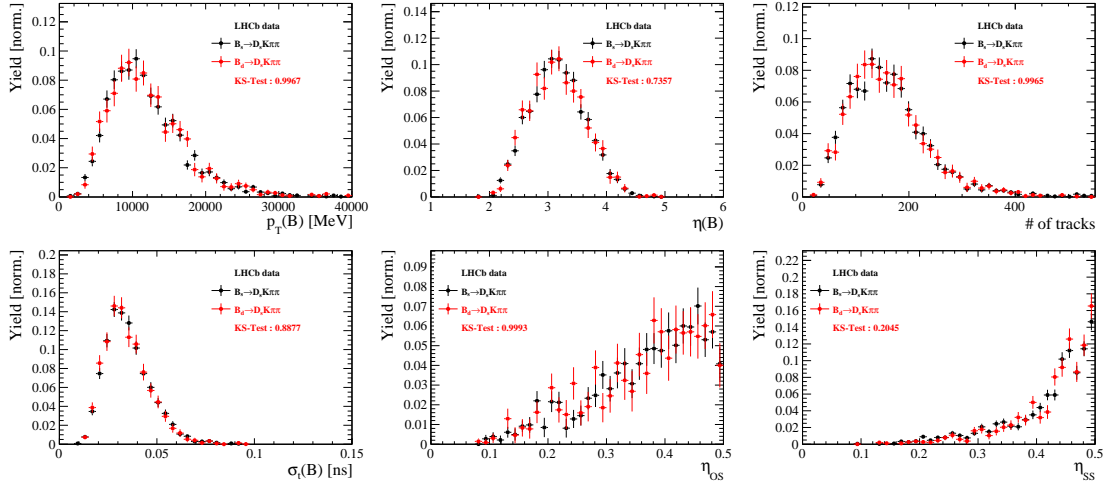


**Figure C.2:** Comparison between  $B_s \rightarrow D_s K\pi\pi$  and  $B_d \rightarrow D_s K\pi\pi$  decays for selected variables.

1042 I.2 Comparison of Run-I and Run-II data

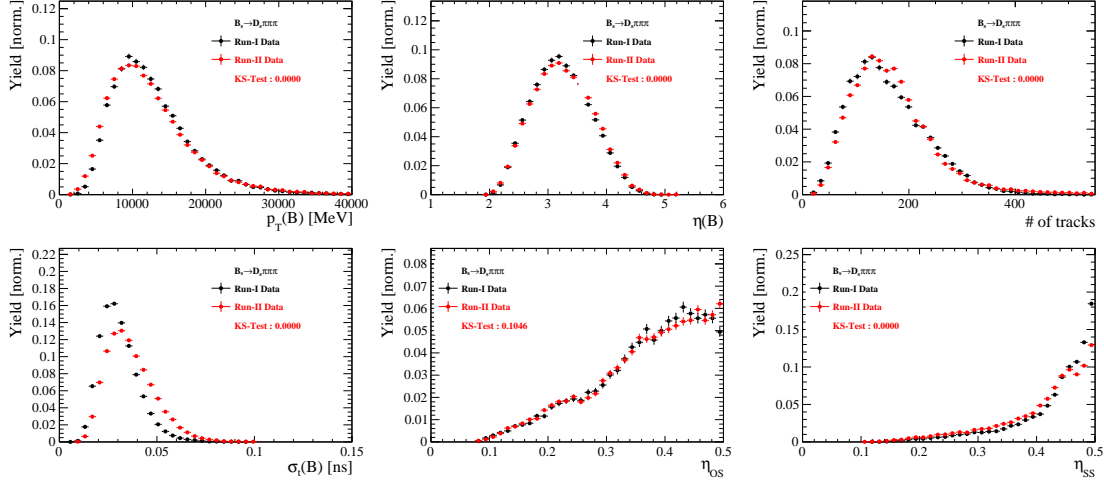


Figure C.3: Comparison of selected variables for Run-I and Run-II data.

1043 I.3 Comparison of  $D_s$  final states

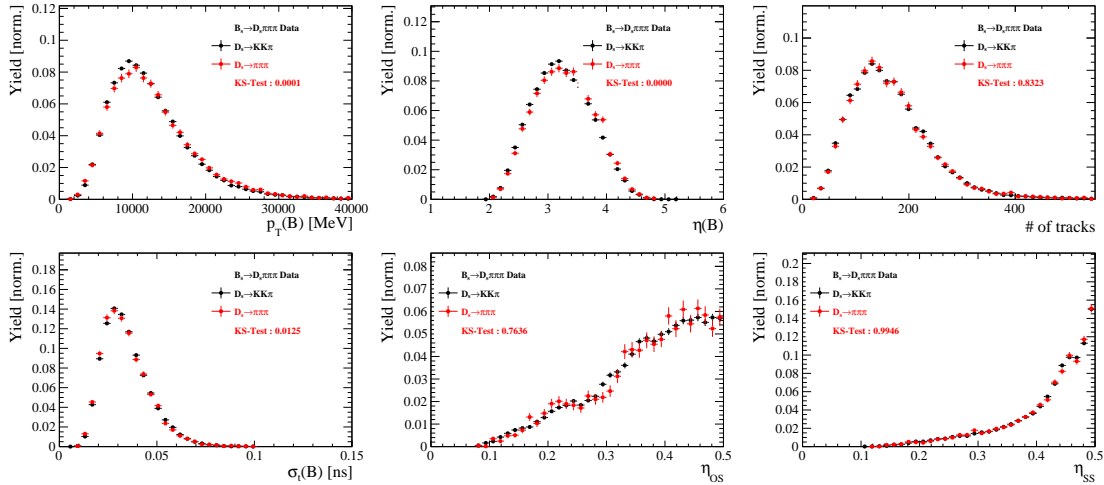
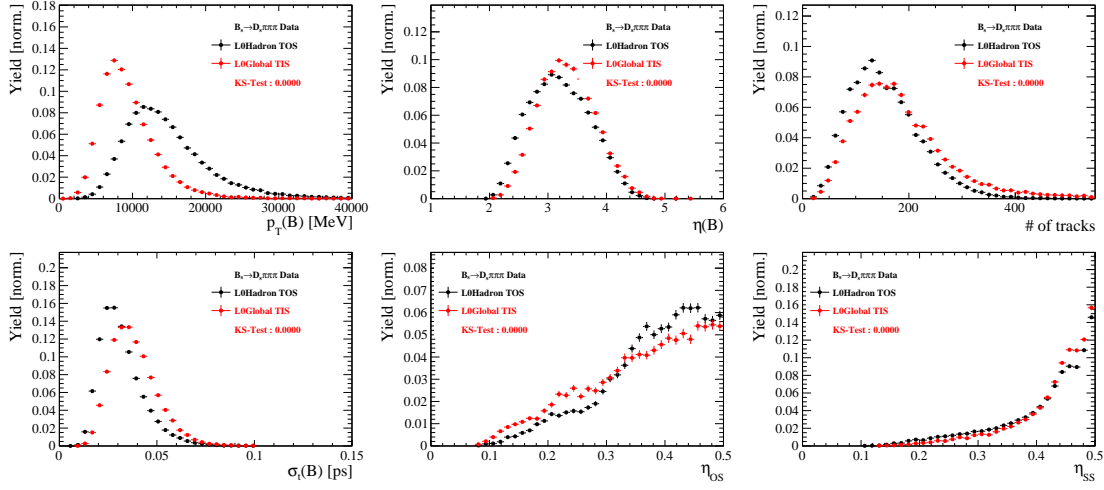


Figure C.4: Comparison of selected variables for different  $D_s$  final states.

1044 I.4 Comparison of trigger categories



**Figure C.5:** Comparison of selected variables for different trigger categories.

## 1045 References

- 1046 [1] R. Fleischer, *New strategies to obtain insights into CP violation through  $B(s) \rightarrow D(s) \rightarrow K \pi$ ,  $D(s)^* \rightarrow K \pi$ , ... and  $B(d) \rightarrow D \pi \pi$ ,  $D^* \pi \pi$ , ... decays*, Nucl.  
1047 Phys. **B671** (2003) 459, arXiv:hep-ph/0304027.
- 1048
- 1049 [2] K. De Bruyn *et al.*, *Exploring  $B_s \rightarrow D_s^{(*)\pm} K^\mp$  Decays in the Presence of a Sizable*  
1050 *Width Difference  $\Delta\Gamma_s$* , Nucl. Phys. **B868** (2013) 351, arXiv:1208.6463.
- 1051 [3] S. Blusk, *First observations and measurements of the branching fractions for the*  
1052 *decays  $\bar{B}_s^0 \rightarrow D_s^+ K^- \pi^+ \pi^-$  and  $\bar{B}^0 \rightarrow D_s^+ K^- \pi^+ \pi^-$* .
- 1053 [4] LHCb, S. Blusk, *Measurement of the CP observables in  $\bar{B}_s^0 \rightarrow D_s^+ K^-$  and first obser-*  
1054 *vation of  $\bar{B}_{(s)}^0 \rightarrow D_s^+ K^- \pi^+ \pi^-$  and  $\bar{B}_s^0 \rightarrow D_{s1}(2536)^+ \pi^-$* , 2012. arXiv:1212.4180.
- 1055 [5] E. Byckling and K. Kajantie, *Particle Kinematics*, John Wiley & Sons, 1973.
- 1056 [6] S. Mandelstam, J. E. Paton, R. F. Peierls, and A. Q. Sarker, *Isobar approximation*  
1057 *of production processes*, Annals of Physics **18** (1962), no. 2 198 .
- 1058 [7] D. J. Herndon, P. Söding, and R. J. Cashmore, *Generalized isobar model formalism*,  
1059 Phys. Rev. D **11** (1975) 3165.
- 1060 [8] J. J. Brehm, *Unitarity and the isobar model: Two-body discontinuities*, Annals of  
1061 Physics **108** (1977), no. 2 454 .
- 1062 [9] P. d'Argent *et al.*, *Amplitude Analyses of  $D^0 \rightarrow \pi^+ \pi^- \pi^+ \pi^-$  and  $D^0 \rightarrow K^+ K^- \pi^+ \pi^-$*   
1063 *Decays*, JHEP **05** (2017) 143, arXiv:1703.08505.
- 1064 [10] F. von Hippel and C. Quigg, *Centrifugal-barrier effects in resonance partial decay*  
1065 *widths, shapes, and production amplitudes*, Phys. Rev. D **5** (1972) 624.
- 1066 [11] J. D. Jackson, *Remarks on the phenomenological analysis of resonances*, Il Nuovo  
1067 Cimento Series 10 **34** (1964), no. 6 1644.
- 1068 [12] Particle Data Group, C. Patrignani *et al.*, *Review of Particle Physics*, Chin. Phys.  
1069 **C40** (2016), no. 10 100001.
- 1070 [13] D. V. Bugg, *The mass of the  $\sigma$  pole*, Journal of Physics G Nuclear Physics **34** (2007)  
1071 151, arXiv:hep-ph/0608081.
- 1072 [14] G. J. Gounaris and J. J. Sakurai, *Finite-width corrections to the vector-meson-*  
1073 *dominance prediction for  $\rho \rightarrow e^+ e^-$* , Phys. Rev. Lett. **21** (1968) 244.
- 1074 [15] M. S. et al. *Search for CP violation in the  $D^0 \rightarrow K K \pi \pi$  decay through a full*  
1075 *amplitude analysis*, LHCb-ANA-2017-064.
- 1076 [16] S. M. Flatté, *Coupled-channel analysis of the  $\pi \eta$  and  $K K$  systems near  $K K$  threshold*,  
1077 Physics Letters B **63** (1976), no. 2 224 .
- 1078 [17] BES Collaboration, M. Ablikim *et al.*, *Resonances in  $J/\psi \rightarrow \phi \pi^+ \pi^-$  and  $\phi K^+ K^-$* ,  
1079 Phys. Lett. **B607** (2005) 243, arXiv:hep-ex/0411001.

- [18] W. Dunwoodie, Fits to  $K\pi$   $I = \frac{1}{2}$   $S$ -wave amplitude and phase data.
- [19] D. Aston *et al.*, *A Study of  $K$ - $\pi$ + Scattering in the Reaction  $K$ -  $p \rightarrow K$ -  $\pi$ +  $n$  at 11- $GeV/c$* , Nucl. Phys. **B296** (1988) 493.
- [20] BaBar, B. Aubert *et al.*, *Dalitz-plot analysis of the decays  $B^\pm \rightarrow K^\pm \pi^\mp \pi^\pm$* , Phys. Rev. **D72** (2005) 072003, arXiv:hep-ex/0507004, [Erratum: Phys. Rev.D74,099903(2006)].
- [21] LHCb, R. Aaij *et al.*, *Studies of the resonance structure in  $D^0 \rightarrow K^\mp \pi^\pm \pi^\pm \pi^\mp$  decays*, Eur. Phys. J. **C78** (2018), no. 6 443, arXiv:1712.08609.
- [22] C. Zemach, *Use of angular momentum tensors*, Phys. Rev. **140** (1965) B97.
- [23] W. Rarita and J. Schwinger, *On a theory of particles with half integral spin*, Phys. Rev. **60** (1941) 61.
- [24] S. U. Chung, *General formulation of covariant helicity-coupling amplitudes*, Phys. Rev. D **57** (1998) 431.
- [25] B. S. Zou and D. V. Bugg, *Covariant tensor formalism for partial wave analyses of  $\psi$  decay to mesons*, Eur. Phys. J. **A16** (2003) 537, arXiv:hep-ph/0211457.
- [26] V. Filippini, A. Fontana, and A. Rotondi, *Covariant spin tensors in meson spectroscopy*, Phys. Rev. **D51** (1995) 2247.
- [27] J.-J. Zhu, *Explicit expressions of spin wave functions*, arXiv:hep-ph/9906250.
- [28] M. Williams, *Numerical Object Oriented Quantum Field Theory Calculations*, Comput. Phys. Commun. **180** (2009) 1847, arXiv:0805.2956.
- [29] D. J. Lange, *The EvtGen particle decay simulation package*, Nucl. Instrum. Meth. **A462** (2001) 152.
- [30] M. Karbach and M. Kenzie, *Gammacombo package*, <http://gammacombo.hepforge.org/web/HTML/index.html>, 2014.
- [31] A. Hoecker *et al.*, *TMVA: Toolkit for Multivariate Data Analysis*, PoS **ACAT** (2007) 040, arXiv:physics/0703039.
- [32] N. L. Johnson, *Systems of frequency curves generated by methods of translation*, Biometrika **36** (1949), no. 1/2 149.
- [33] Particle Data Group, K. A. Olive *et al.*, *Review of Particle Physics*, Chin. Phys. **C38** (2014) 090001.
- [34] LHCb collaboration, R. Aaij *et al.*, *LHCb detector performance*, Int. J. Mod. Phys. **A30** (2015) 1530022, arXiv:1412.6352.
- [35] LHCb, R. Aaij *et al.*, *Measurement of CP asymmetry in  $B_s^0 \rightarrow D_s^\mp K^\pm$  decays*, Submitted to: JHEP (2017) arXiv:1712.07428.

- 1114 [36] LHCb collaboration, L. Zhang, *Measurements of CP violation in  $B_s^0 \rightarrow J/\psi K^+ K^-$*   
 1115 *decays in the low  $K^+ K^-$  mass range with 13 TeV data*, LHCb-ANA-2017-028.
- 1116 [37] A. Poluektov, *Correction of simulated particle identification response in LHCb using*  
 1117 *kernel density estimation*, LHCb-INT-2017-007.
- 1118 [38] Heavy Flavor Averaging Group, Y. Amhis *et al.*, *Averages of b-hadron, c-hadron, and*  
 1119  *$\tau$ -lepton properties as of summer 2014*, arXiv:1412.7515, updated results and plots  
 1120 available at <http://www.slac.stanford.edu/xorg/hfag/>.
- 1121 [39] T. M. Karbach, G. Raven, and M. Schiller, *Decay time integrals in neutral meson*  
 1122 *mixing and their efficient evaluation*, arXiv:1407.0748.
- 1123 [40] LHCb Collaboration, R. Aaij *et al.*, *Measurement of angular and cp asymmetries*  
 1124 *in  $D^0 \rightarrow \pi^+ \pi^- \mu^+ \mu^-$  and  $D^0 \rightarrow K^+ K^- \mu^+ \mu^-$  decays*, Phys. Rev. Lett. **121** (2018)  
 1125 091801.
- 1126 [41] LHCb collaboration, R. Aaij *et al.*, *Opposite-side flavour tagging of B mesons at the*  
 1127 *LHCb experiment*, Eur. Phys. J. **C72** (2012) 2022, arXiv:1202.4979.
- 1128 [42] LHCb, R. Aaij *et al.*, *A new algorithm for identifying the flavour of  $B_s^0$  mesons at*  
 1129 *LHCb*, JINST **11** (2016), no. 05 P05010, arXiv:1602.07252.
- 1130 [43] LHCb, R. Aaij *et al.*, *Measurement of  $B^0$ ,  $B_s^0$ ,  $B^+$  and  $\Lambda_b^0$  production asymmetries in 7*  
 1131 *and 8 TeV proton-proton collisions*, Phys. Lett. **B774** (2017) 139, arXiv:1703.08464.
- 1132 [44] H. Gordon, R. W. Lambert, J. van Tilburg, and M. Vesterinen, *A Measurement of*  
 1133 *the  $K\pi$  Detection Asymmetry*, Tech. Rep. LHCb-INT-2012-027. CERN-LHCb-INT-  
 1134 2012-027, CERN, Geneva, Feb, 2013.
- 1135 [45] A. Davis *et al.*, *Measurement of the instrumental asymmetry for  $K^- \pi^+$ -pairs at LHCb*  
 1136 *in Run 2*, Tech. Rep. LHCb-PUB-2018-004. CERN-LHCb-PUB-2018-004, CERN,  
 1137 Geneva, Mar, 2018.
- 1138 [46] I. I. Y. Bigi and H. Yamamoto, *Interference between Cabibbo allowed and doubly*  
 1139 *forbidden transitions in  $D \rightarrow K(S)$ ,  $K(L) + \pi$ 's decays*, Phys. Lett. **B349** (1995)  
 1140 363, arXiv:hep-ph/9502238.
- 1141 [47] M. Pivk and F. R. Le Diberder, *sPlot: A statistical tool to unfold data distributions*,  
 1142 Nucl. Instrum. Meth. **A555** (2005) 356, arXiv:physics/0402083.
- 1143 [48] R. Tibshirani, *Regression shrinkage and selection via the Lasso*, Journal of the Royal  
 1144 Statistical Society, Series B **58** (1994) 267.
- 1145 [49] B. Guegan, J. Hardin, J. Stevens, and M. Williams, *Model selection for amplitude*  
 1146 *analysis*, JINST **10** (2015), no. 09 P09002, arXiv:1505.05133.
- 1147 [50] G. Schwarz, *Estimating the dimension of a model*, Ann. Statist. **6** (1978) 461.
- 1148 [51] CLEO Collaboration, M. Artuso *et al.*, *Amplitude analysis of  $D^0 \rightarrow K^+ K^- \pi^+ \pi^-$* ,  
 1149 Phys. Rev. **D85** (2012) 122002, arXiv:1201.5716.

- 1150 [52] T. Skwarnicki, *A study of the radiative cascade transitions between the Upsilon-prime*  
1151 *and Upsilon resonances*, PhD thesis, Institute of Nuclear Physics, Krakow, 1986,  
1152 DESY-F31-86-02.
- 1153 [53] D. Hill, M. John, and P. Gandini, *A study of partially reconstructed  $B^\pm \rightarrow D^{*0} h^\pm$*   
1154 *decays using the  $D^0 \rightarrow K\pi, KK, \pi\pi$  final states*, .
- 1155 [54] G. H. Golub and C. F. Van Loan, *Matrix Computations (3rd Ed.)*, Johns Hopkins  
1156 University Press, Baltimore, MD, USA, 1996.
- 1157 [55] L. collaboration, *Precision measurement of the  $B_s$  oscillation frequency with the decay*  
1158  $B_s \rightarrow D_s\pi$ , LHCb-ANA-2012-053.